Shape Descriptors

Department of Computer Science

University of Exeter

Submitted by Mehmet Ali Aktas, to the University of Exeter as a thesis for the degree of Doctor of Philosophy in Computer Science, October 2012.

I certify that all material in this thesis which is not my own work has been identiffied and that no material has previously been submitted and approved for the award of a degree by this or any other University.

Mehmet Ali Aktaş

Abstract

Every day we recognize a numerous objects and human brain can recognize objects under many conditions. The way in which humans are able to identify an object is remarkably fast even in different size, colours or other factors. Computers or robots need computational tools to identify objects. Shape descriptors are one of the tools commonly used in image processing applications. Shape descriptors are regarded as mathematical functions employed for investigating image shape information. Various shape descriptors have been studied in the literature. The aim of this thesis is to develop new shape descriptors which provides a reasonable alternative to the existing methods or modified to improve them.

Generally speaking shape descriptors can be categorized into various taxonomies based on the information they use to compute their measures. However, some descriptors may use a combination of boundary and interior points to compute their measures. A new shape descriptor, which uses both region and contour information, called centeredness measure has been defined. A new alternative ellipticity measure and sensitive family ellipticity measures are introduced. Lastly familiy of ellipticity measures, which can distinguish between ellipses whose ratio between the length of the major and minor axis differs, have been presented. These measures can be combined and applied in different image processing applications such as image retrieval and classification. This simple basis is demonstrated through several examples.

Contents

List of Figures

List of Tables

Acknowledgements

I want to thank to all the people who have supported me in so many ways to complete this work: to my supervisor Dr. Joviša Žunić for his extreme patience throughout my PhD; to all my friends and colleagues for their academic support; to my family and friends in the UK, in Turkey and to those scattered around the globe for their love and constant support. And above all, thanks to my parents for their guidance, support and unconditional love through all these years

Chapter 1

Introduction

It is a common saying that "a picture is worth a thousand words". It is true that visual information is very useful in communicating ideas and certainly humans rely heavily on sight to perceive information regarding the physical world surrounding us. The way in which the human brain processes visual information has been a topic of study for many years.

Every day we recognize numerous objects and object recognition is one of the most fascinating abilities that human brain easily possess, despite the fact that these objects may vary in size, color, orientation, lighting conditions and other factors. The way in which humans are able to process complex visual information and identify an object is remarkably fast. It would be good for robotic applications or cameras to be able to imitate these capabilities.

While it may be obvious that people are capable of recognizing objects with little effort under many variations in conditions, it is one of the hardest challenges for computer vision systems today. Imitating human vision into machine ability has been studied and worked on for more than four decades Jain et al. (1995). There have been significant efforts made to develop representation schemes and algorithms aimed at collecting information and learning about the world around them. In this way computers can eventually understand their surroundings in a very similar way as humans do. The fields of application for computer vision are diverse: any human activity could potentially benefit from it.

1.1 Background

For a digital computer to be able to process an image, it is first necessary to reduce the image to a series of discrete values that can be manipulated by the computer. The image is then a discrete grid of picture elements (pixels) which also have discrete values. This is known as a digital image. The digital images which are captured from digital camera, scanner, etc. must be quantized for digital processing. The necessary quantization step inescapably causes a loss of information. A typical digitized image may have 512×512 or roughly 250,000 pixels and high resolution images are becoming common which is acquired by high quality instruments (e.g. High resolution cameras). This high quality instruments may help avoid the error produced by the quantisation process. A wide research in the literature has been done to reduce the loss of information. There are other alternatives to pixel based representation, like region-based representations, which created by merging similar pixels, and vector graphics which use geometrical primitives. (e.g. curves, lines, points). Several image representation techniques are available in the literature to represent visual data. The represented data should be processed to use for specific tasks. This is what we call image processing application. Generally speaking most image processing applications consist of most of the following components:

- Acquisition - The first process is to capture an image. This can be done by equipments which have the ability to digitize the signal produced by the sensor. The sensor can be digital cameras, scanners or other types of sensors. Moreover, the digital image can be constructed by using photo editing programs.

- Pre-processing - The digital image must be prepared before a computer vision method can be applied. The ultimate goal of this step is to modify the image in order to discard unimportant information and extract some specific piece of information which can be useful for further tasks. The steps of the pre-processing includes: Normalisation, smoothing, Noise reduction, boundary extraction, colour format conversions, binarization, object segmentation, etc.
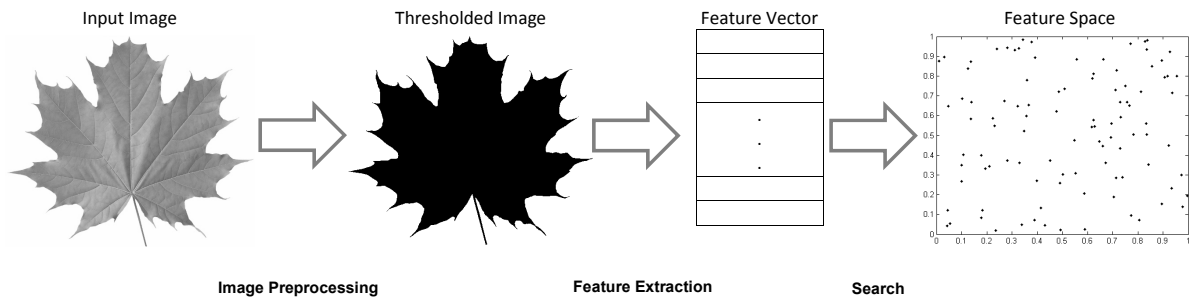
Figure 1.2.1: Structure of a typical image matching system.

- Feature extraction - This is the process of obtaining information from the object in question, highlighting its features of interest. These features or descriptors may be obtained from the objects boundary, surface, texture, or any other characteristic. The features of an object are typically represented in a quantitative form which allows for comparison between objects. Such features can also be extracted by using computational methods called shape descriptors.

- Further processing - Once the relevant information has been extracted the derived information may be used to perform further tasks which depend on the aim of application, for example, recognition, classification, similarity search, etc.

1.2   Shape descriptors

Shape descriptors are considered as mathematical functions employed for investigating image shape information. When applied this function to an image, it is creating numerical values. In general, descriptors are some sets of numerical values that are produced to describe a given shape. Usually, the descriptors are in the form of a vector. After shape features have been extracted, they can be used for further tasks. For example, for a shape matching task, the distance between the vectors of shape descriptors can be measured, or for classification task, a vector of shape descriptor can be entered to a classifier to determine the class of the given shape. A model related to the matching process has been given in Fig.1.2.1 and a detailed information about shape descriptor applications is given later in this section (see page 31).

Generally speaking shape descriptors can be categorized into various taxonomies based on the information they use to compute their measures. Descriptors that use the points on the boundary of the shape, ignoring the shape interior content are called contour based descriptors. On the other hand, descriptors that exploit the interior of the object are called region based descriptors. However it is important to point out that some descriptors may use a combination of boundary and interior points to compute their measures.

Depending on the type of the application, contour based descriptors can be considered advantageous over region based descriptors or vice versa.

Contour based methods are generally sensitive to noise and variations as they only use boundary of the shape; this usually causes these methods to be sensitive to small differences and produce different results when the shape boundary changes slightly. Besides, in many cases, the shape boundary is not available. Moreover, they are not suitable for disjoint shapes or shapes with holes inside. Lastly, in some applications, shape content is more important than the contour features.

On the contrary, region based shape descriptors are not sensitive to small changes on the shape for example big changes on the boundary does not affect the area of the shape thus they do not produce different results which make them robust with respect to noise. Moreover, they are applicable to generic shapes and are more robust to noise and shape distortions.

The descriptors should have certain desirable properties. Below is a short list of these desirable properties:

- Rotation invariance - Rotating an object does not affect its shape but it can cause the change of the pixel positions. However, it is expected that, for a shape S and for the same shape rotated by θ degrees, $R(S, \theta)$, a shape descriptor should produce the same measure

- Translation invariance - Translating an object is going to cause changes on the coordinate of the object pixels. But, it would be expected that the produced measure for the shape S should remain unchanged when transformations are applied to the shape S.

- Scale invariance - When the size of shapes are increased or decreased, the pixels of images will be changed as well. In this case, changing the size of the object should not affect the measure produced by a shape descriptor.

- Affine invariance - Affine invariance is an important property of shape descriptors. Applying an affine transformation (e.g., shearing) to an image is going to cause the pixels to be transformed from one coordinates to another. In this case, applying an affine transformation to the shape S should not affect the measure.

1.3 Existing shape descriptors

Over the years there has been a continuous interest in shape descriptors. Many different approaches have been taken and there is a large existing body of available literature.

As mentioned previously, shape descriptors can be broadly categorized as region-based and contour-based descriptors. This section provides the reader with a brief survey of some of the methods considered most relevant to this thesis. Section 1.3.1 presents a brief overview of the area based shape descriptors and section 1.3.2 presents a brief overview of the boundary based shape descriptors.

1.3.1 Area Based Shape Descriptors

1.3.1.1 Region Based Moments

One of the most well-known shape descriptors are moment invariants introduced by Hu (1962) which have been used extensively in the literature on their own and as basis to construct other shape descriptors. The basic definition of geometric moments of $(p + q)$-th order is as follows:

$$M_{pq} = \int_{-\infty}^{\infty} \int_{-\infty}^{\infty} x^p \, y^q \, f(x, y) \, \mathrm{d}x \, \mathrm{d}y \qquad (1.3.1)$$

19

where $p, q = 0, 1, 2, 3, ..., \infty$ and $f(x, y)$ is the intensity function of the image. If the given image is a binary image representing a shape S, we can simplify the definition of moments to the following expression:

$$M_{pq}(S) = \int_{-\infty}^{\infty} \int_{-\infty}^{\infty} x^p \, y^q \, \mathrm{d}x \, \mathrm{d}y \tag{1.3.2}$$

Properties of Geometric Moments

The lower order moments represent some well known fundamental geometric properties of the underlying image functions.

Central Moments

In order to attain translation invariance, moments are translated to the centroid of the shape. These are called central moments $\mu_{p,q}$ and are defined as:

$$\mu_{pq} = \int_{-\infty}^{\infty} \int_{-\infty}^{\infty} (x - \overline{x})^p \, (y - \overline{y})^q \, f(x, y) \, \mathrm{d}x \, \mathrm{d}y \tag{1.3.3}$$

where $\overline{x}$ and $\overline{y}$ are the centroid of the shape defined as in (1.3.7).

Mass and Area

The zeroth order of the geometric moments, M_{00},

$$M_{00} = \int_{-\infty}^{\infty} \int_{-\infty}^{\infty} f(x, y) \, \mathrm{d}x \, \mathrm{d}y \tag{1.3.4}$$

represents the total mass of the given function or image $f(x, y)$. When we work on a binary image, the zeroth moment (1.3.4) represent the total area of the image.

Centre of Mass

The two first order moments can be used

$$M_{10} = \int_{-\infty}^{\infty} \int_{-\infty}^{\infty} x \, f(x, y) \, \mathrm{d}x \, \mathrm{d}y \tag{1.3.5}$$

and

$$M_{01} = \int_{-\infty}^{\infty} \int_{-\infty}^{\infty} y \, f(x, y) \, \mathrm{d}x \, \mathrm{d}y \tag{1.3.6}$$

to represent the centre of mass of the image $f(x, y)$. In terms of moment values, the coordinates of the centre of mass are

$$\overline{x} = \frac{M_{10}}{M_{00}}, \qquad \overline{y} = \frac{M_{01}}{M_{00}}. \tag{1.3.7}$$

Scale invariant moments

It is possible to constract moments η_{ij} where $i + j \leq 2$ to be invariant to both translation and changes in scale. To do that, the corresponding central moment should be divided by the properly scaled (00)-th moment.

$$\eta_{ij} = \frac{\mu_{ij}}{\mu_{00}^{(1 + \frac{i+j}{2})}} \tag{1.3.8}$$

Rotation invariant moments

The centralised moments are invariant with respect to translation and can be normalised to be invariant with respect to changes in scale. However, to enable invariance to rotation they require reformulation. Hu derived a set of invariants from algebraic invariants applied to the moment generating function under a rotation transformation. They are computed from normalised centralised moments. The first 7 I_n n-th Hu invariant moment which have been widely used in the literature are defined as:

$$I_1 = \eta_{20} + \eta_{02} \tag{1.3.9}$$

$$I_2 = (\eta_{20} - \eta_{02})^2 + (2\eta_{11})^2 \tag{1.3.10}$$

$$I_3 = (\eta_{30} - 3\eta_{12})^2 + (3\eta_{21} - \eta_{30})^2 \tag{1.3.11}$$

$$I_4 = (\eta_{30} + \eta_{12})^2 + (\eta_{21} + \eta_{30})^2 \tag{1.3.12}$$

$$I_5 = (\eta_{30} - 3\eta_{12})(\eta_{30} + \eta_{12})[(\eta_{30} + \eta_{12})^2 - 3(\eta_{21} + \eta_{30})^2] +$$
$$(3\eta_{21} - \eta_{30})(\eta_{21} + \eta_{30})[3(\eta_{30} + \eta_{12})^2 - (\eta_{21} + \eta_{30})] \tag{1.3.13}$$

$$I_6 = (\eta_{20} - \eta_{02})[(\eta_{30} + \eta_{12})^2 - (\eta_{21} + \eta_{30})^2] + 4\eta_{11}(\eta_{30} + \eta_{12})(\eta_{12} + \eta_{30}) \tag{1.3.14}$$

$$I_7 = (3\eta_{21} - \eta_{03})(\eta_{30} + \eta_{12})[(\eta_{30} + \eta_{12})^2 - 3(\eta_{21} + \eta_{03})^2] -$$
$$(\eta_{30} - \eta_{12})(\eta_{21} + \eta_{03})[3(\eta_{30} + \eta_{12})^2 - (\eta_{21} + \eta_{03})] \tag{1.3.15}$$

1.3.1.2 Shape Orientation.

The second order moments, $\{M_{11}, M_{02}, M_{20}\}$, known as the moments of intertia, are also used to determine the shape orientation which is a necessary part of an image normalisation procedure. The most standard method for the computation of the shape orientation is defined as an angle between x axis and principal axis. This method of orientation says that the orientation of an object is given by the line which minimises the sum of squared distance of points belonging to the shape to the line.

In terms of moments, the orientations of the principal axes, θ, are given by Jain et al. (1995).

$$\theta = \frac{1}{2} tan^{-1} (\frac{2\mu_{11}}{\mu_{20} - \mu_{02}})$$ (1.3.16)

1.3.1.3 Shape Elongation.

Elongation is a very common shape descriptor. Because of its clear meaning and applicability, it is used in many shape classification tasks. The standard elongation is consider the ratio of the height and width of a rotated minimum area bounding rectangle for the measured shape (Jenkin and Harris, 1997). In other words, rotate a rectangle so that it is the smallest rectangle in which the shape fits then compare its height to its width (see Fig.1.3.1).

$$Elongation = \frac{Width_{bounding-box}}{Length_{bounding-box}}$$ (1.3.17)
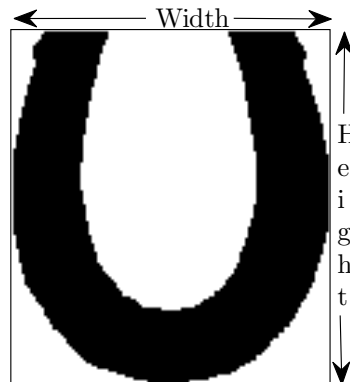
Figure 1.3.1: Illustration of the elongation measure.

It is also possible to compute the ellongation by using central moments as defined in Sonka et al. (2007).

$$\mathbf{El}(S) = \frac{\mu_{2,0}(S) + \mu_{0,2}(S) - \sqrt{4\mu_{1,1}(S)^2 + (\mu_{2,0}(S) - \mu_{0,2}(S))^2}}{\mu_{2,0}(S) + \mu_{0,2}(S) + \sqrt{4\mu_{1,1}(S)^2 + (\mu_{2,0}(S) - \mu_{0,2}(S))^2}}. \tag{1.3.18}$$

where $\mu_{p,q}$ are centralised moments of the shape S defined as in Eq.1.3.3

1.3.1.4 Shape Circularity.

Moments are widely used in literature, for different applications and for the creation of shape descriptors. An example of shape descriptors derived from moment invariants is the circularity descriptor developed by Žunić et al. (2010). They use second order centralised moments to derive their measure, by showing that the quantity

$$\frac{\mu_{2,0}(S) + \mu_{0,2}(S)}{\mu_{0,0}(S)^2} \tag{1.3.19}$$

reaches its minimum if and only if the given shape S is a circle. This shape descriptor gives a measure of similarity between a given shape and a perfect circle and it ranges over $(0, 1]$. This is also referred to as compactness.

The circularity measure introduced by Žunić et al. (2010) is defined as follows:

$$K_{std}(S) = \frac{1}{2\pi} \cdot \frac{\mu_{0,0}(S)^2}{\mu_{2,0}(S) + \mu_{0,2}(S)} \tag{1.3.20}$$

The descriptor is modified by an additional tuning parameter β which modifies the behaviour of the descriptor. The modified circularity measure is defined as follows:

$$K_\beta(S) = \begin{cases} \dfrac{1}{\beta + 1\pi^\beta} \cdot \dfrac{\mu_{00}(S)^{\beta+1}}{\iint\limits_S (x^2 + y^2)^\beta dx dy} & \beta > 0, \\[20pt] \dfrac{\beta + 1\pi^\beta}{1} \cdot \dfrac{\iint\limits_S (x^2 + y^2)^\beta dx dy}{\mu_{00}(S)^{\beta+1}} & \beta \in (-1, 0). \end{cases} \tag{1.3.21}$$

The other approache to the same problem is calculating the intersection and union of the shape area S with the area of the circle K that best fits to the shape. Then the final circularity measure is the ratio of the areas of the intersection and union of S and K.

$$K_{fit}(S) = \frac{S \cap K}{S \cup K} \qquad (1.3.22)$$

This approach is used in the literature to define other shape descriptors such as: ellipticity, rectangularity, triangularity, etc. (Lee and Sallee, 1970).

1.3.1.5 Shape Rectangularity.

The rectangularity measure defined in Rosin (1999) considers fitting a rectangle $R(S)$ to the shape S based on moments. Then the rectangularity is defined as the normalised discrepancies between the areas of the $R(S)$ and S. More precisely, given the following quantities: R – the area of difference between the fitting rectangle $R(S)$ and the shape S; D – the area of difference between the shape S and the fitting rectangle $R(S)$; and B – the area of the fitting rectangle $R(S)$, then the rectangularity measure is:

$$R'_D(S) = 1 - \frac{R + D}{B} \qquad (1.3.23)$$

The illustration of the $R'_D(S)$ rectangularity measure is in Fig.1.3.2. Fig.1.3.2(a) is the shape S, Fig.1.3.2(b) shows the constructed fitting rectangle ($R(S)$), and Fig.1.3.2(c) shows the $R + D$.

(a)   (b)   (c)
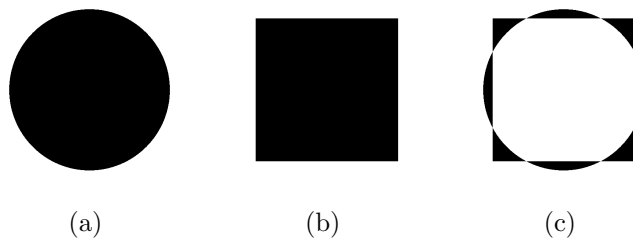
Figure 1.3.2: Illustration of the $R'D$ measure.

The other rectangularity measure defined in the same paper is similar to the previous measure. It introduces I – the area of intersection of the shape S and the fitting rectangle $R(S)$ rather than the area of the fitting rectangle (denoted above by B).

$$R_R(S) = 1 - \frac{R + D}{I} \qquad (1.3.24)$$

The illustration of the R_R rectangularity measure is in Fig.1.3.3. Fig.1.3.3(a) is the shape S, Fig.1.3.2(b) shows the constructed fitting rectangle $(R(S))$, Fig.1.3.3(c) shows the $R + D$, and Fig.1.3.3(d) shows the I.

(a)   (b)   (c)   (d)
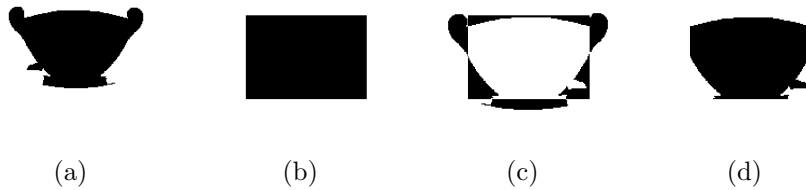
Figure 1.3.3: Illustration of the R_R measure.

1.3.2 Boundary Based Shape Descriptors

1.3.2.1 Contour Based Moments

Moments as defined in Eq.(1.3.2) are computed from shape area information. However moments can also be computed from shape boundary information (Lambert and Gao, 1995). These are referred to as line moments. In order to compute line moments, the boundary of any given shape S has to be expressed in parametric form.

First let us introduce the parametric representation of a given shapes contour. Let B be the boundary of a given shape S and let us start by assuming that B is an open curve. Also let P be the length of B. We then can refer to the coordinates of any point of $B(s) = (x(s), y(s))$ for $0 \leq s \leq P$. Of course if B is a closed curve it only means that $B(0) = B(P)$.

Line moments can be calculated for open curve segments and partially extracted boundaries. Line moments are defined as follows:

$$m_{pq}^{(l)}(B) = \int_B x(s)^p \, y(s)^q \mathrm{d}s \qquad (1.3.25)$$

where the shape boundary B is given in parametric form and $s \in [0, length(B)]$.

It is possible to derive central moments using the boundary information:

$$m_{pq}^{(l)}(B) = \int_B \left(x(s) - \overline{x}^{(l)}\right)^p \left(y(s) - \overline{y}^{(l)}\right)^q \mathrm{d}s \qquad (1.3.26)$$

In this case in terms of boundary moments, the coordinates of the centroid are:

$$\overline{x}^{(l)} = \frac{m_{10}^{(l)}(B)}{m_{00}^{(l)}(B)}, \qquad \overline{y}^{(l)} = \frac{m_{01}^{(l)}(B)}{m_{00}^{(l)}(B)}. \qquad (1.3.27)$$

1.3.2.2 Convexity Measure.

One of the mostly used shape descriptors is the shape convexity. Convexity is an important shape descriptor and several convexity measures have been developed (Rahtu et al., 2006; Padraig Corcoran and Winstanley, 2011) and used for many image processing tasks such as: image segmentation (Pao et al., 1999), shape decomposition (Latecki and Lakmper, 1999; Rosin, 2000) etc. The most standard convexity is defined as the ratio between the convex hull perimeter of an object and its perimeter (Sonka et al., 2007). For a given shape S, its convexity measure $Convexity(S)$ is defined as:

$$Convexity(S) = \frac{Perimeter\_of\_ConvexHull(S)}{Perimeter(S)} \qquad (1.3.28)$$

1.3.2.3 Fourier Descriptors

As stated previously, shape descriptors are classified mainly into two classes. Area based and contour based. In some applications contour content can be more important than the internal content (chromosome classification, identification of aircraft and identification of particles). Contour based techniques can be more efficient for the shapes which are describable by their object boundary (Mokhtarian and Bober, 2003). Several contour-based shape descriptors have been studied in the literature, including Fourier descriptors [13].

The idea is to represent the contour as a function, transform the function in its Fourier series, and use the coefficients of the series as Fourier descriptors (FDs).

In other words, to derive the Fourier descriptors of an image, the considered shape should be converted to 1-D signature.

Let $x[n]$ and $y[n]$ be the coordinates of the n-th pixel on the boundary of a given shape and let $z[n]$ be a shape signature which is generated by using the boundary points $(x[n] \ \ y[n])$, then a complex number can be formed as $z[n] = x[n] + jy[n]$ and the Fourier Descriptor (FD) of this shape is defined as:

$$a_m = FDT(z[n]) = \frac{1}{N} \sum_{n=0}^{N-1} z[n] exp(-j2\pi mn/N) \quad (m = 0, 1, 2, 3, ..., N-1) \quad (1.3.29)$$

where N is the total number of pixels in the boundary.

Many signatures have been proposed in the literature such as: Radial distance, triangular centroid area, polar coordinates, farthest point distance signature etc. (Zhang and Lu, 2002, 2005; El-ghazal et al., 2009). A short overview related to the existing shape signitures has been given below.

– Centroid Distance

The centroid distance considers the distance between the boundary points $(x(n) \ \ y(n))$ and the centoid $((x(c) \ \ y(c)))$ of the shape and defined as in Zhang and Lu (2002, 2005):

$$cd(n) = \sqrt{(x(n) - x(c))^2 + (y(n) - y(c))^2}$$

The centoids $((x(c) \ \ y(c)))$ can be computed as in Eq.1.3.7. They used the centoids to make the measure to be invariant with respect to translation.
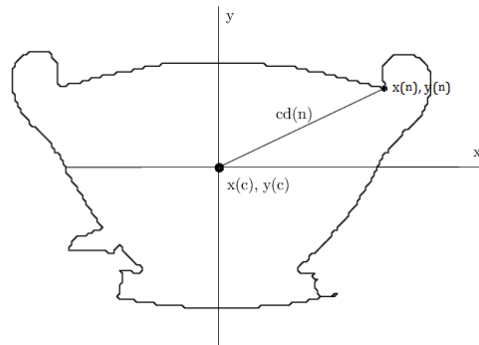
Figure 1.3.4: Illustration of the $cd(n)$ signature.

– Triangular centroid area

Triangular centroid area considers the area of the triangle between the two boundary points $(x(n),\ y(n)), (x(n{+}1),\ y(n{+}1))$ and the centroid $((x(c)\ y(c)))$ of the shape (see Fig.1.3.5). This area is used as a shape signature and can be calculated with the following equation:

$$TCA(n) = \tfrac{1}{2}\,|\,x(n)\ y(n{+}1) - x(n{+}1)\ y(n)\,|$$
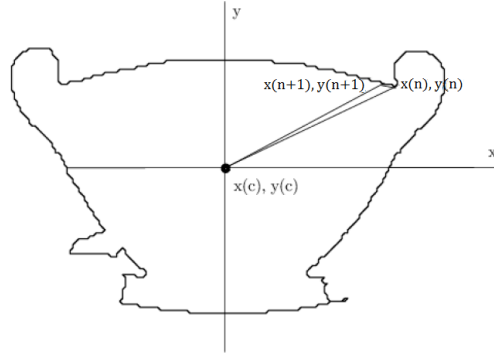
Figure 1.3.5: Illustration of the $TCA(n)$ signature.

– Farthest point distance

In El-ghazal et al. (2009) they defined this signature as the sum of the Euclidean distance between the boundary point $(x(n), y(n))$ to the centroid $(x(c), y(c))$ and the Euclidean distance between the centroid $(x(c), y(c))$ to the farthest point $(x(f), y(f))$ (see Fig.1.3.6 for illustration). It is possible to compute this signature as:

$$FPD(n) = \sqrt{([x(n) - x(c)]^2 + [y(n) - y(c)]^2)} + \sqrt{([x(f) - x(c)]^2 + [y(f) - y(c)]^2)}$$
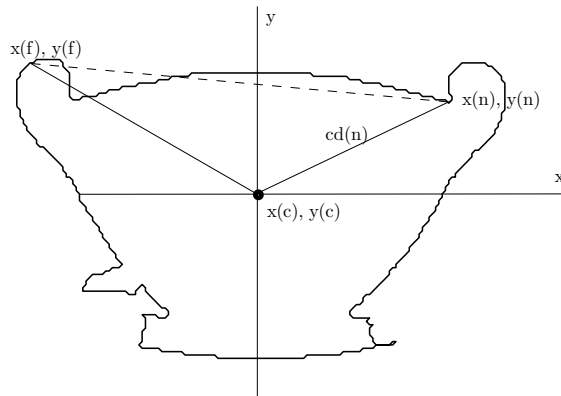
Figure 1.3.6: Illustration of the $FPD(n)$ signature.

– Polar coordinates

Polar coordinates are defined by combining the centrdoid distance $cd(n)$ and the polar angle θ as illustrated in Fig.1.3.7 and can be computed as:

$$PC(n) = cd(n) + j\,\theta(n)$$
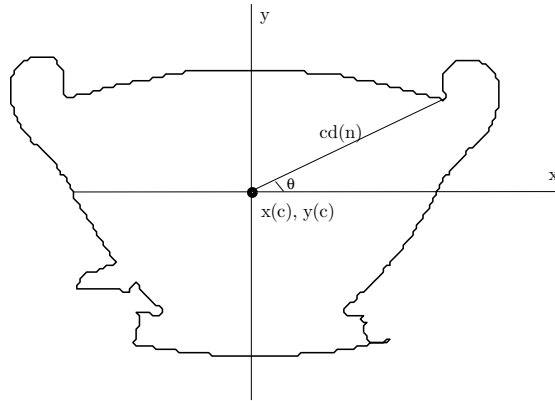
Figure 1.3.7: Illustration of the $PC(n)$ signature.

1.3.2.4 Wavelets

Fourier analysis has been a traditional and efficient tool in many fields of science and engineering, in the past two hundred years and Fourier descriptors are introduced to overcome the drawbacks of existing shape representation techniques. But they have also disadvantages such that they use the whole boundary information of the shape and cannot extract local characteristics thus Wavelet descriptors are defined to avoid the drawback of Fourier descriptors (Dang et al., 2006). Wavelets are functions that satisfy certain mathematical requirements and provide a powerful tool for image decomposition and analysis. Wavelets are a very popular tool in image processing. Several extensions to wavelets have been developed over the years. An example of these is sigmoidality descriptors introduced by Rosin (2003b) and elongation descriptor introduced by Stojmenović and Žunić (2008). They are also used in several applications such as: Recognition of Handprinted Characters, Characterization of Dirac-Edges, Step-Edge Detection, Face Recognition, Iris Pattern Recognition, Document Analysis, etc. (Tang, 2000)

1.3.3   Histogram Based Shape Descriptors

1.3.3.1   Shape Context

Shape context (Belongie et al., 2000) is another way of describing shapes that allows for measuring shape similarity. The basic idea is to pick a set $P = \{p_1, \ldots, p_n\}$, $p_i \in R^2$, of n points from an image (e.g. extracted from a set of detected edge elements) and consider the $n - 1$ vectors obtained by connecting p_i to all other sample points on a shape. The set of all these possible vectors is a rich description but using them as a shape descriptor is far too detailed. Thus, the authors of the paper (Belongie et al., 2000) used the distribution over relative positions as a robust, compact, and highly discriminative descriptor. So, for the selected point p_i from the set of points, they computed the coarse histogram h_i of the relative coordinates of the remaining $n - 1$ points as:

$$h_i(k) = \#\{q \neq p_i : (q - p_i) \in bin(k)\} \tag{1.3.30}$$

They defined this histogram as a shape context of p_i. Bins, which are normally taken to be uniform in log-polar space, have been used to make the descriptor more sensitive to nearest points than farthest points. To compute the cost of the matching two points p_i (from the first shape) and q_i (from the second shape) they used:

$$C_{ij} \equiv C(p_i, q_j) = \frac{1}{2} \sum_{k=1}^{K} \frac{[h_i(k) - h_j(k)]^2}{[h_i(k) + h_j(k)]}$$

1.3.3.2   Histogram of Oriented Gradients

HOG features have been introduced by Dalal and Triggs (2005) who have developed and tested several variants of HOG descriptors. The essential thought behind the Histogram of Oriented Gradient descriptors is that they explicitly exploited the distribution of intensity gradients or edge directions to characterize the local object appearance (Kobayashi et al., 2008; Newell and Griffin, 2011; Huang et al., 2011; Watanabe et al., 2009).

The implementation of these descriptors can be achieved by dividing the image into small connected regions, called cells, and for each cell computing a histogram of gradient directions or edge orientations for the pixels within the cell. The combination of these histograms then represents the descriptor.

Algorithm Implementation

– Gradient Computation

In order to compute the gradient, a grayscale image should first be filtered to obtain x and y pixel derivatives. Several gradient detectors have been used such as $[1, -1], [1, 0, -1], [1, -8, 0, 8, -1]$, Sobel (Sobel, 1970), etc. 1D centered point discrete derivative mask is one of the most commonly used method to filter the gray scale image. The mask should be applied in both the horizontal and vertical directions by using the following kernels:

$$D_x = [-1\,0\,1] \qquad D_y = [-1\,0\,1]^T \tag{1.3.31}$$

Then, convolution operation should be applied as follows to obtain the x and y derivatives of the given image I.

$$I_x = I * D_x \qquad I_y = I * D_y \tag{1.3.32}$$

After calculating x, y derivatives (I_x and I_y), the magnitude and orientation of the gradient should be computed as follows:

The magnitude of the gradient: $|G| = \sqrt{I_x^2 + I_y^2}$

The orientation of the gradient: $\theta = arctan\frac{I_y}{I_x}$

– **Orientation Binning**

The next step is to compute cell histograms for later use at descriptor blocks. Any HOG feature implementation must determine how many orientation bins to use in the histograms.

To form an orientation histogram, for each pixels orientation in the cell, the corresponding orientation bin should be found and the orientations magnitude $|G|$ should be voted to this bin.

– **Descriptor Blocks**

To normalize the cells orientation histograms, they should be grouped into blocks. There are two main block geometries available: rectangular R-HOG blocks and circular C-HOG blocks.

– **Block Normalization**

Gradient is affected by illumination changes thus, for better invariance to illumination and shadowing, it is useful to normalize the local responses before using them.

There are three different methods for block normalization which is defined as follows:

$$L2 - norm : f = \frac{v}{\sqrt{||v||_2^2 + e^2}}$$

$$L1 - norm : f = \frac{v}{||v||_1 + e}$$

$$L1 - sqrt : f = \sqrt{\frac{v}{||v||_1 + e}}$$

1.3.3.3 Spatial Pyramid Representation

In recent years, the bag-of-features (BoF) model has become popular in image processing (Jianchao et al., 2009). The main idea of this method is to consider an image as a set of unordered features which are extracted from local patches and then these

features are quantized into visual words, finally a compact histogram should be computed to represent the image for object recognition or scene categorization. The BoF model has some descriptive limitations because it discards the spatial order of local descriptors. Lazebnik et al. (2006) introduced one particular extension of the BoF model, called spatial pyramid representation (SPR), to overome the limitation of BoF model.

The SPR partitions an image into several subregions then computes the BoF histogram within each subregions and concatenates these histograms to construct a high dimensional vector which can be used to represent the image. First, SPR extracts the global feature from the input image (the top level $l = 0$). Next, the image is divided into a sequence of increasingly finer subregions on each pyramid level. Features are extracted from each subregion cell on each pyramid level l.

When comparing two images, the features that fall into the same corresponding cell in each image should be matched. This means that for each cell, a histogram should be constructed, and it should be matched to the corresponding cell's histogram in the other image. The number of matches at level l is given by the histogram intersection function (Swain and Ballard, 1991):

$$I(H_X^l, H_Y^l) = \sum_{i=1}^{D} min(H_X^l(i), H_Y^l(i)). \qquad (1.3.33)$$

Where D is the dimension of the cells, the histograms of X and Y have been denoted by H_X^l and H_Y^l and the number of points which fall into the ith cell of the subregion showed by $H_X^l(i)$ and $H_Y^l(i)$.

Spatial pyramids can be matched using the pyramid kernel, which weights features at higher levels more highly, reflecting the fact that higher levels localize the features more precisely. Pyramid match kernel has been defined as follows:

$$K^L(X, Y) = \frac{1}{2^L} I^0 + \sum_{l=1}^{L} \frac{1}{2^{L-l+1}} I^L. \qquad (1.3.34)$$

The histogram intersection and the pyramid matching kernel which is used in Lazebnik et al. (2006) are defined by Grauman and Darrell (2005)

1.4 Shape descriptor applications

As it has been mentioned before, shape descriptors are useful tools for extracting features and it is effective for many applications. For example, (Lee et al., 2011) have worked on an intelligent video security system and they used region-based shape descriptor and angular radial transform to model the human shape and track the human action.

Shape descriptors can be used in medical imaging to understand shape changes related to illness or aid surgical planning. For instance, deformable registration of images obtained from different modalities has been investigated by Mattias et al. (2011) and they defined a Non-local shape descriptor to overcome this problem. Furthermore, determining the Alzheimers disease using Teichmller Shape Descriptor has been studied in (Zeng et al., 2012) and Kazhdan et al. (2009), which defines a shape relationship descriptor for identifying similar constellations of tumor geometries from the patients database to transfer of treatment plans between patients with similar indications.

Color and texture based shape descriptors have been used in e-commerce (Gangopadhyay, 2001) to provide an efficient search system through product index where it is difficult to use a text to perform search. For example, it is hard to describe the style of the product by reliable words. Briefly, shape descriptors have been successfully used in a wide range of applications. In this section, I mention a small collection of examples where shape descriptors have been implemented.

In botany, leaf image classification is very useful for botanists. Scientists often identify plants by examining their flowers or fruits however leaves are often useful to identify a plant. In the study conducted by Ling and Jacobs (2007) the authors use Fourier shape descriptors to classify 15 different Swedish tree species, with 75 leaves per species. They achieved up to 95.33% accuracy by combining Fourier descriptors.

In (Rosin, 2003a), several methods (Ellipticity, Rectangularity, and Triangularity) defined in the paper have been used to distinguish a variety of seeds and beans. The best result (43.08%) is achieved when the combination of ellipticity and triangularity measures have been used. In the research which is considered in

(Zaker et al., 2012), the authors performed automatic measurement of the intensity of spontaneous facial action. They considered three facial action units: cheek raiser (AU6), lip corner puller (AU12), and lip stretcher (AU20) in infants, and evaluated these experiments by using different image representation methods (shape and grey scale texture, Histogram of Oriented Gradients (HOG), and Local Binary Patten Histograms (LBPH)). They showed that Shape and grey scale texture proved best for AU 12 (0.68) and AU 20 (0.69). For AU 6, they obtained similar results for grey scale texture (0.81) and for HOG (0.83). LPBH was the least effective for all three AUs (0.80 for AU 6, 0.24 for AU 12 and 0.63 for AU 20). Another shape descriptor application example is face recognition which is performed by Deniz et al. (2011). They used HOG-EBGM method and they achieved up to 95.5%.

Various classification examples can be found in Žunić et al. (2010) .They used circularity measure to classify mammograms into two groups (circumscribed speculated) and they achieved up to 90.74% classification accuracy. They again used circularity to classify galaxies in two groups: spiral and elliptical. When we consider that they used only one circularity measure, the results obtained are good. The last application was to measure print quality: The average correlation coefficient obtained is 0.77 which is favourable according to Žunić et al. (2010). Shape descriptors are also useful for security applications such as face recognition, fingerprint identification etc. A Practical Automatic Face Recognition System has been implemented by Sun et al. (1998) and the faces are identified by ellipse fitting. Fourier Descriptors have also been used for face recognition (Dampos et al., 2000).

1.5 Thesis context

As it can be seen from Section 1.3, shape descriptors have a wide range of applications. Chapters 2 to 4 of this thesis introduce some novel shape descriptors which can be applied to various applications in the same way as described above. The main contribution of this thesis is the development shape descriptors suitable for implementation in image processing applications. Each chapter provides some examples to illustrate how the developed descriptors can be applied. Notice that the examples

provided in each chapter are meant as an illustration of the possible applications and not as a definitive guide of application. As with all shape descriptors, these can be applied to a variety of applications, on their own or in combination with other descriptors.

1.5.1 Thesis structure

The rest of the thesis is structured as follows: Chapter 2 introduces a centredness measure which use both area and boundary information of the shape. Chapter 3 introduces two shape ellipticity methods which have different features to calculate shape ellipticity. Specific features, like setting the robustness of the measure, may be made more or less sensitive to the noise depending on a parameter. Chapter 4 introduces a familiy of ellipticity measures which can distinguish between ellipses whose ratio between the length of the major and minor axis differs. Chapter 5 concludes with a summary of the thesis and outlining some lines of future research.

1.5.2 List of publications

The work in this thesis has been submitted to various journals. The following is a list of conference and journal articles already published or under review:

- Joviša Žunić, Mehmet Ali Aktaş, Carlos Martinez-Ortiz, Antony Galton. (2011). The distance between shape centroids is less than a quarter of the shape perimeter. *Pattern Recognition*, 44(9):2161-2169

- Joviša Žunić, Mehmet Ali Aktaş, Carlos Martinez-Ortiz, Antony Galton, Shape Centredness Measure. *X Triennial International SAUM Conference on Systems, Automatic Control and Measurements Nis, Serbia, November 10th-12th, 2010*, pages 101-104.

- Mehmet Ali Aktaş, Joviša Žunić, Measuring shape ellipticity. in *CAIP'11: Proceedings of the 14th international conference on Computer analysis of images and patterns, 2011, - Volume 6854 Part I of LNCS*, pages 170-177, Berlin, Heidelberg Springer-Verlag.

- Mehmet Ali Aktaş, Joviša Žunić, Sensitivity/Robustness Flexible Ellipticity Measures. *Proceedings of the 34th DAGM and 36th OAGM Symposium, Graz, Austria, August 28-31, 2012. - Volume 7476 of LNSC*, pages 307-316, Berlin, Heidelberg. Springer-Verlag.

- Mehmet Ali Aktaş, Joviša Žunić. (2013). Family of Shape Ellipticity Measures for Galaxy Classification. *SIAM J. Imaging Sci.*, 6(2):765-781

Chapter 2

Shape Centredness Measure

This chapter includes material from:

> *Joviša Žunić, Mehmet Ali Aktaş, Carlos Martinez-Ortiz, Antony Galton. (2011). The distance between shape centroids is less than a quarter of the shape perimeter.* Pattern Recognition,*44(9):2161-2169*

and

> *Joviša Žunić, Mehmet Ali Aktaş, Carlos Martinez-Ortiz, Antony Galton, Shape Centredness Measure.* X Triennial International SAUM Conference on Systems, Automatic Control and Measurements Nis, Serbia, November 10th-12th, 2010,*pages 101-104.*

2.1   Introduction

Shape descriptors (Chen, 2005) are a useful tool in the area of many computer vision and image processing tasks (e.g. image retrieval, object classification, object recognition, etc). However, the fundamental problem of shape descriptors is the accurate extraction and representation of shape characteristics of objects regardless their size and orientation.As previously mentioned, various shape descriptors exist in the literature, mainly categorized into two groups: contour-based shape descriptors and region-based shape descriptors. Contour-based methods need extraction of boundary information which in some cases may not available. Region-based methods, however, do not rely on shape boundary information, but they take into account all

the pixels within the shape region. Contour-based shape descriptors includes Fourier descriptor (Zahn and Roskies, 1972; Bowman, 2001), wavelet descriptors (Chuang and Kuo, 1996) and curvature scale space (CSS) (Mokhtarian and Mackworth, 1992). Region-based shape descriptors includes moment invariants (Hu, 1962) and Zernike moments (Khotanzad and Hong, 1990).

Of course, there are other descriptors which cannot be strictly classified as area based or boundary based ones. Most well-known among them is the compactness, which considers the relation between the shape perimeter and shape area (Sonka et al., 2007).

In this chapter we introduce a new shape descriptor which also uses both the boundary points and the interior points of the shape considered. The new descriptor considers the distance between the shape centroids and assigns a higher value (here called the shape centredness) if such a distance is smaller.

The shape centredness, as defined here, is easy to compute and is invariant with respect to translation, rotation and scaling transformations. Several experiments are provided to illustrate the behaviour of the new measure.

2.2 Shape Centroids

Computation of the shape centroid is one of initial tasks in image normalisation processes. Often, the shape centroid is used to define the shape position. But they are also used to compute the dominant directions and approximate diameters of a region or they can be used to fit elliptic curve segments to extracted contours (Voss et al., 1995). The most common definition of the shape centroid is area based – i.e. it uses all the shape points for the computation, and informally speaking, defines the shape centroid as the point whose coordinates are the average values of the abscissas and ordinates of all the shape points. Let $\mathcal{C}_{area}(S)$ denote the centroid of S defined in such a way, then $\mathcal{C}_{area}(S)$ is formally defined as follows:

$$\mathcal{C}_{area}(S) = \left(\frac{\iint_S x \, dxdy}{\iint_S dxdy}, \ \frac{\iint_S y \, dxdy}{\iint_S dxdy} \right). \tag{2.2.1}$$

However, sometimes it is reasonable and very useful to analyse shape by using the boundary points only. Boundary based centroid is used in the literature to define a shape descriptor and used to determine the Location of the palm print (Li et al., 2011) or to classify the plants (Kue-Bum Lee, 2012). If the shape centroid has to be computed from the boundary points, then such a centroid, here denoted by $\mathcal{C}_{boundary}(S)$, is the point whose coordinates are equal to the average value of the abscissas and to the average value of the ordinates of the shape boundary points. Formally speaking, if the boundary $\mathcal{B}$ of S is given in an arc length parametrisation: $x = x(s)$, $y = y(s)$, where $s \in \left[0, \int_{\mathcal{B}} ds \right]$ (obviously $\int_{\mathcal{B}} ds$ is the perimeter of S) then

$$\mathcal{C}_{boundary}(S) = \left(\frac{\int_{\mathcal{B}} x(s)\ ds}{\int_{\mathcal{B}} ds}, \ \frac{\int_{\mathcal{B}} y(s)\ ds}{\int_{\mathcal{B}} ds} \right). \qquad (2.2.2)$$

As mentioned, shape centroid is used to define the shape position and, jointly with the computation of the shape orientation, is necessary part of image normalization procedures. Shape centroids are also used to define the translation invariants, like Hu invariants (Hu, 1962) or their boundary based analogues (Chen, 1993).

Another example of a use of shape centroids are the shape signatures (see Section 1.5.3). A shape signature is one-dimensional representation of planar shapes. Being one-dimensional objects, the signatures are easier for the further processing than two-dimensional objects are. There are several shape signatures already considered in literature which use the shape centroids as the reference points (El-ghazal et al., 2009; El Rube et al., 2006).

Throughout the chapter the following three conditions will be assumed even not mentioned.

(q-1) All shapes considered have a non-empty interior, i.e., $\iint_S dxdy > 0$, which implies that the area based centroids $\mathcal{C}_{area}(S)$ (see (2.2.1)) are well defined.

(q-2) Boundaries of all shapes considered are continuous curves. This implies that the boundary based centroids $\mathcal{C}_{boundary}(S)$ (see (2.2.2)) are well defined.

(q-3) Boundaries of all shapes considered have length equal to 1, i.e. $\int_{\mathcal{B}} ds = 1$.

2.3 Centeredness Measure

In this section we introduce the main result of the centeredness measure. The distance between the centroids $\mathcal{C}_{area}(S)$ and $\mathcal{C}_{boundary}(S)$ are considered and it is shown that this distance is upper bounded by a quarter of the perimeter of S.

Lemma 2.3.1 *Let a given shape S be scaled so that its perimeter $\int_{\mathcal{B}} ds$ is equal to 1. Also, let the boundary $\mathcal{B}$ of S be given in an arc length parametrisation form: $x = x(s)$, $y = y(s)$, $s \in [0,1]$. Then*

$$\|\mathcal{C}_{area}(S) - \mathcal{C}_{boundary}(S)\| \leq \frac{1}{4} \qquad (2.3.1)$$

Proof. Without loss of generality we can assume that the shape S is translated so that its area centroid $\mathcal{C}_{area}(S)$ coincides with the origin, i.e.

$$\left(\frac{\iint_S x \, dxdy}{\iint_S dxdy}, \frac{\iint_S y \, dxdy}{\iint_S dxdy} \right) = (0,0) \qquad (2.3.2)$$

and rotated so that its boundary centroid $\mathcal{C}_{boundary}(S)$ belongs to the nonnegative part of the x-axis, i.e. so that

$$\int_{\mathcal{B}} y(s) \, ds = 0 \qquad \text{and} \qquad \int_{\mathcal{B}} x(s) \, ds \geq 0 \qquad (2.3.3)$$

hold.

Since the shape S is positioned as stated in (2.3.2) and (2.3.3), then the distance $\|\mathcal{C}_{area}(S), \mathcal{C}_{boundary}(S)\|$ between the centroids of S can be expressed as follows

$$\|\mathcal{C}_{area}(S) - \mathcal{C}_{boundary}(S)\|$$

$$= \left\| \left(\frac{\iint_S x \, dxdy}{\iint_S dxdy}, \frac{\iint_S y \, dxdy}{\iint_S dxdy} \right), \left(\frac{\int_{\mathcal{B}} x(s) \, ds}{\int_{\mathcal{B}} ds}, \frac{\int_{\mathcal{B}} y(s) \, ds}{\int_{\mathcal{B}} ds} \right) \right\|$$

$$= \left\| (0,0), \left(\int_{\mathcal{B}} x(s)ds, \ 0 \right) \right\| = \sqrt{\left(\int_{\mathcal{B}} x(s)ds - 0 \right)^2} = \int_{\mathcal{B}} x(s)ds. \quad (2.3.4)$$

Thus, it remains to prove

$$\int_{\mathcal{B}} x(s) \, ds \ \leq \ \frac{1}{4}, \tag{2.3.5}$$

but we will prove the somewhat stronger inequality

$$\int_{\mathcal{B}} |x(s)| \, ds \ \leq \ \frac{1}{4}. \tag{2.3.6}$$

Because of (2.3.2), the boundary $\mathcal{B}$ intersects the y-axis, else all points of S would belong to one of two open half planes determined by the x-axis, which would imply that the assumed equality $\iint_S x \, dxdy = 0$ is not possible. Let A be one of the intersection points between the boundary $\mathcal{B}$ and the y-axis (see Fig.2.3.1), and let $\mathcal{B}$ be parametrised as follows:

$$\mathcal{B}: \ x = x(s), \ y = y(s), \ s \in [0,1], \ \text{such that} \ (x(0), y(0)) = (x(1), y(1)) = A. \tag{2.3.7}$$

Now, instead of the boundary $\mathcal{B}$ we consider the curve ϱ which is obtained from $\mathcal{B}$ by replacing each point $(x(s), y(s)) \in \mathcal{B}$ by the point $(|(x(s)|, y(s)) \in \mathcal{B}$. In other words, each points $(x(s), y(s)) \in \mathcal{B}$ lying on the left side of y-axis is replaced by the point $(-x(s), y(s))$, while the points lying on the right side of the y-axis and the points lying on the y-axis remain unchanged (see Fig.2.3.1). Thus, the parametrisation of the curve ϱ is:

$$\varrho: \ x = |x(s)|, \ y = y(s), \ s \in [0,1], \ \text{such that} \ (x(0), y(0)) = (x(1), y(1)) = A. \tag{2.3.8}$$

Further, let $a \in (0,1)$ be determined such that

$$\int_{s=0}^{a} |x(s)| \, ds \ = \ \int_{s=a}^{1} |x(s)| \, ds \ = \ \frac{1}{2} \cdot \int_{s=0}^{1} |x(s)| \, ds. \tag{2.3.9}$$

Notice that such a number a exists because $F(a) = \int_{s=0}^{a} |x(s)| \, ds$ is a continuous function, and consequently it reaches all values (including the value $\frac{1}{2} \cdot \int_{s=0}^{1} |x(s)| \, ds$) between the values $F(a=0) = 0$ and $F(a=1) = \int_{s=0}^{1} |x(s)| \, ds$.

Since s denotes the length between the points $A = (x(0), y(0))$ and $(|x(s)|, y(s))$ along the curve ϱ while s varies through $s = 0$ to $s = 1$, it must be that

$$|x(s)| \leq s. \tag{2.3.10}$$

This further gives (together with (2.3.9))

$$\int_\varrho |x(s)|\ ds \ = \ \int_{s=0}^{1} |x(s)|\ ds \ = \ 2 \cdot \int_{s=0}^{a} |x(s)|\ ds \ \leq 2 \cdot \int_{s=0}^{a} s\ ds \ = \ a^2. \tag{2.3.11}$$
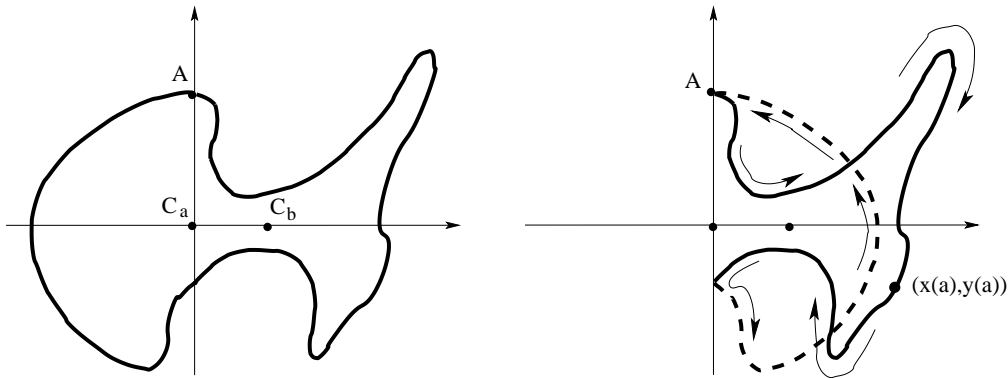
Figure 2.3.1: The boundary $\mathcal{B}$, given as $x = x(s)$, $y = y(s)$, $s \in [0, 1]$, is displayed on the left. The curve ϱ, defined as $x = |x(s)|$, $y = y(s)$, $s \in [0, 1]$, is displayed on the right. ϱ consist of two parts displayed as the solid and dashed line. The dashed line is reflective symmetric to the part of $\mathcal{B}$ lying in the half-plane $x < 0$.

Similarly, $1 - s$ denotes the length between the points $A = (x(0), y(0)) = (x(1), y(1))$ and $(|x(s)|, y(s))$ along the curve ϱ while s varies (this time in the opposite direction) through $s = 1$ to $s = 0$. So, it must be

$$|x(1 - s)| \leq s. \tag{2.3.12}$$

Further, the following analogue of (2.3.9)):

$$\int_{s=0}^{1-a} |x(1-s)|\ ds \ = \ \int_{s=1-a}^{1} |x(1-s)|\ ds \ = \ \frac{1}{2} \cdot \int_{s=0}^{1} |x(s)|\ ds \tag{2.3.13}$$

(together with (2.3.12)) gives

$$\int_{\varrho} |x(s)|\ ds\ =\ \int_{s=0}^{1} |x(s)|\ ds\ =\ 2\cdot\int_{s=0}^{1-a} |x(1-s)|\ ds\ \le 2\cdot\int_{s=0}^{1-a} s\ ds\ =\ (1-a)^2. \quad (2.3.14)$$

Finally (see (2.3.11) and (2.3.14)):

$$\left.\begin{array}{rcll} \displaystyle\int_{s=0}^{1} |x(s)|\ ds & \le & a^2, & a \in (0,1) \\[4mm] \displaystyle\int_{s=0}^{1} |x(s)|\ ds & \le & (1-a)^2, & a \in (0,1) \end{array}\right\} \quad \Rightarrow \quad \int_{s=0}^{1} |x(s)|\ ds\ \le\ \frac{1}{4} \quad (2.3.15)$$

establishes the proof. $\qquad\square$

The following lemma shows that the upper bound established by Lemma 2.3.1 is sharp.

Lemma 2.3.2 *For each $\delta > 0$ there is a shape S such that*

$$\|\mathcal{C}_{area}(S)\ -\ \mathcal{C}_{boundary}(S)\|\ \ge\ \frac{1}{4}\ -\ \delta. \quad (2.3.16)$$

Proof. We prove the statement of the theorem by showing that the distance between centroids of the shape $S(t)$ (displayed in Fig.2.3.2), is arbitrary close to 1/4, for a suitable choice of t.

The perimeter of $S(t)$ is 1. The centroids, $\mathcal{C}_{area}(S(t))$ and $\mathcal{C}_{boundary}(S(t))$, $S(t)$ (see Fig.2.3.2 and equations (2.2.1) and (2.2.2)) are as follows:

$$\begin{aligned} \mathcal{C}_{area}(S(t)) & = \left(\frac{1}{4}\cdot\frac{5t^3-4t^4}{2t^2+t^3-4t^4},\ \frac{1}{2}\cdot\frac{2t^3+t^6-4t^7}{2t^2+t^3-4t^4} \right), \\[4mm] \mathcal{C}_{boundary}(S(t)) & = \left(\frac{1}{4}-t+2t^2+\frac{t^3}{2}-2t^4,\ 2t^2+\frac{t^3}{2}-t^4 \right). \end{aligned} \quad (2.3.17)$$

Obviously, when $t \to 0$, we obtain

$$\lim_{t\to 0} \mathcal{C}_{area}(S(t)) = (0,0)\,, \qquad \lim_{t\to 0} \mathcal{C}_{boundary}(S(t)) = \left(\frac{1}{4},0\right). \quad (2.3.18)$$
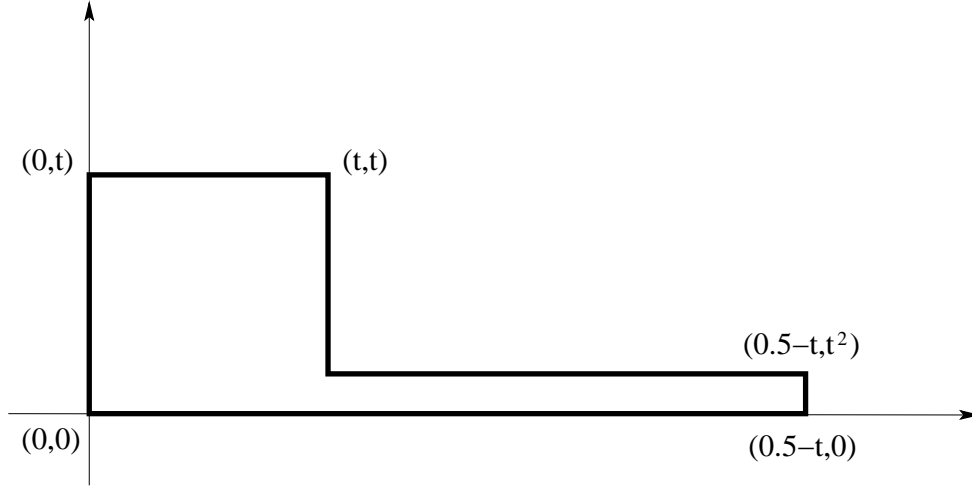
Figure 2.3.2: The shape $S(t)$ depends on the parameter t. As $t \to 0$, its area centroid converges to $(0,0)$ while the boundary centroid converges to $\left(\frac{1}{4}, 0\right)$.

Thus, as $t \to 0$, the area centroid $\mathcal{C}_{area}(S(t))$ approaches the origin $(0,0)$ while the boundary centroid $\mathcal{C}_{boundary}(S(t))$ approaches the point $\left(\frac{1}{4}, 0\right)$. In other words, for each $\delta > 0$, there is $t = t(\delta)$ such that

$$\|\mathcal{C}_{area}(S(t(\delta))) - \mathcal{C}_{boundary}(S(t(\delta)))\| \geq \frac{1}{4} - \delta. \qquad (2.3.19)$$

This establishes the proof. $\qquad \square$

Now, based on the results of Lemma 2.3.1 and Lemma 2.3.2, we introduce a new shape descriptor, named the *shape centredness*, as a quantity which should indicate to which degree the shape centroids coincide. We also give formula to compute the shape centredness. Such a defined shape centredness assigns a higher value to shapes whose centroids are close together and a lower value to shapes whose centroids are far away each other.

Definition 2.3.1 *Let S be a shape with a unit perimeter. Then the shape centredness* $\mathbf{C}(S)$ *of S is computed as*

$$\mathbf{C}(S) = 1 - 4 \cdot \|\mathcal{C}_{area}(S) - \mathcal{C}_{boundary}(S)\|. \qquad (2.3.20)$$

We give the following theorem which summarises the basic desirable properties of the new measure $\mathbf{C}(S)$.

Theorem 2.3.1 *Let S be a shape with a unit perimeter. Then the following statements hold:*

(a) $\mathbf{C}(S)$ *is well defined;*

(b) $\mathbf{C}(S)$ *ranges over* $(0, 1]$;

(c) $\mathbf{C}(S)$ *is invariant with respect to similarity transformations (e.g. translation, rotation and scaling transformations).*

Proof. Item **(a)** follows easily from the assumption that S has a nonempty interior and from the assumption that the boundary $\mathcal{B}$ of S is a continuous curve – i.e. all integrals appearing in (2.2.1) and (2.2.2) exist.

To prove the item **(b)** notice that $0 \leq \mathbf{C}(S) \leq 1$ is a direct consequence of Theorem 2.3.1 and Definition 2.3.1. To prove that $\mathbf{C}(S) \neq 0$ it is enough to notice that $\mathbf{C}(S) = 0$ (i.e. that the distance between the centroids is $1/4$) would imply that the both inequalities in (2.3.10) and (2.3.12) are equalities. Further, the equalities in (2.3.10) and (2.3.12) would imply that ϱ degenerates in two identical lines, which contradicts to the assumption that the shape S has a nonempty interior.

To prove the item **(c)**, first notice that $\|\mathcal{C}_{area}(S) - \mathcal{C}_{boundary}(S)\|$ is invariant with respect to rotations and translations. Since all measured shapes are scaled such that their perimeter is equal to 1, the shape centredness $\mathbf{C}(S)$ is scaling invariant too. $\square$

Remark. If we do not assume that the shapes considered are scaled such that their perimeter is equal to 1 then the formula (2.3.20) can be replaced with the equivalent one:

$$\mathbf{C}(S) = 1 - 4 \cdot \left\| \frac{\mathcal{C}_{area}(S) - \mathcal{C}_{boundary}(S)}{Perimeter\_of\_S} \right\| \tag{2.3.21}$$

and the items **(a)**, **(b)**, and **(c)** would follow again. The proof is trivial.

2.3.1 Shape Descriptors Used in Our Experiments

In this section we give a short overview of the shape descriptors used in experiments here. A particular attention is given to the descriptor introduced in Ladaga and

Bonetto (1998) which is defined as the ration between the shape centroid distances and shape diameter.

We start with the *shape compactness*, which is a very common shape descriptor. The shape compactness $\mathbf{K}(S)$ taking into account that, among all shapes with the same area, the circle has the minimal perimeter, a compactness measure can be defined as (see Sonka et al., 2007):

$$\mathbf{K}(S) \;=\; \frac{4 \cdot \pi \cdot Area\_of\_S}{(perimeter\_of\_S)^2} \tag{2.3.22}$$

Notice that the $\mathbf{K}(S)$ measure also uses both interior information (i.e. area) and boundary information (i.e. perimeter).

Another commonly used shape measures are the Hu's moment invariants (Hu, 1962), which are introduced almost 50 years ago, but are still a very interesting research topic (Xu and Li, 2008; Žunić et al., 2010). As already been mentioned in section 1.1 these quantities are invariant to translation and similarity transformations . In our experiments we will use the first three moment invariants $\mathbf{Hu}_1(S)$, $\mathbf{Hu}_2(S)$, and $\mathbf{Hu}_3(S)$ as mentioned in section 1.3.1.1.

$$\mathbf{Hu}_1(S) = \mu_{2,0}(S) + \mu_{0,2}(S)$$

$$\mathbf{Hu}_2(S) = (\mu_{2,0}(S) - \mu_{0,2}(S))^2 + 4 \cdot (\mu_{1,1}(S))^2$$

$$\mathbf{Hu}_3(S) = (\mu_{3,0}(S) - 3 \cdot \mu_{1,2}(S))^2 + (3 \cdot \mu_{2,1}(S) - \mu_{0,3}(S))^2$$

In addition, we will use the standard shape elongation measure, which also can be expressed in terms of moments (Sonka et al., 2007). The shape elongation is usually given in its 'traditional' form, such that it varies through the interval $[1, \infty)$. It will be denoted by $\mathbf{El}(S)$, and formally (in terms of moments) is defined as Eq.1.3.18.

In our experiments we will use the $1/\mathbf{El}(S)$ value of the standard elongation measure. In this way it is preserved that the measure used is not predominant (i..e. does not take too big values obviously $\mathbf{El}(S) \in (0, 1]$.) in shape matching and shape classification tasks, which will be performed later on.

Finally, we will use a shape descriptor introduced in Ladaga and Bonetto (1998) and here denoted as $\mathbf{ADR}(S)$ (meaning *asymmetries in the distribution of roughness*

index). The $\mathbf{ADR}(S)$ is defined as the ratio between the squared distance among shape centroids and the squared longest distance between two shape points. More formally,

$$\mathbf{ADR}(S) = \frac{||\ \mathcal{C}_{area}(S) - \mathcal{C}_{boundary}(S)||^2}{\mathbf{D}_f(S)^2} \tag{2.3.23}$$

where $\mathbf{D}_f(S)$ is the longest distance between two shape points (also known as maximum Feret diameter, or simply as the shape diameter). This measure is particularly interesting for us because it also uses the distance between shape centroids for its computation. The paper Ladaga and Bonetto (1998) does not give the upper bound of $\mathbf{ADR}(S)$ and this remains still an open problem. The lower bound is obviously 0.

   Remark. Before the experiment section it is good to mention that, although $\mathbf{ADR}(S)$ uses the same centroid distance ($||\ \mathcal{C}_{area}(S) - \mathcal{C}_{boundary}(S)||$) for the computation of the method, it does not mean that $\mathbf{ADR}(S)$ is assigning lower values for the shapes whose distance between shape centroids are small. This is simply because, for a small value of $||\ \mathcal{C}_{area}(S) - \mathcal{C}_{boundary}(S)||$, the shape diameter $\mathbf{D}_f(S)$ can be small as well. Thus, $1 - \mathbf{ADR}(S)$ may not be suitable to be used as an alternative centredness measure. A simple example is in Fig.2.3.3. The area centroid is marked with " $+$ " while the boundary centroid is marked with " $*$ ". Zig-zag section on the boundary of the shape presented is clearly detected by $\mathbf{C}(S)$ (the centrednes assigned is 0.873) while $\mathbf{ADR}(S)$ almost ignores this section and assigns the value $1 - \mathbf{ADR}(S) = 0.975$ (very close to 1 which is the value assigned to a perfect circle).
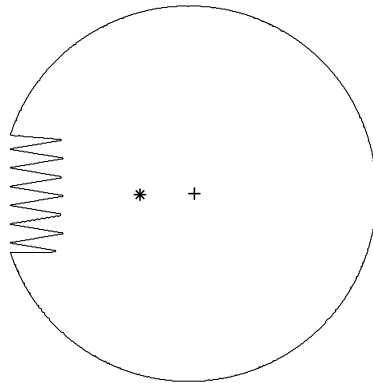
Figure 2.3.3: $1 - \mathbf{ADR}(S) = 0.975$ while $\mathbf{C}(S) = 0.873$.

2.4 Experiments

In this section we give several examples to illustrate how the new shape measure acts. First, we conduct experiments on synthetic shape . Synthetic shape experiments usually illustrate the behaviour of the method and their outcomes can be verified without using a computer. We also provide experiments for standard shape analysis tasks, as they are: shape ranking, shape matching and shape classification.

We start with a synthetic example displayed in Fig.2.4.1. Basically, from the proof of Lemma 1 we obtain an indication of which shapes have a relatively large distance between the centroids (i.e. which have a very small centredness). Informally, it can be said that most of the perimeter of such shapes should be concentrated on the other side from the side where the area is concentrated. A situation like this
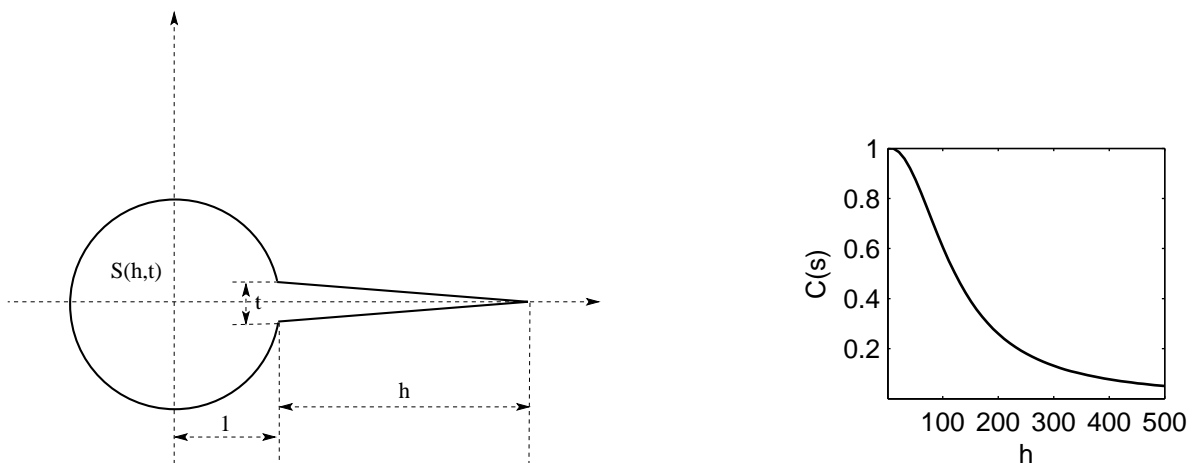
Figure 2.4.1: For a fixed and small t, the centredness measure $\mathbf{C}(S(h,t))$ depends on the spike length h. It decrease as the length of the spike h increases.

is presented in Fig.2.4.1 (in Fig.2.3.2, as well). A shape $S(h,t)$ depends on h which is the spike length and on t (the spike width). While the circular part of shape (the majority of the shape area) "carries" the area centroid to the left, the spike (the majority of the shape boundary) "carries" the boundary centroid to the right. How the measured centredness behaves, as the spike length varies (while the spike width is fixed and very small), is presented by the graph on the right, in the same figure. As expected, if h tends to 0 and t is very small, the shape centredness increases and in the limit case $h = 0$ it becomes equal to 1 (in this case the shape centroids approach each other because $S(h,t)$ tends to a circle, as $h, t \to 0$). On the other

side, if h increases, then the measured centredness $\mathbf{C}(S(h, t = 0))$ decreases and in the limit case $h \to \infty$ converge to 0. Indeed, if the spike width t tends to 0, we can say that $S(h, t = 0)$ consists of a circle C and two identical line segments L_1 and L_2. Without loss of generality, we can assume the situation as presented in Fig.2.4.1: The centroid of C coincides with the origin, i.e., $C = \{(x, y) \mid |x^2 + y^2 = 1\}$, and L_1 and L_2 belong to the x-axis. i.e. $L_1 = L_2 = \{(x, 0) \mid x \in [1, h]\}$. Now, entering: $Perimeter\_of\_S(h, t = 0) = 2\pi + 2h - 2$, $\mathcal{C}_{area}(S(h, t = 0)) = (0, 0)$ and $\mathcal{C}_{boundary}(S(h, t = 0)) = \left(\frac{h+1}{2}, 0\right)$ into (2.3.21) we obtain $\mathbf{C}(S(h, t = 0)) = \frac{\pi - 2}{\pi + h - 1}$. Obviously, $\lim_{h \to \infty} \mathbf{C}(S(h, t = 0)) = 0$, as shown by the graph in Fig.2.4.1.

As a second example, several shape ranking experiments have been performed. The behaviour of $\mathbf{C}(S)$ is illustrated by examples displayed in Fig.2.4.2 and 2.4.3. Two sets of shape are ranked in accordance with their centredness values. Several shapes, which correspond to the building silhouettes, are displayed in Fig.2.4.2 according to their increasing centredness. A lower centredness correspond to buildings having one or several towers. In those situations the shape centroids are relatively far away from each other. A higher centredness correspond to buildings without a tower. The centroids are relatively close to each other, while in the case of the rectangular silhouette the centroids coincide and the centredness is 1. The table below the shapes also includes the shape compactness $\mathbf{K}(S)$ as defined in equation 2.3.22 and $\mathbf{ADR}(S)$ as defined in equation 2.3.23. In the presented example, a higher $\mathbf{C}(S)$ measure correspond to a higher compactness measure. The case is opposite for $\mathbf{ADR}(S)$, higher $\mathbf{ADR}(S)$ measure correspond to a lower compactness measure. But this is not always the situation, as it will be shown by the next shape ranking example.

More shapes are shown in Fig.2.4.3. We could say that the centredness values are as we expected. The lower values correspond to the lamps with a long, thin body which makes most of the area to be located on lampshade. Higher centredness values belong to the lamps which have circular bodies, which implies an equally distributed area from top to bottom. Notice that while in the case of the shapes in Fig.2.4.2 the centredness and the compactness values assigned are consistent but

Shape	(a)	(b)	(c)	(d)	(e)	(f)
C(S)	0.8024	0.8376	0.8607	0.9535	0.9919	1.0000
K(S)	0.2503	0.3420	0.4245	0.6571	0.7249	0.7400
ADR(S)	0.0389	0.0182	0.0113	0.0012	0.0000	0.0000
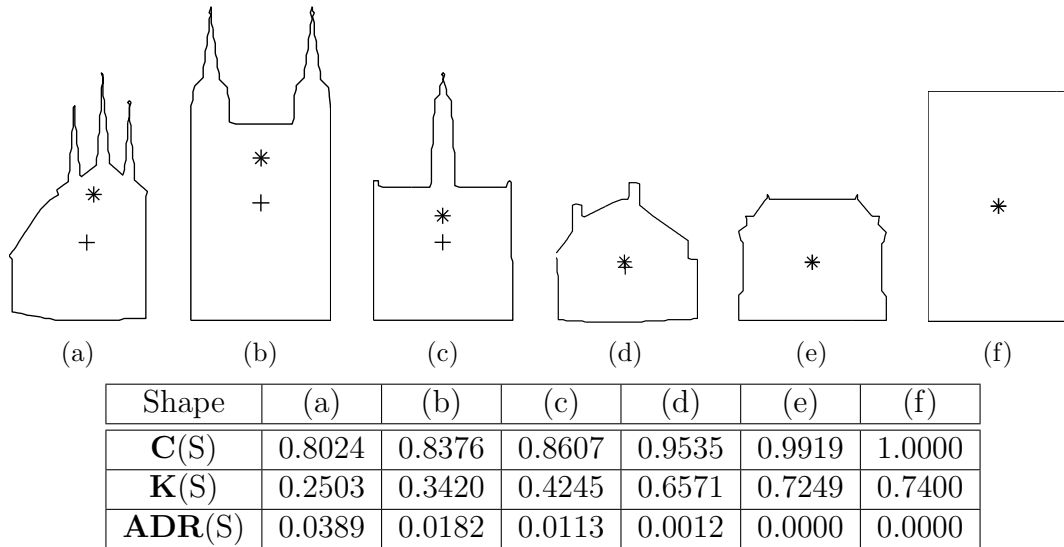
Figure 2.4.2: The displayed shapes correspond to buildings silhouettes. Their centredness, together with their compactness are given in the table below the shapes. The area centroids are marked with " + " while the boundary centroids are marked with " * "

$\mathbf{ADR}(S)$ values was opposite, in the case of the shapes in Fig.2.4.3, the rankings for the three methods are different. As a result of this experiment it is possible to say that compactness and centredness measures are not always consistent and $\mathbf{ADR}(S)$ measure is not always inverse because they give different rankings.

Obtained rankings are:

$\mathbf{C}$(S) :   (a), (b), (c), (d) (e), (f),

$\mathbf{K}$(S) :   (a), (d), (e), (c) (f), (b),

$\mathbf{ADR}$(S) : (f), (e), (d), (b), (c), (a),

As a third example we perform two shape matching (retrieval) experiments. The shapes used are from the well known Kimia database. In both figures, Fig.2.4.4 and Fig.2.4.5, the query shape is on the left (enclosed shape).

Five standard shape descriptors are used (the first three Hu's moment invariants (Hu, 1962), compactness and elongation (normalised such that varies through $(0, 1]$)) to perform shape matching (Fig.2.4.4). The best 9 matches (form the data base) are listed after the query shape (the first row).

Shape	(a)	(b)	(c)	(d)	(e)	(f)
C(S)	0.8272	0.8685	0.9156	0.9312	0.9858	0.9921
K(S)	0.2996	0.4024	0.3893	0.3498	0.3554	0.4003
ADR(S)	0.0362	0.0164	0.0214	0.0114	0.0069	0.0000
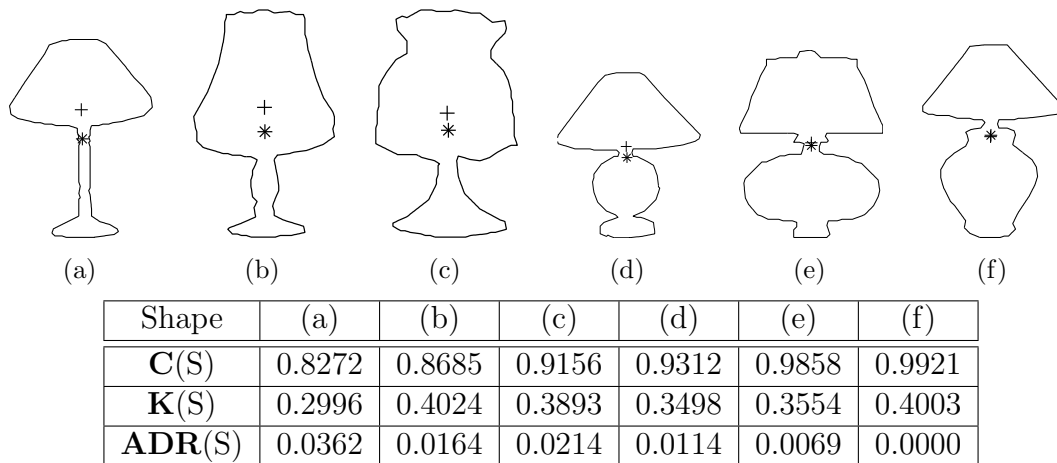
Figure 2.4.3: The displayed shapes correspond to buildings silhouettes. Their centredness, together with their compactness are given in the table below the shapes. The area centroids are marked with " + " while the boundary centroids are marked with " ∗ "
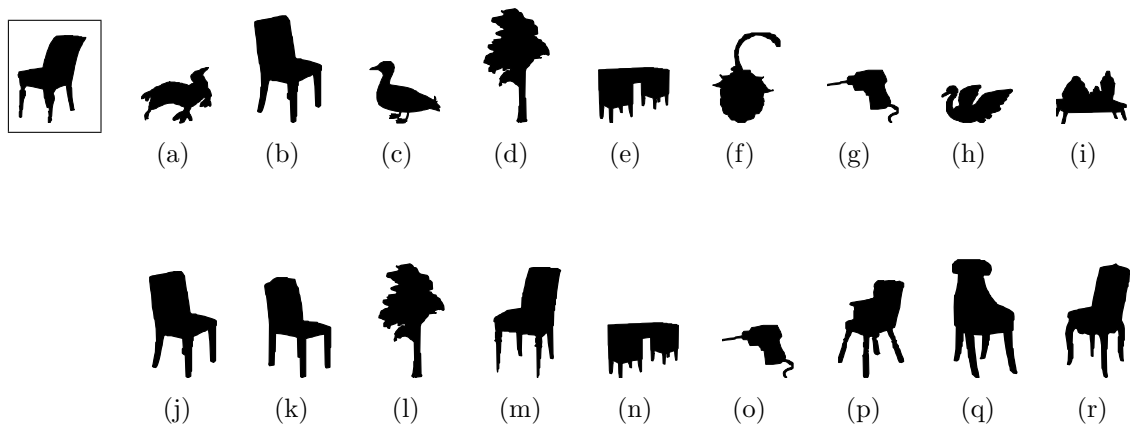
Figure 2.4.4: The query shape is on the left (enclosed shape). The first row: The best 9 matches, if the first three Hu's moment invariants, elongation and compactness are used. The second row: The best 9 matches if the centredness is added to the set of descriptors used.

After that, the centredness has been added to the set of shape descriptors used and shape matching is performed again. The best 9 matches obtained are in the second row. Even that objects of different kind may have similar shapes, and vice-versa, object of the same kind can appear as object of different shapes, our preference is that among the best matches we obtain, as many as possible, objects of the same king (i.e. objects from the same group/class). Adding the centredness **C**(S), to the set of descriptors used, leads to an obvious improvement in both experiments. Indeed, in the first experiment (Fig.2.4.4), the query shape was a chair and among 9 best matches there was only one chair, and, even worse, the best match was not

a chair (see the first row). The situation is essentially improved if the centredness is added to the set of descriptors used: Among the 9 best matches 6 of them were chairs, and the best 2 matches were chairs (see the second row in Fig.2.4.4).

	$\mathbf{C}(S)$	$\mathbf{Hu}_1(S)$	$\mathbf{Hu}_2(S)$	$\mathbf{Hu}_3(S)$	$\mathbf{El}(S)$	$\mathbf{K}(S)$
Query	0.8723	0.2566	0.0174	0.0015	0.3215	0.2100
M1(a)	0.9560*	0.2549	0.0175	0.0021	0.3164	0.1940
M1(b)	0.8720*	0.2583	0.0165	0.0010	0.3362	0.2221
M1(c)	0.9724*	0.2706	0.0185	0.0104	0.3311	0.2103
M1(d)	0.9143*	0.2432	0.0171	0.0039	0.3012	0.2173
M1(e)	0.9233*	0.2358	0.0155	0.0012	0.3091	0.1985
M1(f)	0.9543*	0.2832	0.0218	0.0092	0.3143	0.2230
M1(g)	0.9210*	0.2557	0.0169	0.0097	0.3265	0.2406
M1(h)	0.9552*	0.2282	0.0133	0.0019	0.3291	0.2244
M1(i)	0.9660*	0.2432	0.0154	0.0015	0.3244	0.2400
M2(j)	0.8720	0.2583	0.0165	0.0010	0.3362	0.2221
M2(k)	0.8694	0.2892	0.0228	0.0020	0.3142	0.1912
M2(l)	0.9143	0.2432	0.0171	0.0039	0.3012	0.2173
M2(m)	0.8527	0.2586	0.0178	0.0020	0.3187	0.1606
M2(n)	0.9233	0.2358	0.0155	0.0012	0.3091	0.1985
M2(o)	0.9210	0.2557	0.0169	0.0097	0.3265	0.2406
M2(p)	0.8814	0.2640	0.0169	0.0003	0.3401	0.1552
M2(q)	0.8875	0.2625	0.0222	0.0013	0.2761	0.1746
M2(r)	0.8649	0.2699	0.0224	0.0021	0.2870	0.1629

Table 2.4.1: Shape descriptor values computed for the shapes in Fig.2.4.4. Values in M1(a)-(i) rows relate to the shapes in the first row in Fig.2.4.4. $\mathbf{C}(S)$ values marked by * were not used in the first matching task. Values in M2(j)-(r) rows relate to the shapes in the second row in Fig.2.4.4.

Table 2.4.1 is added for a better understanding of the matching results obtained. It can be seen that the matches $M1(a) - (i)$ have similar $\mathbf{Hu}_1$, $\mathbf{Hu}_2$, $\mathbf{Hu}_3$, $\mathbf{El}(S)$ and $\mathbf{K}(S)$ values to the corresponding values of the query shape (the $\mathbf{C}(S)$ values, denoted by *, were not used for the matching, but they are needed for an explanation of the matching results). The corresponding centrednes $\mathbf{C}(S)$ values of the shapes M1(a), M1(c), M1(f), M1(h) and M1(i) are essentially different (all bigger than 0.9543) from the centredness (0.8723) of the query shape. But the centrednes was not used for the matching, in the first instance. Once the centrednes was added to the set of the descriptors (the second row in Fig.2.4.4), the situation has changed, and shapes whose centrednes differs essentially from the centrednes of the query shape were not among the 9 best matches. Of course, the selected shapes M2(j)-(r) have the values of all descriptors used pretty much similar to the corresponding values of the query shape.

For the second matching example we compared the matching performance of centredness measure with ADR. A building silhouette shape was the query shape (the enclosed shape on the left in Fig.2.4.5) in the second matching task. When the descriptors: $\mathbf{Hu}_1$, $\mathbf{Hu}_2$, $\mathbf{Hu}_3$, were used, four building shape was among the 9 best matches (the first row). Once the centredness is added to the shape descriptors used, the situations is again essentially improved. Seven building shapes were among the 9 best matches (the second row). When the ADR is added to the shape descriptors used, the situations is not very much improved. Five building shapes were among the 9 best matches (the third row). Centredness performed better for this matching experiment.

(a)

(b)

(c)
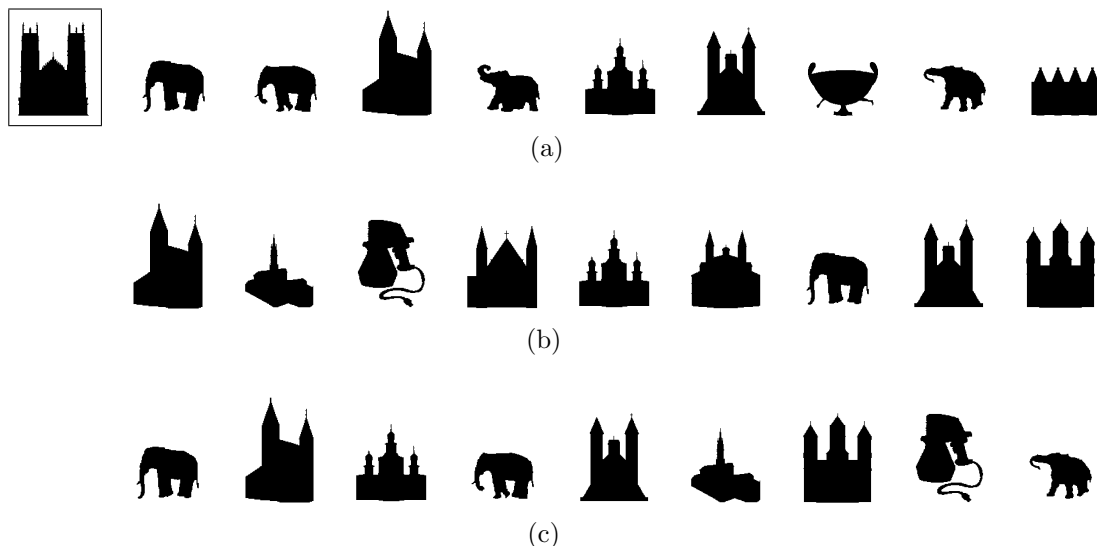
Figure 2.4.5: The query shape is on the left (enclosed shape). The first row: The best 9 matches, if the first three Hu's moment invariants are used. The second row: The best 9 matches if the centredness is added to the set of descriptors used. The second row: The best 9 matches if the ADR is added to the set of descriptors used.

For the other example in this section, we perform a number of classification tasks. Several combinations of descriptors $\mathbf{Hu}_1$, $\mathbf{Hu}_2$, $\mathbf{Hu}_3$, $\mathbf{El}(S)$, $\mathbf{K}(S)$, $\mathbf{ADR}(S)$ and $\mathbf{C}(S)$ were used for the classification. Classification tasks were performed on a shape set consisting of 150 shapes belonging to 5 classes: buildings, chairs, candelabrum, stars and trousers (taken from the Kimia database). Figure 2.4.6 shows one sample image from each of these classes. The classification was made using a k nearest neighbour classifier (kNN), with the value of k arbitrarily set to $k = 5$. The classification results obtained are in Table 2.4.2.

An explanation of the classification results follow.

Figure 2.4.6: Sample shapes from each class used in the classification experiment.

1.) In the first classification task, the initial set of descriptors:

$$\mathbf{Hu}_1(S), \quad \mathbf{Hu}_2(S), \quad \mathbf{Hu}_3(S), \quad \mathbf{El}(S), \quad \text{and} \quad \mathbf{K}(S) \tag{2.4.1}$$

where used. The classification rate 62.96% was obtained.

2.) In the next experiment, $\mathbf{ADR}(S)$ has been added to the initial set (2.4.1) of shape descriptors. The classification rate has been improved to 68.89%.

3.) In the third classification experiment, the centredness $\mathbf{C}(S)$ has been added to the set of initial descriptors (2.4.1) and classification rate has been further improved to 73.33%. This experiments also demonstrates that $\mathbf{C}(S)$ are $\mathbf{ADR}(S)$ essentially different (otherwise the classification rate in the second and the third experiment would not differ essentially).

Descriptor set	Class. rate
1.) $\mathbf{K}(S)$, $\mathbf{Hu}_1(S)$, $\mathbf{Hu}_2(S)$, $\mathbf{Hu}_3(S)$, $\mathbf{El}(S)$	62.96%
2.) $\mathbf{K}(S)$, $\mathbf{Hu}_1(S)$, $\mathbf{Hu}_2(S)$, $\mathbf{Hu}_3(S)$, $\mathbf{El}(S)$ and $\mathbf{ADR}(S)$	68.89%
3.) $\mathbf{K}(S)$, $\mathbf{Hu}_1(S)$, $\mathbf{Hu}_2(S)$, $\mathbf{Hu}_3(S)$, $\mathbf{El}(S)$ and $\mathbf{C}(S)$	73.33%
4.) $\mathbf{K}(S)$, $\mathbf{Hu}_1(S)$, $\mathbf{Hu}_2(S)$, $\mathbf{Hu}_3(S)$, $\mathbf{El}(S)$ and $\mathbf{C}(S)$, $\mathbf{ADR}(S)$	73.33%
5.) $\mathbf{K}(S)$, $\mathbf{Hu}_1(S)$, $\mathbf{Hu}_2(S)$, $\mathbf{Hu}_3(S)$, $\mathbf{El}(S)$ and $\sqrt{\mathbf{ADR}(S)}$	75.56%
6.) $\mathbf{K}(S)$, $\mathbf{Hu}_1(S)$, $\mathbf{Hu}_2(S)$, $\mathbf{Hu}_3(S)$, $\mathbf{El}(S)$ and $\mathbf{C}(S)$, $\sqrt{\mathbf{ADR}(S)}$	77.78%

Table 2.4.2: Classification accuracy: Different descriptor sets and kNN (k=5) are used.

4.) Interestingly, by adding both $\mathbf{C}(S)$ and $\mathbf{ADR}(S)$ to the initial set of descriptors, the classification rate has not changed – it remains 73.33%, as in the third experiment. Looking for the reason why an improvement did not happen (or, at least, why the classification rate has not been changed), we come to a conclusion that this is because $\mathbf{ADR}(S)$ varies through a short interval $[0, 0.0428]$, for shapes from the selected data set. Because the interval $[0, 0.0428]$ is so short, the measure $\mathbf{ADR}(S)$ is not expected to distinguish well among the shapes classified.

Thus, in the next two experiments, $\sqrt{\mathbf{ADR}(S)}$ was used instead of $\mathbf{ADR}(S)$. There were two reasons for such replacement:

- Since $\sqrt{\mathbf{ADR}(S)}$ varies through the interval $[0, 0.207]$, which is a wider interval than the interval $[0, 0428]$, it is expected that the replacement of $\mathbf{ADR}(S)$ with $\sqrt{\mathbf{ADR}(S)}$ will increase the classification rate.

- The definition of $\mathbf{ADR}(S)$ considers the squared distance of among the shape centroids (see (2.3.23)). If we consider $\sqrt{\mathbf{ADR}(S)}$ then the distance among the shape centroids (divided by the diameter of the shape considered) will be involved, what is our preference since we are studying a measure which is linearly dependent on the distance between centroids.

5.) In the fifth classification experiment, $\sqrt{\mathbf{ADR}(S)}$ has been used with the initial set (2.4.1) of shape descriptors. The $\mathbf{ADR}(S)$ measure performed better than $\sqrt{\mathbf{ADR}(S)}$ and $\mathbf{C}(S)$ measure. The classification rate 75.56% was obtained.

6.) Finally, once both $\sqrt{\mathbf{ADR}(S)}$ and $\mathbf{C}(S)$ are added to the initial set of descriptors, the highest classification rate 77.78% was reached. Since the classification accuracy has increased, with respect to the fourth classification experiment performed here, we conclude that $\sqrt{\mathbf{ADR}(S)}$ and $\mathbf{C}(S)$ are clearly correlated.

Two more examples have been performed. In Table 2.4.3 Z-score normalization has been applied to the same data which is used in experiment illustrated in Table 2.4.2. The same classification tasks were performed and the results of the classification accuracies are listed in Table 2.4.3. In this experiment the three measures $\mathbf{C}(S)$, $\mathbf{ADR}(S)$ and $\sqrt{\mathbf{ADR}(S)}$ performed identically. Moreover, using the $\mathbf{C}(S)$ and $\mathbf{ADR}(S)$ together with the other shape descriptors did not improve the result but using the $\mathbf{C}(S)$ and $\sqrt{\mathbf{ADR}(S)}$ together with the other shape descriptors slightly improved the classification accuracy.

In Table 2.4.4 Min-Max normalization has been applied to the same data which is used in experiment illustrated in Table 2.4.2. All the measures have been scaled to be between 0 and 1. The same classification tasks were performed and the results

of the classification accuracies are listed in Table 2.4.4. In this experiment $\mathbf{C}(S)$ performed better than the $\mathbf{ADR}(S)$ measure but $\sqrt{\mathbf{ADR}(S)}$ gave the best classifciation accuracy. Moreover, this time, using the $\mathbf{C}(S)$ and $\mathbf{ADR}(S)$ together with the other shape descriptors improved the result but using the $\mathbf{C}(S)$ and $\sqrt{\mathbf{ADR}(S)}$ together with the other shape descriptors caused the classifcaiton accuracy to decrease.

Descriptor set	Class. rate
1.) $\mathbf{K}(S)$, $\mathbf{Hu}_1(S)$, $\mathbf{Hu}_2(S)$, $\mathbf{Hu}_3(S)$, $\mathbf{El}(S)$	66.67%
2.) $\mathbf{K}(S)$, $\mathbf{Hu}_1(S)$, $\mathbf{Hu}_2(S)$, $\mathbf{Hu}_3(S)$, $\mathbf{El}(S)$ and $\mathbf{ADR}(S)$	77.33%
3.) $\mathbf{K}(S)$, $\mathbf{Hu}_1(S)$, $\mathbf{Hu}_2(S)$, $\mathbf{Hu}_3(S)$, $\mathbf{El}(S)$ and $\mathbf{C}(S)$	77.33%
4.) $\mathbf{K}(S)$, $\mathbf{Hu}_1(S)$, $\mathbf{Hu}_2(S)$, $\mathbf{Hu}_3(S)$, $\mathbf{El}(S)$ and $\mathbf{C}(S)$, $\mathbf{ADR}(S)$	77.33%
5.) $\mathbf{K}(S)$, $\mathbf{Hu}_1(S)$, $\mathbf{Hu}_2(S)$, $\mathbf{Hu}_3(S)$, $\mathbf{El}(S)$ and $\sqrt{\mathbf{ADR}(S)}$	77.33%
6.) $\mathbf{K}(S)$, $\mathbf{Hu}_1(S)$, $\mathbf{Hu}_2(S)$, $\mathbf{Hu}_3(S)$, $\mathbf{El}(S)$ and $\mathbf{C}(S)$, $\sqrt{\mathbf{ADR}(S)}$	78.67%

Table 2.4.3: Classification accuracy results for the Z-score normalized data: Different descriptor sets and kNN (k=5) are used.

Descriptor set	Class. rate
1.) $\mathbf{K}(S)$, $\mathbf{Hu}_1(S)$, $\mathbf{Hu}_2(S)$, $\mathbf{Hu}_3(S)$, $\mathbf{El}(S)$	68.00%
2.) $\mathbf{K}(S)$, $\mathbf{Hu}_1(S)$, $\mathbf{Hu}_2(S)$, $\mathbf{Hu}_3(S)$, $\mathbf{El}(S)$ and $\mathbf{ADR}(S)$	76.00%
3.) $\mathbf{K}(S)$, $\mathbf{Hu}_1(S)$, $\mathbf{Hu}_2(S)$, $\mathbf{Hu}_3(S)$, $\mathbf{El}(S)$ and $\mathbf{C}(S)$	78.67%
4.) $\mathbf{K}(S)$, $\mathbf{Hu}_1(S)$, $\mathbf{Hu}_2(S)$, $\mathbf{Hu}_3(S)$, $\mathbf{El}(S)$ and $\mathbf{C}(S)$, $\mathbf{ADR}(S)$	80.00%
5.) $\mathbf{K}(S)$, $\mathbf{Hu}_1(S)$, $\mathbf{Hu}_2(S)$, $\mathbf{Hu}_3(S)$, $\mathbf{El}(S)$ and $\sqrt{\mathbf{ADR}(S)}$	80.00%
6.) $\mathbf{K}(S)$, $\mathbf{Hu}_1(S)$, $\mathbf{Hu}_2(S)$, $\mathbf{Hu}_3(S)$, $\mathbf{El}(S)$ and $\mathbf{C}(S)$, $\sqrt{\mathbf{ADR}(S)}$	78.67%

Table 2.4.4: Classification accuracy results for the Min-Max normalized data: Different descriptor sets and kNN (k=5) are used.

2.5 Conclusion

In this section we have considered the distance between the area centroid and boundary centroid of a given shape. It has been shown that this distance is upper bounded by a quarter of the shape perimeter, i.e. by 1/4 if the considered shape is scaled so that its perimeter is equal to 1. We have also proved that this upper bound is sharp and it cannot be improved. In other words, for arbitrarily small $\delta > 0$ there is always a shape whose centroids are at a distance bigger than $\frac{1}{4} - \delta$. Trivially, the

minimum distance between a shape's centroids is 0 and many shapes achieve this value: circles, squares, etc, but also many irregular shapes.

We exploit such a sharp upper bound to define a new shape descriptor. We named it shape centredness and intended it to be an indicator of the degree to which the shape centroids coincide or informally, to which degree a shape has the uniquely defined centre (centroid is sometimes called centre of gravity or centre of mass). The centredness $\mathbf{C}(S)$ of a given shape S (scaled such that it has perimeter equal to 1) is computed by the formula

$$\mathbf{C}(S) \ = \ 1 - 4 \cdot ||\mathcal{C}_{area}(S) - \mathcal{C}_{boundary}(S)||$$

which provides that the measured centredness varies through the interval $(0, 1]$ and reaches a higher value if the shape centroids are closer to each other. We also showed that the new measure is invariant with respect to translation, rotation and scaling transformations, which is always desirable when dealing with problems which involve the shape analysis tools.

Being theoretically well founded, the centredness behaviour can be understood well and situations where the centredness would act well could be predicted (to the some extent) in advance. For example, it is easy to predict that differentiating a fruit without stalk e.g. Orange and a fruit with stalk e.g. cherry is possible. Because the stalk of the cherry is going to cause the boundary centroid to move far from the area based centroid on the direction of the stalk. But, for the orange, because orange is an almost circular fruit, the both centroid of the orange shape is not going to be too far from each other. We have used Kimia's shape data set to verify usefulness of the new measure. The measure has performed well and resulted in improved accuracy in shape matching and shape classification tasks once the new descriptor is added to a set of other shape descriptors.

Chapter 3

Measuring shape ellipticity

This chapter includes material from:

> *Mehmet Ali Aktaş, Joviša Žunić, Measuring shape ellipticity. in* CAIP'11: Proceedings of the 14th international conference on Computer analysis of images and patterns - Volume 6854 Part I of LNCS,*pages 170-177, Berlin, Heidelberg Springer-Verlag.*

and

> *Mehmet Ali Aktaş, Joviša Žunić, Sensitivity/Robustness Flexible Ellipticity Measures.* Proceedings of the 34th DAGM and 36th OAGM Symposium, Graz, Austria, August 28-31, 2012. - Volume 7476 of LNSC,*pages 307-316, Berlin, Heidelberg. Springer-Verlag*

3.1   Introduction

As it was mentioned in section 1.2.1 a number of shape descriptors have been developed which can be generally divided in two groups: boundary and area based. Many shape descriptors were created and used. Some of them are quite generic: such as, Fourier descriptors (Bowman, 2001) and moment invariants (Hu, 1962). Alternatively, there are shape descriptors which use a single characteristic of shapes: Sigmoidality (Rosin, 2003b), linearity (Stojmenović et al., 2008), rectilinearity (Žunić and Rosin, 2003), symmetry (Zabrodsky et al., 1995), etc.

This section introduces another global shape descriptor: *shape ellipticity*. Ellipse

is a basic shape widely applied to a vast range of image processing tasks involving not only man-made objects, but also natural forms. The problems like: Identifying certain grains, onions, watermelons, cells, human faces and it is also used to ensure the quality of steel coils before they are shipped out (Stojmenovic and Nayak, 2007; Schleicher and Zagar, 2008). Moreover, how to determine the ellipse which fits best to the data considered, or how to evaluate how much a shape given differs from a perfect ellipse, have already been studied in literature (Fitzgibbon et al., 1999; Peura and Iivarinen, 1997; Proffitt, 1982; Rosin, 2003a; Sonka et al., 2007). Different techniques were employed – e.g. Discrete Fourier Transform (Proffitt, 1982), or affine moment invariants (Rosin, 2003a).

3.2 Ellipticity

Two ellipticity measures are defined in this chapter. First, an overview about the existing ellipticity measures will be given, then basic ellipticity measure will be introduced and lastly sensitive ellipticity measure will be defined. All the new ellipticity measures introduced here indicate the degree to which a given shape differs from a perfect ellipse. The ellipticity measure ranges over the interval $(0, 1]$ and reaches its maximum value 1 if and only if the measured line is a perfect ellipse. The measure is invariant with respect to translations, rotations and scaling transformations.

3.2.1 Comparable Ellipticity Measures

As it was mentioned in the previous section several methods have already been studied in literature. As expected, all the existing ellipticity measures have their own strengths and weaknesses, and it is not possible to establish a strict ranking among them. Measures which perform well in some tasks can have poor performance in others.

We begin with a short overview, of the comparable ellipticity measures, with a recent measure $\mathcal{E}_I(S)$ presented by Rosin (2003a). The measure $\mathcal{E}_I(S)$ varies through the interval $[0, 1]$ and picks the value 1 when the considered shape S is an ellipse. The problem is that $\mathcal{E}_I(S) = 1$ does not guaranty (or at least this has not been

proven) that the measured shape S is a perfect ellipse. Also, since $\mathcal{E}_I(S)$ is defined by using a projective invariant (Flusser and Suk, 1993), it does not change the assigned ellipticity measure when an affine transformation is applied to the object considered. Of course, in some applications this property can be an advantage, but in some other applications it can be a disadvantage. For instance, when an application needs to differentiate a circle and an ellipse it is not possible with $\mathcal{E}_I(S)$ measure because it is using affine moment invariant thus it is going to assign same value for these two shapes (ellipse and circle). But the ellipticity measures which are defined in this chapter can differentiate these two shapes (ellipse and circle). For this situation, using a method, which is an affine transformation applied, is a disadvantage.

On the other side, if the application needs to differentiate circle, ellipse and triangle and if the circle and ellipse should be classified as the same class than using the method which assign the same value to the shapes (ellipse and circle) is an advantage. This time, the ellipticity measure $\mathcal{E}_I(S)$ is more suitable for this situation.

$\mathcal{E}_I(S)$ uses the following affine moment invariant (Flusser and Suk, 1993):

$$I(S) = \frac{\mu_{20}(S) \cdot \mu_{02}(S) - \mu_{11}^2(S)}{\mu_{00}^4(S)} \qquad (3.2.1)$$

and is defined as follows:

$$\mathcal{E}_I(S) = \begin{cases} 16 \cdot \pi^2 \cdot I(S) & \text{if} \quad I(S) \leq \dfrac{1}{16\pi^2} \\[3mm] \dfrac{1}{16 \cdot \pi^2 \cdot I(S)} & \text{otherwise.} \end{cases} \qquad (3.2.2)$$

where, the ellipticity measure $\mathcal{E}_I(S)$ is equal to $16 \cdot \pi^2 \cdot I(S)$ if $I(S) \leq \dfrac{1}{16\pi^2}$ else the ellipticity measure $\mathcal{E}_I(S)$ is equal to $\frac{1}{16 \cdot \pi^2 \cdot I(S)}$.

The quantities $\mu_{p,q}(S) = \iint_S \left(x - \frac{\iint_S x\,dx\,dy}{\iint_S dx\,dy} \right)^p \left(y - \frac{\iint_S y\,dx\,dy}{\iint_S dx\,dy} \right)^q dx\,dy$, appearing in (3.2.1), are well known as the centralized moments.

There are also some standard approaches which can be used to define an el-

lipticity measure. For example, the most common method (Sonka et al., 2007) to determine an ellipse $E_f(S)$ which fits with a given shape S, also uses the moments for the computation. The axes of $E_f(S)$ are (Sonka et al., 2007):

$$major - axis: \quad \sqrt{\mu_{2,0}(S) + \mu_{0,2}(S) + \sqrt{4 \cdot (\mu_{1,1}(S))^2 + (\mu_{2,0}(S) - \mu_{0,2}(S))^2}} \tag{3.2.3}$$

$$minor - axis: \quad \sqrt{\mu_{2,0}(S) + \mu_{0,2}(S) - \sqrt{4 \cdot (\mu_{1,1}(S))^2 + (\mu_{2,0}(S) - \mu_{0,2}(S))^2}}. \tag{3.2.4}$$

The angle φ between the major axis of $E_f(S)$ and the x-axis is computed from

$$\tan(2 \cdot \varphi) = \frac{2\mu_{11}(S)}{\mu_{20}(S) - \mu_{02}(S)}. \tag{3.2.5}$$

Now, we can define an ellipticity measure $\mathcal{E}_f(S)$ by comparing a given shape S and the ellipse $SE_f(S)$, which is actually the ellipse $E_f(S)$ scaled such that the area of S and the area of $E_f(S)$ coincide. A possible definition is:

$$\mathcal{E}_f(S) = \frac{Area(S \cap SE_f(S))}{Area(S \cup SE_f(S))}. \tag{3.2.6}$$

The angle φ, defined as in (3.2.5), is very often used to define the shape orientation Sonka et al. (2007). The problem is that this method for the computation of the shape orientation fails in many situations, but also can be very unreliable (Žunić et al., 2006). For example, it is not possible to find a single angle φ for n-fold rotationally symmetric shapes. Because of that, we modify the $\mathcal{E}_f(S)$ measure by replacing $SE_f(S)$ in (3.2.6) by rotating $SE_f(S)$ around the centroid for an angle θ which maximizes the area of $S \cap SE_f(S)$. If such a rotated ellipse $SE_f(S)$ is denoted by $SE_f(S(\theta))$ then we define a new ellipticity measure $\mathcal{E}_{fm}(S)$ as:

$$\mathcal{E}_{fm}(S) = \frac{Area(S \cap SE_f(S(\theta)))}{Area(S \cup SE_f(S(\theta)))}. \tag{3.2.7}$$

All three measures $\mathcal{E}_I(S)$, $\mathcal{E}_f(S)$, and $\mathcal{E}_{fm}(S)$, mentioned above, as well as the new ellipticity measure, which will be defined in the next section, are area based. This means that all the interior points are used for their computation. Because of that, we

will say that all the shapes whose mutual set differences have the area equal to zero, are equal. For example, the shape of an open circular disc $\{(x,y) \mid x^2 + y^2 < 1\}$ and the shape of the closed one $\{(x,y) \mid x^2 + y^2 \leq 1\}$ will be considered as equal shapes. Obviously, this is not a restriction in image processing tasks, but will simplify our proofs.

3.2.2 Ellipticity Measure

As it has been noticed before, the ellipticity measure should provide an indication of how much the shape considered differs from a perfect ellipse. This section introduces the ellipticity measure. We define a new ellipticity measure and give some desirable properties of it. Throughout this section, it will be assumed, even not mentioned, that all appearing shapes have the unit area.

To describe the new ellipticity measure we need an auxiliary ellipse $E(S)$ which is defined as

$$E(S) \; = \; \left\{ (x,y) \mid \frac{x^2}{\psi} + \psi \cdot y^2 \leq 1 \right\}, \qquad (3.2.8)$$

where ψ is the ratio between the major-axis and the minor-axis of shape S, defined as in (3.2.3) and (3.2.4)

Now, To define the new ellipticity measure, we start with a Lemma that describes integral of the ellipse function over both the ellipse and the shape.

Lemma 3.2.1 *Let a given shape S whose area is 1 and whose centroid coincides with the origin. Let $S(\alpha)$ be the shape S rotated around the origin for an angle α, and let $\; Q(x,y) = \dfrac{x^2}{\psi} + \psi \cdot y^2, \;$ for a shorter notation. Then:*

(a) $\displaystyle \iint_{S} Q(x,y) \; dx \; dy \; = \; \iint_{E(S)} Q(x,y) \; dx \; dy \quad \Rightarrow \quad S = E(S);$

(b) $\displaystyle \min_{\alpha \in (0,2\pi]} \iint_{S(\alpha)} Q(x,y) \; dx \; dy \; = \; \frac{1}{2} \quad \Leftrightarrow \quad S$ *is an ellipse.*

Proof. *(a)* Since the areas of S and $E(S)$ are the same (both equal to 1) and all the points (x, y) satisfying $Q(x, y) = \dfrac{x^2}{\psi} + \psi \cdot y^2 \leq 1$ are inside the ellipse $E(S)$ (see (3.2.8)) we deduce

$$(x, y) \in E(S) \quad \text{and} \quad (u, v) \notin E(S) \quad \Rightarrow \quad Q(x, y) < Q(u, v). \tag{3.2.9}$$

Now, by using the above implication, we derive

$$\iint_S Q(x, y) \, dx \, dy = \iint_{S \setminus E(S)} Q(x, y) \, dx \, dy + \iint_{S \cap E(S)} Q(x, y) \, dx \, dy \geq$$

$$\iint_{E(S) \setminus S} Q(x, y) \, dx \, dy + \iint_{E(S) \cap S} Q(x, y) \, dx \, dy = \iint_{E(S)} Q(x, y) \, dx dy. \tag{3.2.10}$$

Finally, the required implication (in *(a)*) follows from the fact that the equality $\iint_S Q(x, y) dx dy = \iint_{E(S)} Q(x, y) dx dy$ holds if and only if

$$\iint_{S \setminus E(S)} Q(x, y) \, dx \, dy = \iint_{E(S) \setminus S} Q(x, y) \, dx \, dy = 0$$

(a direct consequence of (3.2.9) and (3.2.10)) – i.e., if the shapes S and $E(S)$ are equal.

(b) This item follows from *(a)*, which actually says that $\iint_{S(\alpha)} Q(x, y) dx dy$ reaches the minimum possible value $1/2$ (notice $1/2 = \iint_{E(S)} Q(x, y) dx dy$ and see (3.2.10)) if there is an angle α such that $S(\alpha) = E(S)$. $\qquad\square$

By the arguments of Lemma 3.2.1 we define the following ellipticity measure.

Definition 3.2.1 *Let a given shape S whose area is 1 and whose centroid coincides with the origin. The ellipticity $\mathcal{E}(S)$ of S is defined as*

$$\mathcal{E}(S) = \frac{1}{2} \cdot \frac{1}{\min\limits_{\alpha \in [0, 2\pi]} \iint_{S(\alpha)} \frac{x^2}{\psi} + \psi \cdot y^2} \tag{3.2.11}$$

where ψ is the elongation of S and $S(\alpha)$ denotes the shape S rotated around the origin for an angle α where α can be found by exhaustive search.

Now, we summarize desirable properties of $\mathcal{E}(S)$.

Theorem 3.2.1 *The ellipticity measure $\mathcal{E}(S)$ has the following properties:*

(a) $\mathcal{E}(S) \in (0, 1]$;

(b) $\mathcal{E}(S) = 1 \quad$ *if and only if $\quad S$ is an ellipse;*

(c) $\mathcal{E}(S)$ *is invariant with respect translation, rotation and scaling transformations.*

Proof. The proof of *(a)* and *(b)* follows from Theorem 1. The proof of *(c)* follows directly from the definition. Basic calculus is sufficient for a formal proof. □

3.2.3   Sensitivity/Robustness Flexible Ellipticity Measures

This section introduces a modification of definition 3.2.11 which allows the ellipticity measure to be more sensitive or robust. As highlighted in the previous chapter, a lot of research has been done on how to measure the shape ellipticity. Because the existing methods and the ellipticity method which defined in section 3.2.1 are area based, these methods are robust with respect to noise. When working with a low quality data, the methods being robust is a desirable property. But there are also situations where methods sensitive to the presence of noise or to small object deformations, are more preferred.

In this section we propose a new family of ellipticity measures. The ellipticity measures are dependent on a single parameter and by varying this parameter the sensitivity/robustness properties of the related ellipticity measures, vary as well.

Independently on the parameter choice, all the new ellipticity measures indicate the degree to which a given shape differs from a perfect ellipse. The ellipticity measures range over $(0, 1]$ and become 1 if and only if the shape considered is an ellipse. All the measures are invariant with respect to the translation, scaling, and rotation transformation.

To describe the new ellipticity measure we need an auxiliary ellipse $\mathbf{E}(S)$, defined for a given shape S, in the following way :

$$\mathbf{E}(S) \;=\; \left\{ (x,y) \mid \frac{\pi}{\rho(S)} \cdot x^2 + (\pi \cdot \rho(S)) \cdot y^2 \;\leq\; 1 \right\}. \qquad (3.2.12)$$

In the above equation $\rho(S)$ is the ratio between the major-axis and the minor-axis of S, defined as in (3.2.3) and (3.2.4). Notice that the areas of S and $\mathbf{E}(S)$ are the same and both equal to 1.

The ellipse $\mathbf{E}(S)$ can be expressed in many different ways. Indeed, let $\lambda > 0$ and let the function $\Phi_\lambda(x,y)$ be defined as

$$\Phi_\lambda(x,y) \;=\; \left(\frac{\pi}{\rho(S)} \cdot x^2 + (\pi \cdot \rho(S)) \cdot y^2 \right)^\lambda, \qquad (3.2.13)$$

then

$$\mathbf{E}(S) \;=\; \{(x,y) \mid \Phi_\lambda(x,y) \leq 1\} \qquad \text{for all } \lambda > 0. \qquad (3.2.14)$$

It is easy to see that regions on the right side of (3.2.12) and (3.2.14) are both bounded by the same curve given by the equation $\Phi_\lambda(x,y) = 1$, which does not depend on λ, i.e., the equations $\Phi_\lambda(x,y) = 1$ and $\Phi_\gamma(x,y) = 1$ are equivalent for all $\lambda, \gamma > 0$.

Now, to define the new ellipticity measure, we start with a Lemma which gives the theoretical foundations for our definition of the new ellipcity measures.

Lemma 3.2.2 *Let a given shape S whose area is 1 and whose centroid coincides with the origin. Let $S(\alpha)$ be the shape S rotated around the origin for an angle α, and let fix $\lambda > 0$. Then:*

(a) $\displaystyle \iint_S \Phi_\lambda(x,y) \; dx \; dy \;=\; \iint_{\mathbf{E}(S)} \Phi_\lambda(x,y) \; dx \; dy \quad \Rightarrow \quad S = \mathbf{E}(S);$

(b) $\displaystyle \min_{\alpha \in (0,2\pi]} \iint_{S(\alpha)} \Phi_\lambda(x,y) \; dx \; dy \;=\; \frac{1}{1+\lambda} \quad \Leftrightarrow \quad S$ *is an ellipse.*

Proof. *(a)* Fix $\lambda > 0$. Since all the points (x, y) satisfying $\Phi_\lambda(x, y) \leq 1$ are inside the ellipse $\mathbf{E}(S)$ (see (3.2.14)) we deduce

$$(x, y) \in \mathbf{E}(S) \quad \text{and} \quad (u, v) \notin \mathbf{E}(S) \quad \Rightarrow \quad \Phi_\lambda(x, y) \leq 1 < \Phi_\lambda(u, v). \tag{3.2.15}$$

Let us assume that the shapes S and $\mathbf{E}(S)$ are different, i.e.

$$\Delta = Area(S \setminus \mathbf{E}(S)) = Area(\mathbf{E}(S) \setminus S) > 0. \tag{3.2.16}$$

The above implication (3.2.15) gives

$$\iint_{S \setminus \mathbf{E}(S)} \Phi_\lambda(x, y) \; dx \; dy \; \geq \; \iint_{\mathbf{E}(S) \setminus S} \Phi_\lambda(x, y) \; dx \; dy \tag{3.2.17}$$

and further

$$\iint_S \Phi_\lambda(x, y) \; dx \; dy \; \geq \; \iint_{\mathbf{E}(S)} \Phi_\lambda(x, y) \; dx \; dy. \tag{3.2.18}$$

Finally, the required implication (in *(a)*) follows from the fact that the equality $\iint_S \phi_\lambda(x, y) dx dy = \iint_{\mathbf{E}(S)} \Phi_\lambda(x, y) dx dy$ holds if and only if

$$\iint_{S \setminus \mathbf{E}(S)} \Phi_\lambda(x, y) \; dx \; dy \; = \; \iint_{\mathbf{E}(S) \setminus S} \Phi_\lambda(x, y) \; dx \; dy \; = \; 0$$

(a direct consequence of (3.2.15) and (3.2.18)) – i.e., if the shapes S and $\mathbf{E}(S)$ are equal.

(b) This item follows from *(a)*, which actually says that $\iint_{S(\alpha)} \Phi_\lambda(x, y) dx dy$ reaches the minimum possible value $\dfrac{1}{1 + \lambda}$ (notice $\dfrac{1}{1 + \lambda} = \iint_{\mathbf{E}(S)} \Phi_\lambda(x, y) dx dy$ and see (3.2.18)) if there is an angle α such that $S(\alpha) = \mathbf{E}(S)$. □

By the arguments of Lemma 3.2.2 we define the following ellipticity measure.

Definition 3.2.2 *Let a given shape S and let $\lambda > 0$. The ellipticity $\mathcal{E}_\lambda(S)$ of S is defined as*

$$\mathcal{E}_\lambda(S) \; = \; \frac{1}{1 + \lambda} \cdot \frac{Area(S)^{1+\lambda}}{\min\limits_{\alpha \in [0, 2\pi]} \iint_{S(\alpha)} \Phi_\lambda(x, y) \; dx \; dy} \tag{3.2.19}$$

where $\Phi_\lambda(x, y)$ is defined as in (3.2.13) and $S(\alpha)$ denotes the shape S rotated around the origin for an angle α.

Now, we summarize desirable properties of $\mathcal{E}(S)$.

Theorem 3.2.2 *All ellipticity measures $\mathcal{E}_\lambda(S)$, $\lambda > 0$, have the following properties:*

(a) $\mathcal{E}_\lambda(S) \in (0, 1]$; *(It tends to 0 for large λ)*

(b) $\mathcal{E}_\lambda(S) = 1$ *if and only if S is an ellipse;*

(c) $\mathcal{E}_\lambda(S)$ *is invariant with respect to translation, rotation and scaling transformations.*

Proof. The proof of *(a)* and *(b)* follows from Theorem 1. $\mathcal{E}_\lambda(S)$ is translation and rotation invariant from the definition. Basic calculus is sufficient to prove the scaling invariance of $\mathcal{E}_\lambda(S)$. $\qquad\square$

Fig.3.2.1 shows how $\mathcal{E}_\lambda(S)$ changes if S is fixed and λ varies. Six shapes and their corresponding graphs $\mathcal{E}_\lambda(S)$ for λ varing through the interval $\in [0.1, 30]$ are displayed.
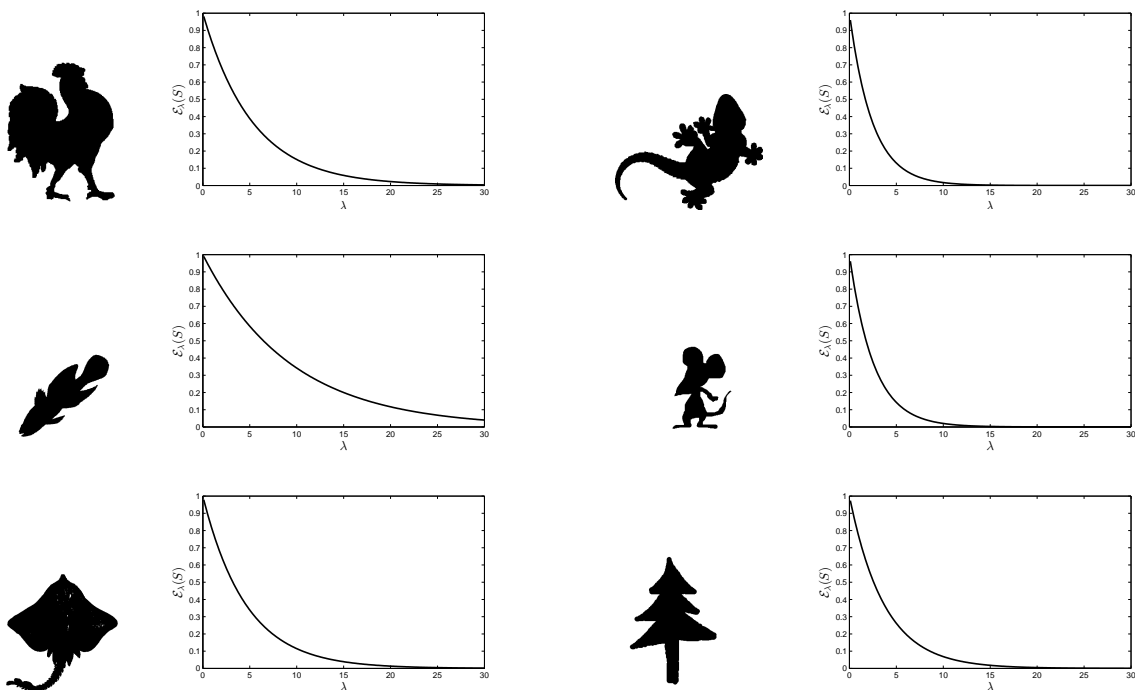
Figure 3.2.1: Six shapes and their corresponding graphs $\mathcal{E}_\lambda(S)$, for $\lambda \in [0.1, 30]$

3.3 Experiments

This section provides several experiments to illustrate the behaviour of the $\mathcal{E}(S)$ ellipticity measure and to compare it with the related measures $\mathcal{E}_f(S)$, $\mathcal{E}_{fm}(S)$, $\mathcal{E}_I(S)$). This section is divided in two parts: Subsection 3.3.1 provides some examples for the basic ellipticity measure given in Definition 3.1. Subsection 3.3.2 presents some experiments to illustrate the behaviour of Sensitivity/Robustness Flexible Ellipticity Measures given in Definition 3.2.

3.3.1 Ellipticity Measure

The first example in this section is noise experiment. Although all measures defined in this chapter are area based and robust with respect to noise or to narrow intrusion, as it has been demonstrated in Fig.3.3.1, the assigned ellipticity measures do not change essentially. The shapes Fig.3.3.1(b),(c),(d), illustrate the noisy images with different level of boundary noise added. Even that the last shape Fig.3.3.1(d) has a big level of noise added, there is no big change on the assigned ellipticity measure.

	(a)	(b)	(c)	(d)
$\mathcal{E}$	0.7484	0.7565	0.7617	0.7466
$\mathcal{E}_f$	0.6701	0.6786	0.6847	0.6668
$\mathcal{E}_{fm}$	0.6821	0.6969	0.7055	0.6929
$\mathcal{E}_I$	0.5622	0.5727	0.5813	0.5580

Figure 3.3.1: Shapes with a different noise level added and their corresponded $\mathcal{E}$, $\mathcal{E}_f$, $\mathcal{E}_{fm}$, and $\mathcal{E}_I$ values.

The second example in this section is a ranking experiment. As shown in Fig.3.3.2, eight random shapes are ranked in accordance with the increasing $\mathcal{E}(S)$ measure. The computed measures $\mathcal{E}(S)$, $\mathcal{E}_f(S)$, $\mathcal{E}_{fm}(S)$, and $\mathcal{E}_I(S)$ are in the table below the shapes. As a result of this experiment, it is possible to say that all measures which is used in this experiment is essentially different because they give different rankings. For example, if we consider the last 6 shapes the obtained rankings are:

$\mathcal{E} : (c)(d)(e)(f)(g)(h);$

$\mathcal{E}_f : (d)(c)(f)(e)(g)(h);$

$\mathcal{E}_{fm} : (c)(d)(f)(e)(g)(h);$

$\mathcal{E}_I : (c)(d)(e)(f)(h)(g)$ – i.e. all the rankings obtained are different.

Shape	(a)	(b)	(c)	(d)	(e)	(f)	(g)	(h)
$\mathcal{E}(S)$	0.1628	0.3011	0.6328	0.7039	0.7676	0.7691	0.9032	0.9033
$\mathcal{E}_f(S)$	0.0000	$----$	0.5324	0.4838	0.6854	0.5326	0.7641	0.7752
$\mathcal{E}_{fm}(S)$	0.0000	0.0000	0.5374	0.6346	0.7426	0.7383	0.7612	0.7801
$\mathcal{E}_I(S)$	0.0266	0.0907	0.4010	0.5026	0.6120	0.6120	0.8305	0.8150
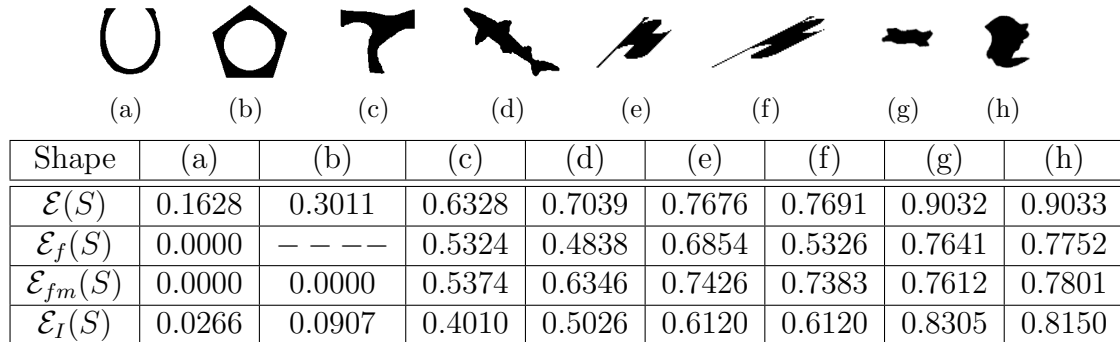
Figure 3.3.2: Shapes are displayed in accordance with their increased $\mathcal{E}(S)$ measure.

Furthermore, the first shape in the same figure (Fig.3.3.2(a)) illustrates a big drawback of $\mathcal{E}_f(S)$ and $\mathcal{E}_{mf}(S)$. Both measures could assign the value 0 to the shapes with big holes or shapes whose centroid lies outside the shape. A consequence is that $\mathcal{E}_f(S)$ and $\mathcal{E}_{mf}(S)$ could not distinguish among such shapes. The new measure $\mathcal{E}(S)$ has no such a drawback and it does not take the value 0 for any shape.

The second shape in the same figure (Fig.3.3.2(b)) illustrates another drawback of the $\mathcal{E}_f(S)$ measure, i.e., it is well-known that $\mathcal{E}_f(S)$ cannot be applied to the N-fold rotationally symmetric shapes (Žunić et al., 2006), because these shapes satisfy $\mu_{1,1}(S) = \mu_{2,0}(S) - \mu_{0,2}(S) = 0$ and, consequently, the orientation angle, defined as in (3.2.5), cannot be computed. The new measure $\mathcal{E}(S)$ does not have such a drawback. Notice that a big hole in the middle of the shape causes $\mathcal{E}_{fm}(S) = 0$ for this shape (as has already been discussed).

Finally, the shapes in Fig.3.3.2(e) and Fig.3.3.2(f) cannot be distinguished by the measure $\mathcal{E}_I(S)$ because it assigns the same value for all the shapes which are produced by affine transformations applied to a shape (as they are shapes in Fig.3.3.2(e) and Fig.3.3.2(f)). The new measure $\mathcal{E}(S)$ distinguishes among these shapes and this

property can be an advantage in some applications. Of course, there are applications where this property is not preferred.

As the third example in this section two shape matching experiments were performed. In these matching experiments our aim is to obtain as many as possible shapes of the same class with the query image because sometimes It can be possible that two shapes from different classes can be similar or vice versa, shapes from the same classes can look like different.

For the first matching experiment (see Fig.3.3.3) we used MPEG7 CE Shape-1 Part-B database. The data set was built by chosing 200 images from 10 different classes (bat, camel, bone, crown, fork, frog, beetle, rat, horseshoe, bird) and we selected "camel-7" as the query image (the enclosed shape in Fig.3.3.3). For the first task we used the first three Hu moment invariants to perform the matching task and we diplayed the best 9 matches in the first row of the Fig.3.3.3). The 3 of the best matches were camels.

In the next four task we chosed a single ellipticity measure form the set $\{\mathcal{E}(S),\ \mathcal{E}_f(S),\ \mathcal{E}_{fm}(S),\ \mathcal{E}_I(S)\}$ and used together with the first three Hu moment invariants. We illsutrated the results of the best 9 matches in the corresponding rows. In all situation there is an improvement. For example, when we used $\mathcal{E}_I(S), \mathcal{E}_f(S)$ or $\mathcal{E}_{fm}(S)$ together with the first three Hu moment invariants, the number of camels inside the 9 best matches increased to 6. But the best improvement has been achieved once the new measure $\mathcal{E}(S)$ has been added to the set of the first three Hu moment invariants. In this case 8 out of 9 best matches were camels.

For the second matching experiment (see Fig.3.3.4), a different data set was created by using different image databases (kimia and mpeg7). For the first task of the second matching experiment, we used only the first three Hu's invariants $(Hu_1(S), Hu_2(S), Hu_3(S))$ to perform shape matching and the best 9 matches (from the database) are listed after the query shape (Fig.3.3.4(a)), after that in Fig.3.3.4(b) we added compactness and elongation $(K(S), El(S))$ to the first three Hu's invariants to increase the classification rate. In Fig.3.3.4(c) our ellipticity method has been added to the listed shape descriptors $(Hu_1(S), Hu_2(S), Hu_3(S), K(S), El(S))$

(a) The first three Hu's moment invariants are used.

(b) $\mathcal{E}(S)$ and the first three Hu's moment invariants are used.

(c) $\mathcal{E}_I(S)$ and the first three Hu's moment invariants are used.

(d) $\mathcal{E}_f(S)$ and the first three Hu's moment invariants are used.

(e) $\mathcal{E}_{fm}(S)$ and the first three Hu's moment invariants are used.

Figure 3.3.3: The enclosed query shape is in the first row. The best nine matches, for a different choice of shape descriptors used, are displayed in the corresponding rows.

and we performed the shape matching again. After we added our ellipticity measure ($\mathcal{E}(S)$), we could say that an improvement is obvious.

Indeed, for the first task in Fig.3.3.4(a) among 9 best matches, there are 3 fishes, what is good, but the best match is not a fish. Moreover, in the second matching task (Fig.3.3.4(b)) although the numbers of matched fishes are increased, the first best match is again not fish. The situation is essentially improved if our ellipticity ($\mathcal{E}(S)$) is added to the descriptors used(see Fig.3.3.4(c)). Among the 9 best matches 7 of them are fishes, and the best 5 matches are fishes.

For the continuation of the second matching experiment we repeat the matching tasks by removing our method and adding other ellipticity measures $\mathcal{E}_I(S), \mathcal{E}_f(S), \mathcal{E}_{fm}(S)$ to illustrate the matching performance of all the methods. For Fig.3.3.4(e) and Fig.3.3.4(f) we repeat the matching task by adding $\mathcal{E}_I(S)$ and $\mathcal{E}_f(S)$ ellipticity methods respectively and it is possible to say that these two methods can select the 5 matches as fishes but the rest of the shapes are from the different classes. Lastly,

in Fig.3.3.4(g), we added $\mathcal{E}_{fm}(S)$ ellipticity method and we determined that our method and $\mathcal{E}_{fm}(S)$ performs similar for this query image and data set.

(a) The first three Hu's moment invariants are used.

(b) The first three Hu's moment invariants, elongation and compactness are used.

(c) $\mathcal{E}(S)$, the first three Hu's moment invariants, elongation and compactness are used.

(d) $\mathcal{E}_I(S)$, the first three Hu's moment invariants, elongation and compactness are used.

(e) $\mathcal{E}_f(S)$, the first three Hu's moment invariants, elongation and compactness are used.

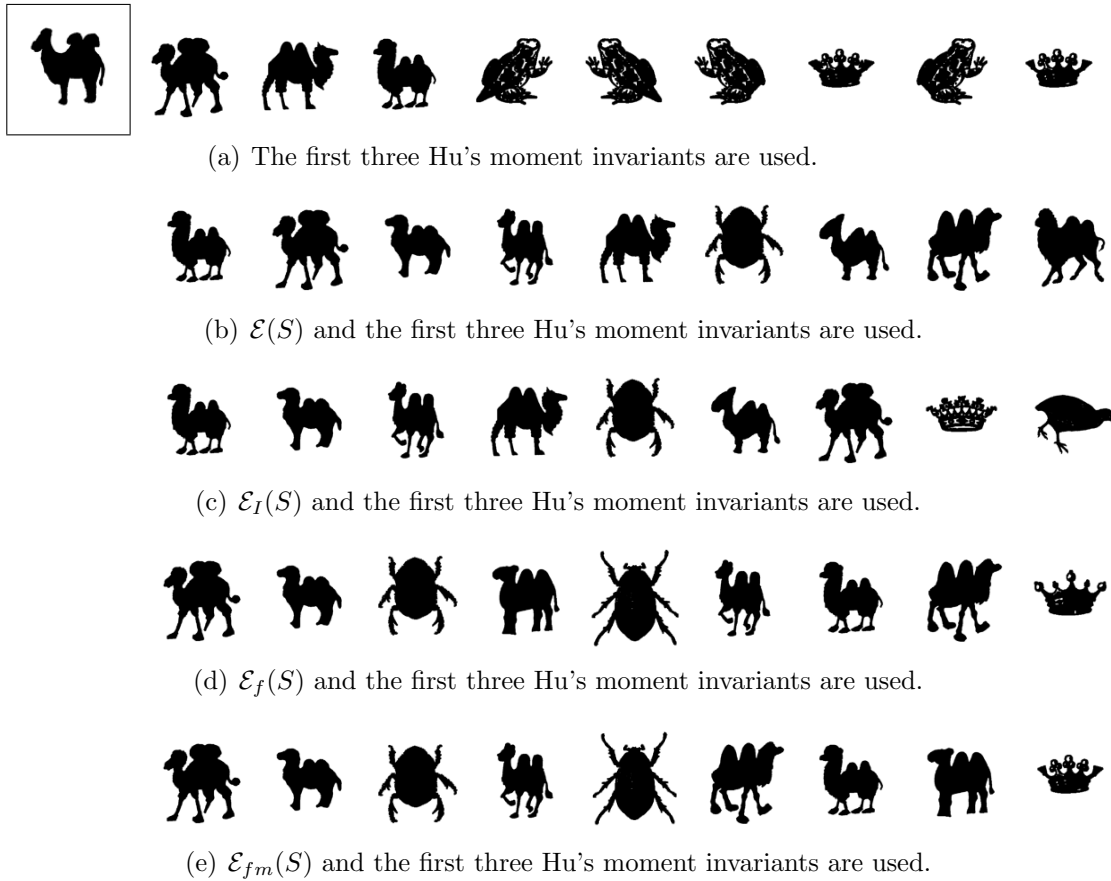(f) $\mathcal{E}_{fm}(S)$, the first three Hu's moment invariants, elongation and compactness are used.

Figure 3.3.4: The enclosed query shape is in the first row. The best nine matches, for a different choice of shape descriptors used, are displayed in the corresponding rows.

In the last example we performed two classification experiments. First one was to classify galaxies in two groups: spiral and elliptical. The data set which are used in this experiment consists of 104 images (100×100 pixels) and is originally used in Lekshmi et al. (2003). The images are thresholded before the classification, as shown in Fig.3.3.5). Four classification tasks were performed, each time by using a single ellipticity measure from the set $\{\mathcal{E}(S),\ \mathcal{E}_f(S),\ \mathcal{E}_{fm}(S),\ \mathcal{E}_I(S)\}$. The classification rates obtained are displayed in the table in Fig.3.3.5. It can be seen that the new ellipticity measure $\mathcal{E}(S)$ (75% classification rate achieved) has performed better than the measures $\mathcal{E}_f(S)$ (65.48%), $\mathcal{E}_{fm}(S)$ (67.31%), and $\mathcal{E}_I(S)$ (63.46%).

For the second part of the classification experiment we create a data set consisting of 150 shapes belonging to 5 classes: butterfly, insect, tool, furniture, vase (taken

	Class. rate
$\mathcal{E}$	75.00%
$\mathcal{E}_f$	65.38%
$\mathcal{E}_{fm}$	67.31%
$\mathcal{E}_I$	63.46%
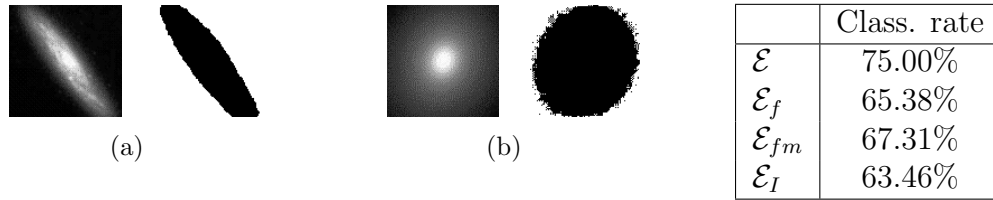
Figure 3.3.5: Sample galaxy images with their shapes extracted by thresholding. The galaxy on the left (a) is spiral and the galaxy in (b) is elliptical.

from the Kimia database). Fig. 3.3.6 shows one sample image from each of these classes. We execute several classification tasks to see the accuracy of our method and how it performs. For each task we combined different set of descriptors such as $\mathbf{Hu}_1$, $\mathbf{Hu}_2$, $\mathbf{Hu}_3$, $\mathbf{El}(S)$, and $\mathbf{E}(S)$ for the classification. We used k-nearest neighbour classifier (kNN), with the value of k arbitrarily set to k = 5. The classification results obtained are in table shown in Fig. 3.3.6. An explanation of the classification results follow.

	Descriptor set	Classification ratio
1.)	$\mathbf{Hu}_1(S)$, $\mathbf{Hu}_2(S)$, $\mathbf{Hu}_3(S)$, $\mathbf{El}(S)$,	66.6667%
2.)	$\mathbf{Hu}_1(S)$, $\mathbf{Hu}_2(S)$, $\mathbf{Hu}_3(S)$, $\mathbf{El}(S)$, $\mathcal{E}(S)$	80.0000%
3.)	$\mathbf{Hu}_1(S)$, $\mathbf{Hu}_2(S)$, $\mathbf{Hu}_3(S)$, $\mathbf{El}(S)$, $\mathcal{E}_f(S)$	73.3333%
4.)	$\mathbf{Hu}_1(S)$, $\mathbf{Hu}_2(S)$, $\mathbf{Hu}_3(S)$, $\mathbf{El}(S)$, $\mathcal{E}_{fm}(S)$	77.3333%
5.)	$\mathbf{Hu}_1(S)$, $\mathbf{Hu}_2(S)$, $\mathbf{Hu}_3(S)$, $\mathbf{El}(S)$, $\mathcal{E}_I(S)$	78.6667%
6.)	$\mathbf{Hu}_2(S)$, $\mathbf{Hu}_3(S)$, $\mathbf{El}(S)$, $\mathcal{E}(S)$, $\mathcal{E}_f(S)$, $\mathcal{E}_{fm}(S)$, $\mathcal{E}_I(S)$	80.0000%'

Figure 3.3.6: Sample shapes from each class used in the classification experiment.

1. In the first classification task, the initial set of descriptors:

$$\mathbf{Hu}_1(S), \mathbf{Hu}_2(S), \mathbf{Hu}_3(S), \mathbf{El}(S) \qquad (3.3.1)$$

were used. The classification rate 66.6667% was obtained.

2. In the next task, $\mathcal{E}(S)$ has been added to the initial set (3.3.1) of shape descriptors. The classification rate has been improved to 80.0000%.

3. In the third classification task , $\mathcal{E}_f(S)$ has been added to the set of initial descriptors (3.3.1) and classification rate has been 73.33%.

4. In the fourth classification task, $\mathcal{E}_{fm}(S)$ has been added to the set of initial descriptors (3.3.1) and classification rate has been 77.3333%.

5. In the fourth classification task, $\mathcal{E}_I(S)$ has been added to the set of initial descriptors (3.3.1) and classification rate has been 78.6667%.

6. Interestingly, in the last task, by adding all ellipticity methods ($\mathcal{E}(S), \mathcal{E}_f(S), \mathcal{E}_{fm}(S), \mathcal{E}_I(S)$) to the initial set of descriptors, the classification rate has not changed it remains 80.0000%.

The second classification experiment has been extended and two more classification experiments have been performed. The same data which is used in the experiment illustrated in 3.3.6 has been normalized by using two different method (Z-score, Min-Max). The results of the experiments for the Z-score normalized data are listed in Fig.3.3.7. For these experiments, our method $\mathcal{E}(S)$ performed best but the classification accuracy of the measure $\mathcal{E}_I(S)$ slightly decreased and performed better than $\mathcal{E}_f(S)$ but performed worst when compared to the other shape descriptors ($\mathcal{E}(S)$, $\mathcal{E}_{fm}(S)$) when Z-score normalization has been used.

	Descriptor set	Class. ratio (Z-Score Norma.)
1.)	$\mathbf{Hu}_1(S)$, $\mathbf{Hu}_2(S)$, $\mathbf{Hu}_3(S)$, $\mathbf{El}(S)$,	66.6667%
2.)	$\mathbf{Hu}_1(S)$, $\mathbf{Hu}_2(S)$, $\mathbf{Hu}_3(S)$, $\mathbf{El}(S)$, $\mathcal{E}(S)$	80.0000%
3.)	$\mathbf{Hu}_1(S)$, $\mathbf{Hu}_2(S)$, $\mathbf{Hu}_3(S)$, $\mathbf{El}(S)$, $\mathcal{E}_f(S)$	73.3333%
4.)	$\mathbf{Hu}_1(S)$, $\mathbf{Hu}_2(S)$, $\mathbf{Hu}_3(S)$, $\mathbf{El}(S)$, $\mathcal{E}_{fm}(S)$	77.3333%
5.)	$\mathbf{Hu}_1(S)$, $\mathbf{Hu}_2(S)$, $\mathbf{Hu}_3(S)$, $\mathbf{El}(S)$, $\mathcal{E}_I(S)$	76.0000%
6.)	$\mathbf{Hu}_2(S)$, $\mathbf{Hu}_3(S)$, $\mathbf{El}(S)$, $\mathcal{E}(S)$, $\mathcal{E}_f(S)$, $\mathcal{E}_{fm}(S)$, $\mathcal{E}_I(S)$	78.6667%'

Figure 3.3.7: Classification experiment and classification results performed by the Z-core normalized data

In Fig.3.3.8 Min-Max normalization has been applied to the same data which is used in experiment Figure 3.3.6. All the measures have been scaled to be between 0 and 1. The same classification were performed and the results are listed in 3.3.8. Still, normalization did not make a big difference to the classifcaiton accuracies. For this experiments our method $\mathcal{E}(S)$ and $\mathcal{E}_I(S)$ performed same and gave the best classification accuracy.

	Descriptor set	Class. ratio (Min-Max Norma.)
1.)	$\mathbf{Hu}_1(S)$, $\mathbf{Hu}_2(S)$, $\mathbf{Hu}_3(S)$, $\mathbf{El}(S)$,	66.6667%
2.)	$\mathbf{Hu}_1(S)$, $\mathbf{Hu}_2(S)$, $\mathbf{Hu}_3(S)$, $\mathbf{El}(S)$, $\mathcal{E}(S)$	78.6667%
3.)	$\mathbf{Hu}_1(S)$, $\mathbf{Hu}_2(S)$, $\mathbf{Hu}_3(S)$, $\mathbf{El}(S)$, $\mathcal{E}_f(S)$	74.6667%
4.)	$\mathbf{Hu}_1(S)$, $\mathbf{Hu}_2(S)$, $\mathbf{Hu}_3(S)$, $\mathbf{El}(S)$, $\mathcal{E}_{fm}(S)$	77.3333%
5.)	$\mathbf{Hu}_1(S)$, $\mathbf{Hu}_2(S)$, $\mathbf{Hu}_3(S)$, $\mathbf{El}(S)$, $\mathcal{E}_I(S)$	78.6667%
6.)	$\mathbf{Hu}_2(S)$, $\mathbf{Hu}_3(S)$, $\mathbf{El}(S)$, $\mathcal{E}(S)$, $\mathcal{E}_f(S)$, $\mathcal{E}_{fm}(S)$, $\mathcal{E}_I(S)$	80.0000%'

Figure 3.3.8: Classification experiment and classification results performed by the Min-Max normalized data.

3.3.2 Sensitivity/Robustness Flexible Ellipticity Measures

This section provides examples which illustrate the behaviour of ellipticty measure $\mathcal{E}_\lambda(S)$ and compare them with the behavior of related measures $\mathcal{E}_f(S)$, $\mathcal{E}_{fm}(S)$, and $\mathcal{E}_I(S)$.

The first example in this section shows how the sensitivity of the ellipcity measures $\mathcal{E}_\lambda$ vary if λ varies. The shapes in Fig.3.3.9(b) is an ellipse with a salt and pepper noise added. As expected, Although all measures ($\mathcal{E}_f$, $\mathcal{E}_{fm}$, and $\mathcal{E}_I$) are area based, They are not assigning much different ellipticity value for this "noise shape" than a perfect ellipse (Fig.3.3.9(a)). As intended, new measures provide a wider interval of ellipcity values, and depending on setted preference it is possible to ignore the presence of noise (e.g. by setting $\lambda = 0.5$) or it is possible to increase the noise sensitivity of the new measures (e.g. by setting $\lambda = 20$ when the ellipticity assigned becomes less than 0.7). Similar comments hold for the next two shapes. Shape in Fig.3.3.9(c) is bounded by a polygonal approximation of an ellipse, and the shape in Fig.3.3.9(d) is an ellipse with a noise added to its boundary.

	(a)	(b)	(c)	(d)
$\mathcal{E}_{\lambda=0.5}$	0.9999	0.9915	0.9971	0.9957
$\mathcal{E}_{\lambda=1}$	0.9998	0.9830	0.9943	0.9914
$\mathcal{E}_{\lambda=1.5}$	0.9997	0.9746	0.9989	0.9619
$\mathcal{E}_{\lambda=4.5}$	0.9992	0.9256	0.9745	0.9619
$\mathcal{E}_{\lambda=10}$	0.9982	0.8422	0.9442	0.9172
$\mathcal{E}_{\lambda=20}$	0.9970	0.6832	0.8915	0.8413
$\mathcal{E}_f$	0.9953	0.9667	0.9449	0.9276
$\mathcal{E}_{fm}$	0.9989	0.9796	0.9462	0.9322
$\mathcal{E}_I$	1.0000	0.9676	0.9922	0.9849
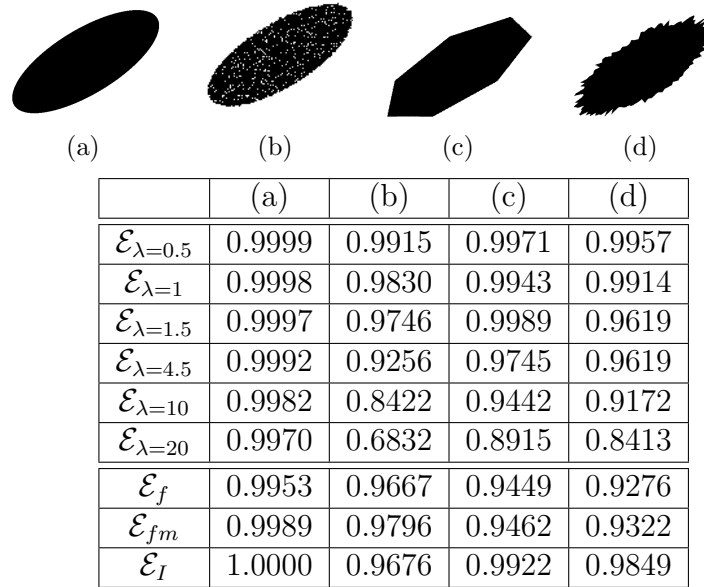
Figure 3.3.9: Shapes similar to a perfect ellipse are is measured with $\mathcal{E}_\lambda$, for $\lambda \in \{0.5, 1, 1.5, 4.5, 10, 20\}$, and with $\mathcal{E}_f$, $\mathcal{E}_{fm}$, and $\mathcal{E}_I$

In the second example in this section ten arbitrary shapes are listed in accordance with the increasing $\mathcal{E}_{\lambda=2}(S)$ measure. The computed measures $\mathcal{E}_{\lambda=2}(S)$, $\mathcal{E}_f(S)$, $\mathcal{E}_{fm}(S)$, and $\mathcal{E}_I(S)$ are in the table below the shapes.

The first part of this second example illustrates that the measures $\mathcal{E}_\lambda(S)$ essentially differs from $\mathcal{E}_f(S)$, $\mathcal{E}_{fm}(S)$, and $\mathcal{E}_I(S)$. Indeed, if we consider the rankings

$\mathcal{E}_{\lambda=2}$: $(b)(c)(d)(e)(f)(g)(h)(i)(j)$;
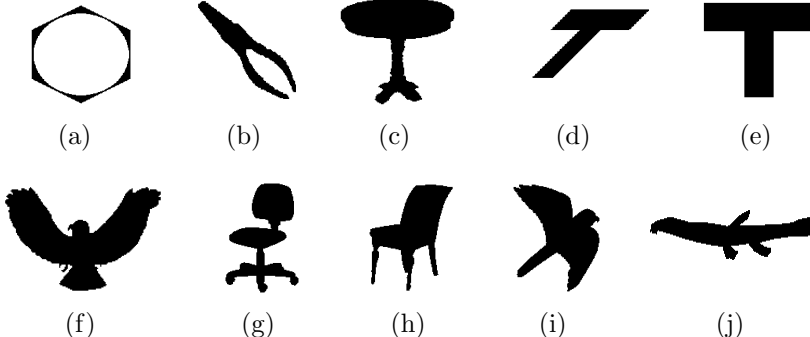
$\mathcal{E}_f$: $(b)(d)(e)(c)(f)(g)(j)(i)(h)$;

$\mathcal{E}_{fm}$: $(b)(d)(e)(c)(f)(g)(j)(h)(i)$;

$\mathcal{E}_I$: $(c)(b)(d)(e)(g)(f)(i)(j)(h)$;

obtained by these 4 measures, we see that the ranking obtained $\mathcal{E}_{\lambda=2}(S)$ differs from the rankings obtained by $\mathcal{E}_f(S)$, $\mathcal{E}_{fm}(S)$, and $\mathcal{E}_I(S)$. Thus, they might be considered as essentially different and can be combined in some classification, matching or recognition tasks.

The second part of this second example illustrates that the new measure can be applied to the shapes which are N-fold rotationally symmetric or which have big holes, without any restriction. As shown in Fig.3.3.10(a), $\mathcal{E}_f(S)$ cannot be applied to rotationally symmetric shapes Žunić et al. (2006)(cannot assign any value) and for

Shape	(a)	(b)	(c)	(d)	(e)	(f)	(g)	(h)	(i)	(j)
$\mathcal{E}_{e=2}(S)$	0.006	0.304	0.306	0.353	0.355	0.366	0.366	0.522	0.522	0.524
$\mathcal{E}_f(S)$	$--$	0.423	0.471	0.464	0.470	0.510	0.517	0.609	0.603	0.583
$\mathcal{E}_{fm}(S)$	0.000	0.432	0.474	0.471	0.472	0.510	0.525	0.612	0.642	0.588
$\mathcal{E}_I(S)$	0.006	0.308	0.305	0.353	0.353	0.365	0.365	0.522	0.520	0.520

Figure 3.3.10: Shapes are displayed in accordance with their increased $\mathcal{E}_{\lambda=2}(S)$ measure.

$\mathcal{E}_{fm}$, this method cannot be applied for shapes with big holes which do not intersects with $SE_f(S)$ (gives the ellipticity value 0).

In the third example in this section two shape matching task was performed. For first experiment of this example the MPEG7 CE Shape-1 Part-B database was used. 140 images were chosen randomly from 7 different classes: chicken, lizzard, lmfish, rat, ray, tree, turtle – for some examples see Fig.3.3.11 . The image "chicken-14" was selected as the query image (the enclosed shape in Fig.3.3.12).

A very good matching result was obtained for a new ellipticity measure and for $\lambda = 2.5$. If $\mathcal{E}_{\lambda=2.5}(S)$ is used for the matching 6 out of 9 best matches were chicken. These shapes are displayed in the first row in Fig.3.3.12. The experiment was repeated by using the measure form the set $\{\mathcal{E}_f(S),\ \mathcal{E}_{fm}(S),\ \mathcal{E}_I(S)\}$ and the best 9 matches are displayed in the corresponding rows.
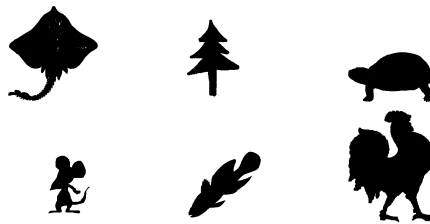
Figure 3.3.11: Example images from each class used in the fist matching task (Fig.3.3.12).

(a) Result of matching task when $\mathcal{E}_{\lambda=2.5}(S)$ is used.

(b) Result of matching task when $\mathcal{E}_f(S)$ is used.

(c) Result of matching task when $\mathcal{E}_{fm}(S)$ is used.

(d) Result of matching task when $\mathcal{E}_I(S)$ is used.

Figure 3.3.12: The enclosed query shape is in the first row. The best nine matches, for a different choice of ellipticity measures used, are displayed in the corresponding rows.
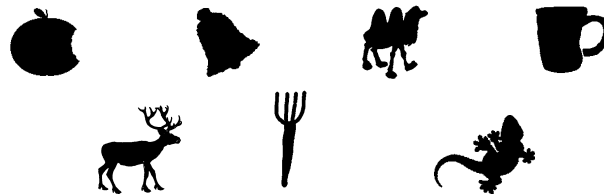
Figure 3.3.13: Example images from each class used in the second matching task (Fig.3.3.14).

In this second experiment another shape matching task was performed. For this experiment same database (MPEG7 CE Shape-1 Part-B) was used. 140 images were chosen from 7 different classes: apple, bell, camel, cup, deer, fork, lizzard – for some examples see Fig.3.3.13 . The image "fork-5" was selected as the query image (the enclosed shape in Fig.3.3.14). In the first row the best 9 matches are displayed if $\mathcal{E}_{e=2}(S)$ are used for the matching (8 of them were forks). In the next three tasks experiment was repeated by using measure form the set $\{\mathcal{E}_f(S), \mathcal{E}_{fm}(S), \mathcal{E}_I(S)\}$ and the best 9 matches are displayed in the corresponding rows. In all matching tasks, the best result has been achieved once the new measure $\mathcal{E}_{e=2}(S)$ has been used. In this case 8 out of 9 best matches were forks.

For the last example in this section a classification task was performed by using

(a) Result of matching task when $\mathcal{E}_{e=2}(S)$ is used.

(b) Result of matching task when $\mathcal{E}_f(S)$ is used.

(c) Result of matching task when $\mathcal{E}_{fm}(S)$ is used.

(d) Result of matching task when $\mathcal{E}_I(S)$ is used.
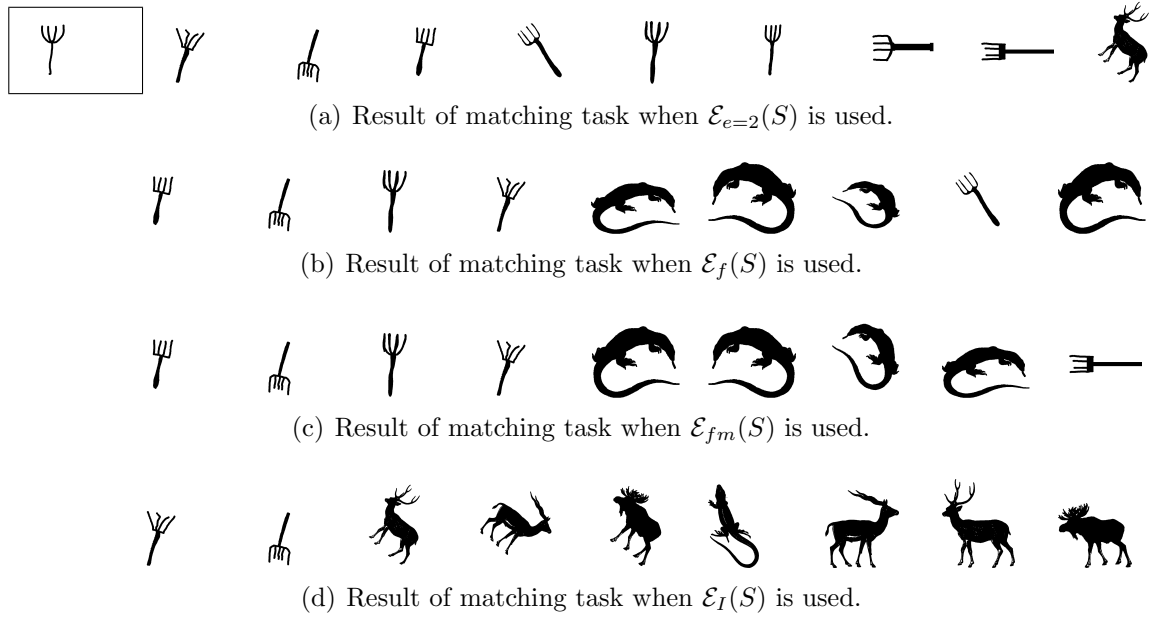
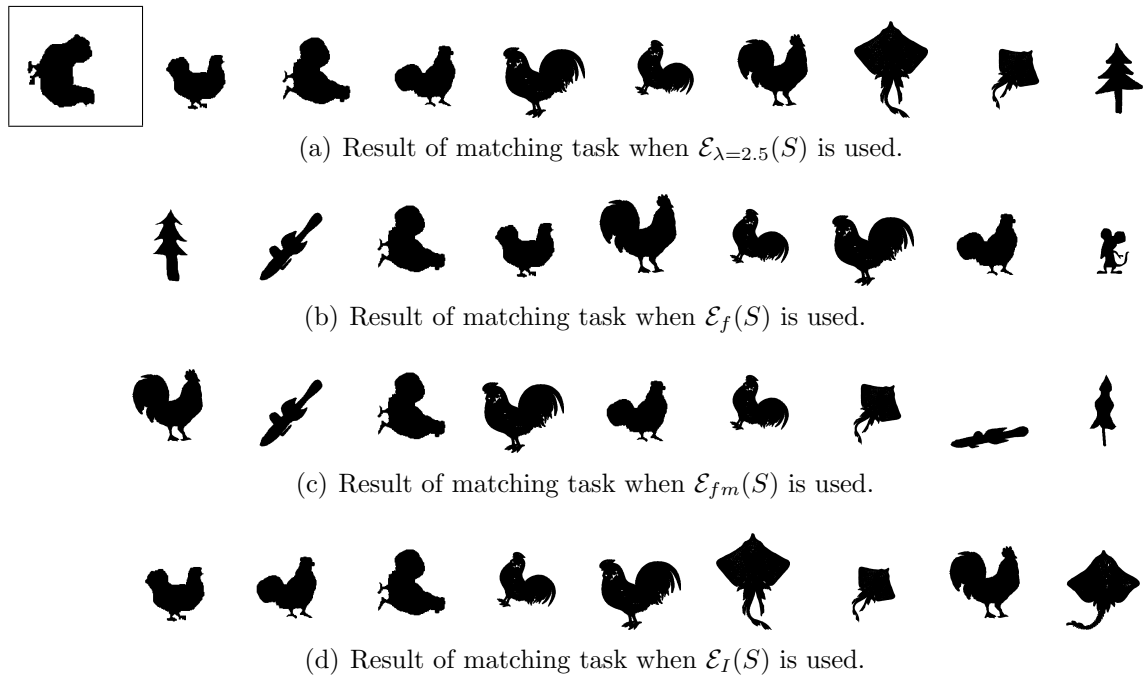Figure 3.3.14: The enclosed query shape is in the first row. The best nine matches, for a different choice of shape descriptors used, are displayed in the corresponding rows.

the well known Lekshmi et al. (2003) data set consists of 112 galaxy images (100 × 100 pixels). There are three group of galaxies: spiral,lenticular and elliptical. To perform the classification task, images converted to binary images (i.e. images are thresholded Otsu (1979) as shown in Fig.3.3.15).

Five classification tasks were performed. For each task we used a single ellipticty measure from the set $\{\mathcal{E}_{\lambda=1}(S), \{\mathcal{E}_{\lambda=5}(S), \mathcal{E}_f(S), \mathcal{E}_{fm}(S), \mathcal{E}_I(S)\}$. We used k-NN classifier, with $k = 5$ and the data set was devided in to two parts and $\approx 30\%$ of galaxy-images, from each classes were used for the training while the remaining images were used for testing. The classification rates obtained are displayed in the table in Fig.3.3.15. It can be seen that the achieved classification rate by using $\mathcal{E}_{\lambda=1}(S)$ (74.22%) is better than the measures $\mathcal{E}_f(S)$ (70.10%), $\mathcal{E}_{fm}(S)$ (69.07%), and $\mathcal{E}_I(S)$ (72.16%).

Finally, since a family of ellipcity measures was obtained, we have used the opportunity to combine several of them to increase the classification accuracy. We have used Forward feature selection method (Whitney, 1971) to find the best features since it is simple and straightforward. An increase of classification accuracy to 78.35% was obtained by using four dimensional feature vectors for the classification. The feature vector components were the following ellipticity measures:

$(\mathcal{E}_{\lambda=1}(S), \mathcal{E}_{\lambda=4}(S), \mathcal{E}_{\lambda=5}(S)$, and $\mathcal{E}_{\lambda=8}(S))$. The same 5-NN classifier and the same split 70%/30% of training/test images were used.

| | (a) | | (b) | | (c) |
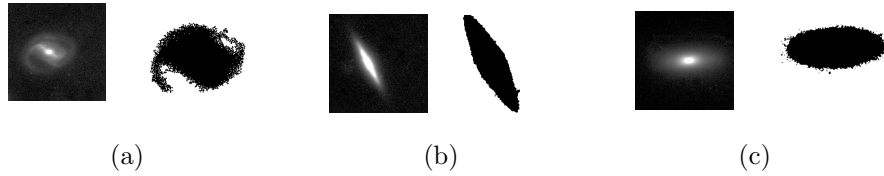
	$\mathcal{E}_{\lambda=1}$	$\mathcal{E}_I$	$\mathcal{E}_{\lambda=5}$	$\mathcal{E}_f$	$\mathcal{E}_{fm}$	$\mathcal{E}_{\lambda=1,4,5,8}$
Class. rate	**74.22%**	72.16%	71.13%	70.10%	69.07%	**78.35%**

Figure 3.3.15: Sample galaxy images with their shapes extracted by thresholding (Otsu, 1979). The galaxy on the left (a) is spiral, the galaxy in (b) is lenticular and the galaxy in (c) is elliptical. The classification rate obtained are in the table.

3.4 Conclusion

Two ellipticity measures are introduced in this chapter. Ellipticity measure $(\mathcal{E}(S))$ is a viable alternative to the existing ellipticity measures $(\mathcal{E}_f(S), \mathcal{E}_{fm}(S), \mathcal{E}_I(S)$, etc.) in the literature. Moreover, sensitive ellipticity measure $(\mathcal{E}_\lambda(S))$ dependent on a single parameter and by varying this parameter the sensitivity/robustness properties of the related ellipticity measures, vary as well. When working on high precision inspection tasks, using a sensitive method can be a desirable property. Apart from these properties, the two ellipticity measures $(\mathcal{E}(S), \mathcal{E}_\lambda(S))$ introduced in this chapter are theoretically well founded and have a clear geometric meaning - they indicate the difference between the considered shape and an ellipse. All the measures defined in this chapter are invariant with respect to translation, rotation and scale transformations, ranges over $(0, 1]$ and gives 1 if and only if the measure shape is an ellipse.

Experiments provided illustrate theoretical observations and demonstrate applicability of the new ellipticity measure. A noise sensitivity of the measure $(\mathcal{E}_\lambda(S))$ is given in 3.3.9. When $\lambda = 1$ selected, the assigned measure for perfect ellipse (Fig.3.3.9(a)) is 0.9998 and measures for noisy images (Fig.3.3.9(b),(c),(d)) are 0.9830, 0.9943, 0.9914 respectively. But the situation is essentially changing when

the parameter selected as $\lambda = 20$. While the assigned ellipticity measure for the perfect ellipse is changing slightly (0.9970), it can be seen that the noisy images that is most affected by lambda changes. The ellipticity measures for Fig.3.3.9(b),(c),(d) when $\lambda = 20$ are $0.6832, 0.8915$ and 0.8413 respectively.

Chapter 4

A family of Ellipticity Measure for galaxy classification

This chapter includes material from:

Mehmet Ali Aktaş, Joviša Žunić. (2013). Family of Shape Ellipticity Measures for Galaxy Classification. *SIAM J. Imaging Sci.*, 6(2):765-781

4.1 Introduction

In recent years, a huge amount of image data is available, and every day, thousands of new visual information is being generated from different domains such as medical science, astronomy and used in many image processing applications including object recognition, classification, image matching, etc. Matching objects by comparing all pairwise features could be computationally expensive and inaccurate. To reduce the computational complexity of matching, it has turned out that another idea is to transform the image data into a set of features (also named features vector), and perform a similarity measure in those feature vectors. To build a feature vector we need the object characteristics which we can quantify into set of numbers easily. The most commonly used features are colour and texture to characterize images. The shape is also one of the object characteristics which enable a spectrum of numerical quantifications. Shape descriptors play a fundamental role in computer vision and pattern recognition, shape analysis, image segmentation, and classification.

This chapter introduces a family of ellipticity measures. As mentioned in section 3.2.1 several ellipticity measures already exist in the literature. All of them use their own way to evaluate how the shape considered differs from an ellipse. These measures assign a highest possible ellipticity to all the ellipses, including circles. Consequently, these measures do not distinguish among ellipses whose axis length ratio differs. Ellipticity measures defined in this chapter distinguish between ellipses whose ratio between the length of the major and minor axis differs.

Every ellipticity measure $\mathcal{E}_\rho(S)$, $\rho > 0$, from the new family, evaluates how much a given shape S differs from an ellipse whose major and minor axis length ratio is ρ. The ellipticity measure ranges over the interval $(0, 1]$ and reaches its maximum value 1 if and only if the measured shape is a perfect ellipse whose major and minor axis ratio is ρ. The measure is invariant with respect to translations, rotations and scaling transformations.

The new family of ellipticity measures are used to perform a galaxy classification task. Classification of galaxies is recognized as a difficult problem (Lekshmi et al., 2003). Several approaches have been introduced and used to perform machine automatic classification. Neural Networks approaches have been used by several experts. The first attempt (in automated galaxy classification) has been done by Odewahn et al. (1992). Another techniques have also been employed. For example Mhnen and Frantti (2000) has developed a galaxy classifier based and fuzzy sets theory. Two types of auto galaxy classifiers are described in Goderya and Lolling (2002). The first model employs geometric shape features and the second model employs direct pixel images for classification purposes. Galaxy classification based on the shape squareness measure has been considered in Rosin and Žunić (2011). The comparison of different galaxy classification algorithms like PCA (Principle Component Analysis), Supervised Neural Networks or quasi-Newton algorithms can be found in Lahav et al. (1996). Fractal Signatures were used in Lekshmi et al. (2003). Shape symmetry analysis, for a quantitative galaxy classification, was considered in Guo et al. (2010).

As mentioned before, in this chapter a galaxy classification task has been per-

formed by using the new family of ellipticity measures. In experiments the elliptical
and spiral galaxies listed in the Nearby Galaxy Catalog (Frei et al., 1996) has been
used, which has been used by many others.

4.2   Family of New Ellipticity Measures

This section introduces a family of new ellipticity measures. As mentioned many
times, an ellipticity measure should provide an indication of how much an ellipse
differs from an arbitrary ellipse (not a specific one). All common approaches in
literature, consider all ellipses as same shapes, and all of them assign the maximum
possible value to all ellipses, including circles. In this chapter we use a different
approach: We assume that ellipses whose axis length ratios differ are different in
shape and, consequently, our request is that the new ellipticity measures must be
able to distinguish among differently elongated ellipses.

   We shortly list the basic terms and denotations that describes some facts about
ellipses.

- $E(a, b)$ denotes an isothetic ellipse whose axis lengths are a and b, and whose
  centroid coincides with the origin. Formally,

$$E(a, b) \;=\; \left\{ (x, y) \mid \frac{x^2}{a^2} + \frac{y^2}{b^2} \leq 1 \right\}.$$

  Just as a short reminder, the area of $E(a, b)$ is $\pi \cdot a \cdot b$.

- Without loss of efficiency in shape classification tasks, prior to the performing
  a classification task, all appearing shapes will be scaled such that they have
  the unit area. So, if an isothetic ellipse $E(\rho)$ has the unit area, if the ratio
  among its axes length is denoted by ρ, and finally, if it is placed such that the
  centroid of $E(\rho)$ coincides with the origin, then $E(\rho)$ can be described as

$$E(\rho) \;=\; \left\{ (x, y) \mid \frac{x^2}{\left(\sqrt{\frac{\rho}{\pi}}\right)^2} + \frac{y^2}{\left(\frac{1}{\sqrt{\pi \cdot \rho}}\right)^2} \leq 1 \right\} = \left\{ (x, y) \mid \frac{x^2}{\rho} + \rho \cdot y^2 \leq \frac{1}{\pi} \right\}.$$

$$\text{(4.2.1)}$$

In other words

$$E(\rho) = E(a, b) \quad \text{with} \quad a = \sqrt{\frac{\rho}{\pi}} \quad \text{and} \quad b = \frac{1}{\sqrt{\pi \cdot \rho}}.$$

- In order to avoid discussions on pathological situations, we will say that two shapes are equal if their set differences have the area equal to zero. This is obviously not a restriction in practical applications – e.g. a closed circle $\{(x, y) \mid x^2 + y^2 \leq 1\}$ and the open one $\{(x, y) \mid x^2 + y^2 < 1\}$ are said to be of the same shape.

- $S(\omega)$ will denote the shape S rotated around its centroid for an angle ω. Notice that the shape centroid, as usually, is defined as $\left(\dfrac{\iint_S x \, dx \, dy}{\iint_S dx \, dy}, \ \dfrac{\iint_S y \, dx \, dy}{\iint_S dx \, dy} \right)$.

Now, we start with a Lemma that gives the arguments for the definition of the family of ellipticity measures.

Lemma 4.2.1 *Let a shape S, whose area is 1 and whose centroid coincides with the origin, be given. Let $S(\omega)$ be the shape S rotated around the origin for an angle ω, and let fix a parameter $\rho > 0$. Then:*

$$\min_{\omega \in (0, 2\pi]} \iint_{S(\omega)} \left(\frac{x^2}{\rho} + \rho \cdot y^2 \right) dx \, dy \ = \ \frac{1}{2 \cdot \pi} \quad \Leftrightarrow \quad S \ = \ E(\rho). \qquad (4.2.2)$$

Proof. We prove the following implication

$$\iint_S \left(\frac{x^2}{\rho} + \rho \cdot y^2 \right) dx \, dy \ = \ \iint_{E(\rho)} \left(\frac{x^2}{\rho} + \rho \cdot y^2 \right) dx \, dy \quad \Rightarrow \quad S = E(\rho)$$
$$(4.2.3)$$

by a contradiction.

So let us assume

- $S \neq E(\rho)$ (or more precisely both $S \setminus E(\rho)$ and $E(\rho) \setminus S$ have a positive area), and

- $\displaystyle \iint_S \left(\frac{x^2}{\rho} + \rho \cdot y^2 \right) dx dy = \iint_{E(\rho)} \left(\frac{x^2}{\rho} + \rho \cdot y^2 \right) dx dy.$

Since the areas of S and $E(\rho)$ are the same (both equal to 1), the areas of $S \setminus E(\rho)$ and $E(\rho) \setminus S$ are also the same (and both strictly positive). Let

$$\Delta \;=\; Area\_of\_(S \setminus E(\rho)) \;=\; Area\_of\_(E(\rho) \setminus S) \;>\; 0.$$

All the points (x, y) satisfying $\dfrac{x^2}{\rho} + \rho \cdot y^2 \leq \dfrac{1}{\pi}$ are inside the ellipse $E(\rho)$ (see (4.2.1)). Thus, we have

$$(x, y) \in E(\rho) \quad \text{and} \quad (u, v) \notin E(\rho) \quad \Rightarrow \quad \frac{x^2}{\rho} + \rho \cdot y^2 \;\leq\; \frac{1}{\pi} \;<\; \frac{u^2}{\rho} + \rho \cdot v^2. \quad (4.2.4)$$

Further, the elementary integral calculus says that there are points $(x_0, y_0) \in E(\rho) \setminus S$ and $(u_0, v_0) \in S \setminus E(\rho)$ such that

$$\iint\limits_{E(\rho)\setminus S} \left(\frac{x^2}{\rho} + \rho \cdot y^2 \right) dxdy \;=\; \left(\frac{x_0^2}{\rho} + \rho \cdot y_0^2 \right) \cdot \Delta \;>\; 0 \qquad (4.2.5)$$

$$\iint\limits_{S\setminus E(\rho)} \left(\frac{x^2}{\rho} + \rho \cdot y^2 \right) dxdy \;=\; \left(\frac{u_0^2}{\rho} + \rho \cdot v_0^2 \right) \cdot \Delta \;>\; 0. \qquad (4.2.6)$$

Quantities in (4.2.5) and (4.2.6) are strictly positive because both Δ and the subintegral function (for all $(x, y) \neq (0, 0)$) are also strictly positive.

Taking into account (4.2.4), (4.2.5), and (4.2.6), we deduce the following strict inequality

$$\iint\limits_{E(\rho)\setminus S} \left(\frac{x^2}{\rho} + \rho \cdot y^2 \right) dxdy \;<\; \iint\limits_{S\setminus E(\rho)} \left(\frac{x^2}{\rho} + \rho \cdot y^2 \right) dxdy. \qquad (4.2.7)$$

Finally, by using the above implication (4.2.7), we derive

$$\iint\limits_{S} \left(\frac{x^2}{\rho} + \rho \cdot y^2 \right) dxdy \;=\; \iint\limits_{S\setminus E(\rho)} \left(\frac{x^2}{\rho} + \rho \cdot y^2 \right) dxdy \;+\; \iint\limits_{S\cap E(\rho)} \left(\frac{x^2}{\rho} + \rho \cdot y^2 \right) dxdy \;>$$

$$\iint\limits_{E(\rho)\setminus S} \left(\frac{x^2}{\rho} + \rho \cdot y^2 \right) dxdy \;+\; \iint\limits_{E(\rho)\cap S} \left(\frac{x^2}{\rho} + \rho \cdot y^2 \right) dxdy = \iint\limits_{E(\rho)} \left(\frac{x^2}{\rho} + \rho \cdot y^2 \right) dxdy \quad (4.2.8)$$

Thus, the above strict inequality contradicts to the assumed: $\iint_S \left(\frac{x^2}{\rho} + \rho \cdot y^2\right) dxdy = \iint_{E(\rho)} \left(\frac{x^2}{\rho} + \rho \cdot y^2\right) dxdy$.

To complete the proof of the theorem it remains to prove that $S = E(\rho)$ implies

$$\min_{\omega \in (0,2\pi]} \iint_{S(\omega)} \left(\frac{x^2}{\rho} + \rho \cdot y^2\right) dx\, dy \;=\; \min_{\omega \in (0,2\pi]} \iint_{E(\rho,\omega)} \left(\frac{x^2}{\rho} + \rho \cdot y^2\right) dx\, dy \;=\; 1/(2\pi),$$

where $E(\rho, \omega)$ is the ellipse $E(\rho)$ rotated around the origin for the angle θ.

Actually, by using the same reasoning as in the first part of the proof of the theorem we can prove:

$$\min_{\omega \in (0,2\pi]} \iint_{E(\rho,\omega)} \left(\frac{x^2}{\rho} + \rho \cdot y^2\right) dx\, dy \;=\; \iint_{E(\rho)} \left(\frac{x^2}{\rho} + \rho \cdot y^2\right) dx\, dy. \qquad (4.2.9)$$

Indeed, for any $\omega \notin \{0, \pi\}$, the strict inequality

$$\iint_{E(\rho,\omega)} \left(\frac{x^2}{\rho} + \rho \cdot y^2\right) dx\, dy \;>\; \iint_{E(\rho)} \left(\frac{x^2}{\rho} + \rho \cdot y^2\right) dx\, dy$$

follows from the facts that $\Delta = Area\_of\_(E(\rho) \setminus E(\rho, \omega)) = Area\_of\_(E(\rho, \omega) \setminus E(\rho)) > 0$ and from the following implication (see (4.2.4) and (4.2.7)):

$$(x,y) \in E(\rho) \setminus E(\rho,\omega) \quad \text{and} \quad (u,v) \notin E(\rho,\omega) \setminus E(\rho) \quad \Rightarrow \quad \frac{x^2}{\rho} + \rho \cdot y^2 \;<\; \frac{u^2}{\rho} + \rho \cdot v^2.$$

Finally, a trivial equality $\dfrac{1}{2 \cdot \pi} = \iint_{E(\rho)} \left(\frac{x^2}{\rho} + \rho \cdot y^2\right) dxdy$, together with the equality (4.2.9), establishes the proof. $\qquad\square$

Motivated by the results of Lemma 4.2.1 we define the following family of ellipticity measures.

Definition 4.2.1 *Let a given shape S whose area is 1 and whose centroid coincides with the origin. Then for every $\rho > 0$, the ellipticity measure $\mathcal{E}_\rho(S)$ of S is defined as*

$$\mathcal{E}_\rho(S) \;=\; \frac{1}{2 \cdot \pi} \cdot \frac{1}{\min\limits_{\omega \in [0,2\pi]} \iint_{S(\omega)} \left(\frac{x^2}{\rho} + \rho \cdot y^2\right) dx\, dy}. \qquad (4.2.10)$$

Now, we summarize desirable properties of the measures from the family $\mathcal{E}_\rho(S)$, $\rho > 0$.

Theorem 4.2.1 *Let a real $\rho > 0$ be given. The ellipticity measure $\mathcal{E}_\rho(S)$ has the following properties:*

(a) $\mathcal{E}_\rho(S) \in (0, 1]$, *for any shape S;*

(b) $\mathcal{E}_\rho(S) = 1$ *if and only if S is isometric to the ellipse $E(\rho)$;*

(c) $\mathcal{E}_\rho(S)$ *is invariant with respect translation, rotation and scaling transformations.*

Proof. The proof of *(a)* and *(b)* follows from Lemma 4.2.1 (i.e. from (4.2.2) and (4.2.8)). The item *(c)* follows directly from the definition. □

Theoretical foundations for the understanding of the behavior of the new ellipticity measures $\mathcal{E}_\rho$ are given above. The behavior of the ellipticity measures, from $\mathcal{E}_\rho(S)$, depends on the choice of the parameter ρ. For a fixed ρ, the measure $\mathcal{E}_\rho(S)$ indicates how much the considered shape S differs from a perfect ellipse $E(\rho)$ whose axes length ratio is ρ. The highest score, equal to 1 is given only to the ellipse $E(\rho)$. For shapes different from $E(\rho)$, including the ellipses whose axes length ratio differs from ρ, the measured $\mathcal{E}_\rho(S)$ ellipticities are strictly less than 1. Selection of the parameter depends on the application which is going to be performed.

An example of two leaf shapes and their measured ellipticities are given in Fig4.2.1 in order to illustrate the behavior of the measure. Their corresponding graphs of $\mathcal{E}_\rho(S)$, when ρ varies through the interval $(0; 1]$, are displayed in the Fig.4.2.2. Thresholded shapes (Fig.4.2.1(a),(b)) extracted from the original leaf images Fig.4.2.1(c),(d). The assigned ellipticity measures for both Fig.4.2.1(a) and Fig.4.2.1(b) from the existing methods $\mathcal{E}_f(S)$, $\mathcal{E}_{fm}(S)$, $\mathcal{E}_I(S)$, $\mathcal{E}(S)$ are not different enough to distinguish these leaf shapes because they are assigning similar ellipticity values for differently elongated ellipses. On the contrary, the situation is essentially different when we used ellipticity measure $\mathcal{E}_\rho(S)$ with the parameter $\rho = 0.85$. The assigned elllipticity measure for Fig.4.1(a) is 0.8215 and for Fig.4.1(b) is 0.5457.
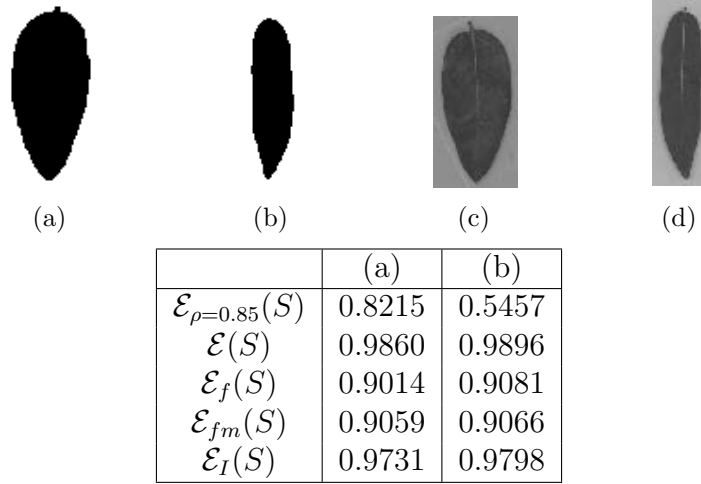
	(a)	(b)
$\mathcal{E}_{\rho=0.85}(S)$	0.8215	0.5457
$\mathcal{E}(S)$	0.9860	0.9896
$\mathcal{E}_f(S)$	0.9014	0.9081
$\mathcal{E}_{fm}(S)$	0.9059	0.9066
$\mathcal{E}_I(S)$	0.9731	0.9798

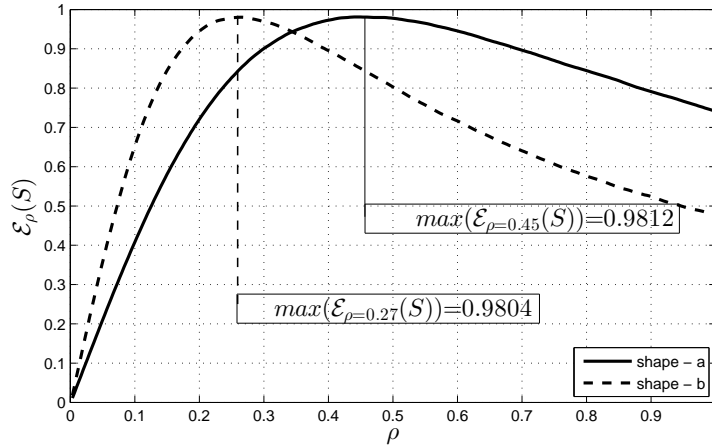Figure 4.2.1: Illustration of the ellipticity measure ($\mathcal{E}_\lambda$(S)) on leaf images.

Figure 4.2.2: Corresponding ellipticity graph of the leaf images (4.2.1). Straight graph belongs to the Fig.4.2.1(a), dotted graph belongs to the 4.2.1(b)

Several more examples of random shapes and their measured ellipticities are given in Fig.4.2.3 in order to illustrate that all the measures from the family $\{\mathcal{E}_\rho(S) \mid \rho \in (0,1]\}$ are independent. Ellipticity measures $\mathcal{E}_{\rho=0.2}$, $\mathcal{E}_{\rho=0.4}$, $\mathcal{E}_{\rho=0.7}$, and $\mathcal{E}_{\rho=0.9}$ from the new family are used to estimate the ellipticity of the shapes displayed and to illustrate that all the measures are indipendent and give different rankings. The obtained results are in accordance with our theoretical considerations. Indeed, for a small value of the parameter ρ, i.e. $\rho = 0.2$ the highest ellipticity $\mathcal{E}_{\rho=0.2}$, is computed for the shape in Fig.4.2.3(c)(i)(h). These shapes, displayed in Fig.4.2.3(c)(i), and the ellipse, displayed in Fig.4.2.3(h), are very elongated and relatively high $\mathcal{E}_{\rho=0.2}$ ellipticities are expected, because the measure $\mathcal{E}_{\rho=0.2}$, actually, estimates how much

a shape differs from an ellipse whose axis length ratio is 0.2 (i.e. the longer axis is 5 times longer than the shorter axis). The situation is opposite for a big ρ. E.g., for $\rho = 0.9$ these shapes have a small $\mathcal{E}_{\rho=0.9}$ ellipticity. $\mathcal{E}_{\rho=0.9}$ measure assigns high values to the shapes in Fig.4.2.3(g)(j)(f) because they can be understood as a very robust shapes (or let say, very circular) as it is an ellipse whose axes lengths are almost the same, i.e. their ratio is 0.9. Notice that the measures $\mathcal{E}_{\rho=0.2}$, $\mathcal{E}_{\rho=0.4}$, $\mathcal{E}_{\rho=0.7}$ $\mathcal{E}_{\rho=0.9}$ all assign different ellipticities for the ellipses in Fig.4.2.3(f)(g)(h), while the ellipticity measure. This is in accordance with our previous discussions. It has been pointed out that the measures from the new family assign different ellipticity values to the ellipses whose axes length ratios differ.

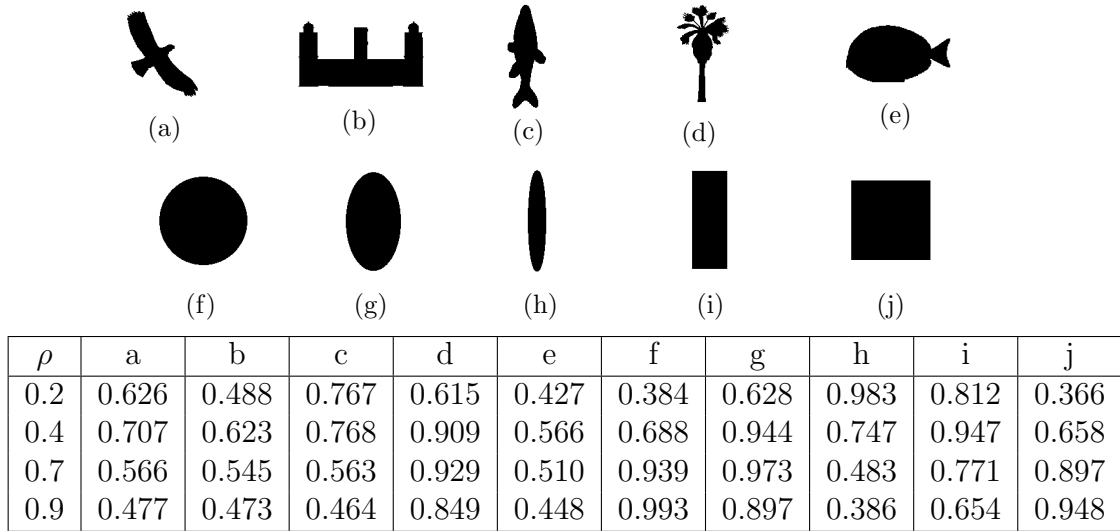| ρ	a	b	c	d	e	f	g	h	i	j
0.2	0.626	0.488	0.767	0.615	0.427	0.384	0.628	0.983	0.812	0.366
0.4	0.707	0.623	0.768	0.909	0.566	0.688	0.944	0.747	0.947	0.658
0.7	0.566	0.545	0.563	0.929	0.510	0.939	0.973	0.483	0.771	0.897
0.9	0.477	0.473	0.464	0.849	0.448	0.993	0.897	0.386	0.654	0.948

Figure 4.2.3: Five random shapes (first row) and five geometric shapes (second row) and their ellipticities $\mathcal{E}_{\rho=0.2}$, $\mathcal{E}_{\rho=0.4}$, $\mathcal{E}_{\rho=0.7}$ and $\mathcal{E}_{\rho=0.9}$, (in the table below the shapes)

optained ranking are:

$\mathcal{E}_{\rho=0.2} : (j), (f), (e), (b), (d), (g), (a), (c), (i), (h),$

$\mathcal{E}_{\rho=0.4} : (e), (b), (j), (f), (a), (h), (c), (d), (g), (i),$

$\mathcal{E}_{\rho=0.7} : (h), (e), (b), (c), (a), (i), (j), (d), (f), (g),$

$\mathcal{E}_{\rho=0.9} : (h), (e), (c), (b), (a), (i), (d), (g), (j), (f),$

The illustrations of the new ellipticity measures on galaxy images are in the next section (Fig.4.3.1-4.3.4) where galaxy classification task is performed. Graphs of $\mathcal{E}_\rho(S)$, when ρ varies through the interval $\left(\dfrac{1}{300}, 1\right)$, for 8 different shapes are in the second row in Fig.4.3.1-4.3.4 (each figures includes two graphs for shapes

obtained by two different thresholding methods, applied to the original gray-level galaxy images). All 4 graphs, of $\mathcal{E}_\rho(S)$, in Fig.4.3.1 and Fig.4.3.2 reach their maxima for the values of the parameter ρ close to 1, and also these maxima are very high for shapes obtained by global thresholding applied to elliptical galaxies displayed in Fig.4.3.1 and Fig.4.3.2. The maximal ellipticity of 0.9923 is obtained for the shape in Fig.4.3.1(b) and the maximal ellipticity of 0.9951 is obtained for the shape in Fig.4.3.2(b)). These high maximas are as expected because the galaxies displayed in these figures are very circular, and consequently, their corresponding thresholding images are nearly circular (notice that $E(\rho = 1)$ is a circle). So, a high ellipticity measures are expected to be reached for a high value of the parameter ρ.

The situation is different for shapes displayed in Fig.4.3.3 and Fig.4.3.4. Thresholded images, corresponding to the original gray-level images, are not circular and the maximum values of $\mathcal{E}_\rho(S)$ are obtained for values of ρ placed close to the middle of the interval $\left(\dfrac{1}{300}, 1\right)$. Also, these maximal ellipticity measures are not close to 1, for the shapes in Fig.4.3.4, since the deviation of these shapes from a perfect ellipse is obvious. But also, a very high maximal ellipticity of 0.9932 is obtained for the shape obtained by global thresholding of the spiral galaxy displayed in Fig.4.3.3(b). A smaller maximal ellipticity of 0.6609 is obtained for the shape Fig.4.3.4(b) which is obtained by the global thresholding from an spiral galaxy displayed in Fig.4.3.4(a).

To mention that using maximal possible ellipticity $(max\{\mathcal{E}_\rho(S)\,|\,\rho \in (0;1]\})$ is not sufficient enough to distinguish among the elliptical and spiral galaxies. Indeed, in both cases (of global and local thresholding) there is an essential overlap for the ranges of $(max\{E(S)\,|\,\rho \in (0;1]\})$ values assigned to elliptical and spiral galaxy shapes:

- for the galaxy shapes obtained by the global thresholding:

  $\mathcal{E}_\rho(S)$ ranges over $[0.9923, 0.9980]$ for the elliptical galaxies, and

  $\mathcal{E}_\rho(S)$ ranges over $[0.6609, 0.9975]$ for the spiral galaxies;

- for the galaxy shapes obtained by the local thresholding:

  $\mathcal{E}_\rho(S)$ ranges over $[0.7775, 0.9809]$ for the elliptical galaxies, and

  $\mathcal{E}_\rho(S)$ ranges over $[0.6888, 0.9419]$ for the spiral galaxies.

Furthermore, an overlap is also exist for the parameters ρ for which $\mathcal{E}_\rho(S)$ reaches the maximum possible value. Thus, it is not possible to determine a definite ρ value which is enough to classify the elliptical and spiral galaxies.

- for the galaxy shapes obtained by the global thresholding:

  ρ ranges over $[0.44, 0.90]$ for the elliptical galaxies, and

  ρ ranges over $[0.18, 0.94]$ for the spiral galaxies;

- for the galaxy shapes obtained by the local thresholding:

  ρ ranges over $[0.41, 0.96]$ for the elliptical galaxies, and

  ρ ranges over $[0.19, 0.99]$ for the spiral galaxies.

4.3 Galaxy Classification by Using Shape Ellipticity Measures

In this section we will describe a classification system/pipeline which we used for galaxy classification. Briefly, the system components are as follows.

– The elliptical and spiral galaxies listed in the *Nearby Galaxy Catalog* (**NGC**) Frei et al. (1996) are used as the data set. The data set consist of 14 elliptical and 90 spiral galax images.

– We used two different thresholding methods to extract galaxy shapes from the original images i.e. two black-white images/shapes will be assigned to each galaxy.

– We create a 6-dimensional feature vectors which assigned to each galaxy shapes by using three ellipticity measures (two of them are from the new family and the third one is from section 3.2.2.

– We used k-NN (k-*Nearest Neighbor*) classifier to perform the classification.

As mentioned, we expect that the ellipticity measures, which distinguish among ellipses whose axis length ratio differs, could be a good choice (at least among shape descriptors), for such a classification, because galaxy shapes could be understood as nearly elliptical (some examples are in Fig.4.3.1-4.3.4). Of course, this does not mean that a classification rate, bigger than targeted 95.1%, will be achieved. There are

another factors which could limit the classification efficiency, like the quality of data used, efficiency and suitability of the thresholding methods applied, performance of classifier selected, etc.
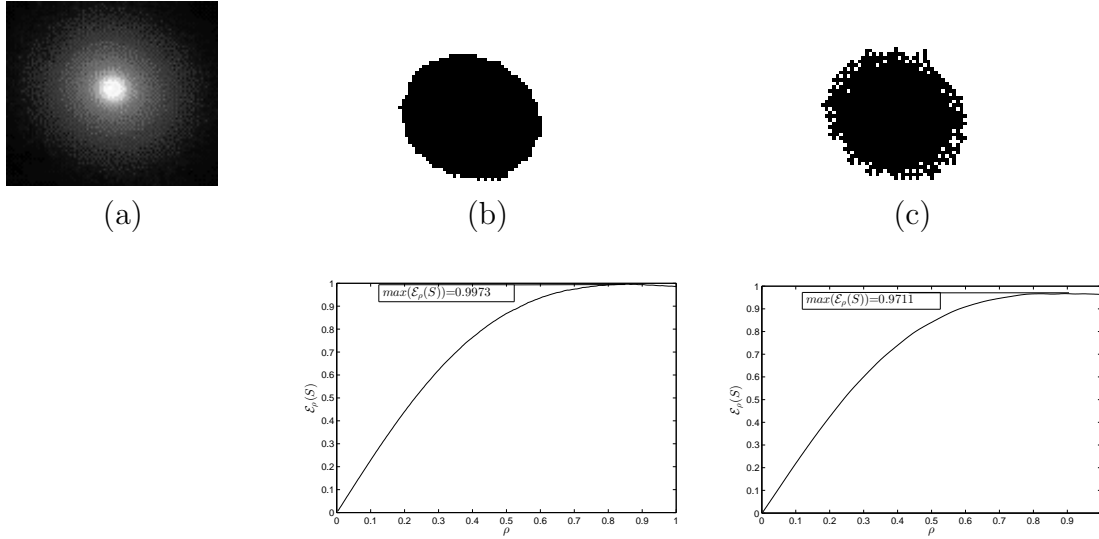

Figure 4.3.1: *First row: (a) Original image,* **NGC** *no.: 3379; (b) Global thresholding applied; (c) Local thresholding applied. Second row: Graphs of $\mathcal{E}_\rho(S)$, $\rho \in (1/300, 1)$ for the shapes in (b) and (c), respectively.*
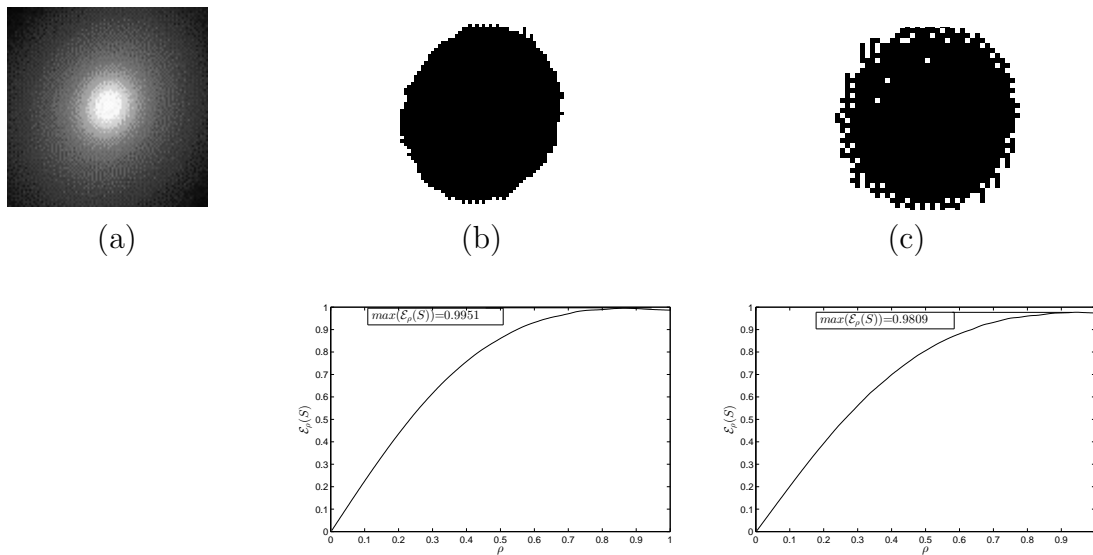
Figure 4.3.2: *First row: (a) Original image,* **NGC** *no.: 4486; (b) Global thresholding applied; (c) Local thresholding applied. Second row: Graphs of $\mathcal{E}_\rho(S)$, $\rho \in (1/300, 1)$ for the shapes in (b) and (c), respectively.*

Figure 4.3.3: *First row: (a) Original image, **NGC** no.: 4258; (b) Global thresholding applied; (c) Local thresholding applied. Second row: Graphs of $\mathcal{E}_\rho(S)$, $\rho \in (1/300, 1)$ for the shapes in (b) and (c), respectively.*

Figure 4.3.4: *First row: (a) Original image, **NGC** no.: 3893; (b) Global thresholding applied; (c) Local thresholding applied. Second row: Graphs of $\mathcal{E}_\rho(S)$, $\rho \in (1/300, 1)$ for the shapes in (b) and (c), respectively.*
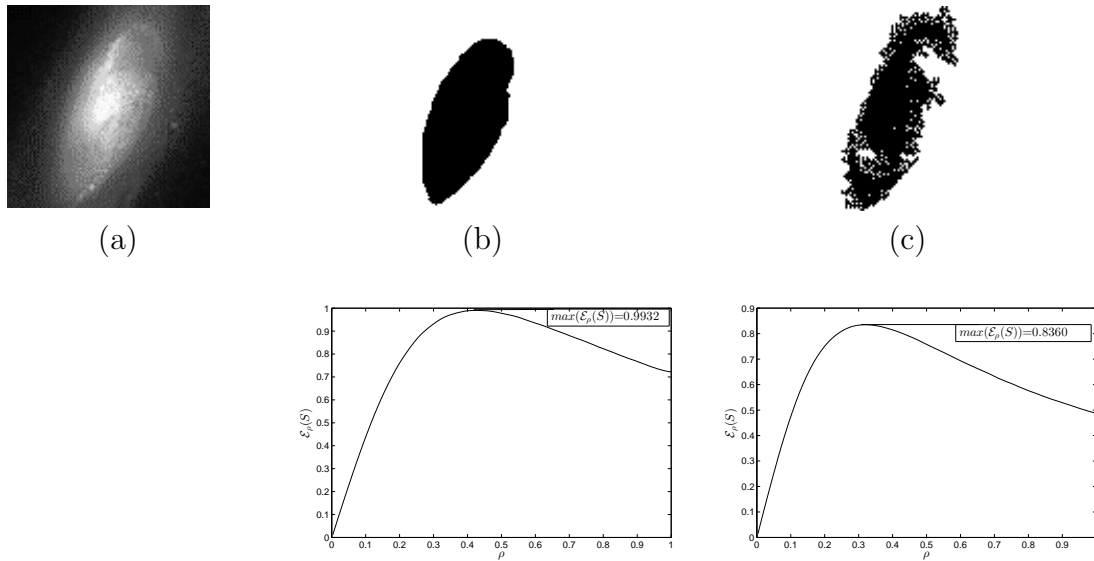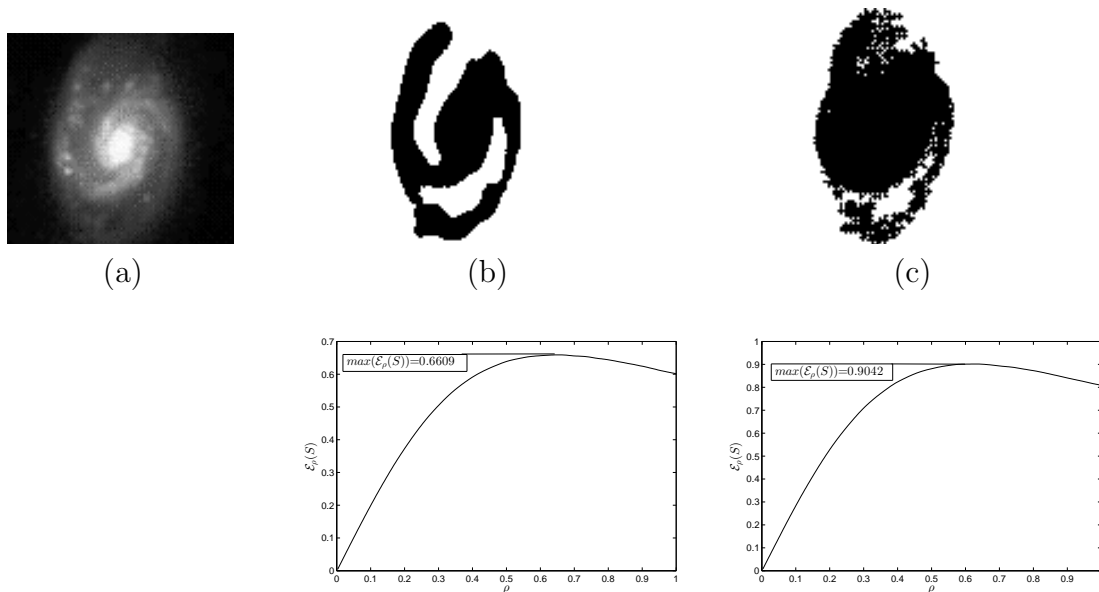
In fixed (or global) thresholding, the threshold value is held constant throughout the image: Determine a single threshold value by treating each pixel independently of its neighborhood.

Since our classification system uses shape based object characteristics we have to extract black and white images (from the original gray-level images) by certain thresholding method. These black-white images actually represent the shape of the galaxies considered. Different thresholding methods and their variants are available in the literature (Sezgin and Sankur, 2004). In this galaxy classification system, we will use two version of Otsu's thresholding method (Otsu, 1979):

First we used a fixed (or global) thresholding, which determines a single threshold value and hold constant throughout the all image pixels. When we use global thresholding, we typically have to play with it, sometimes losing too much of the region and sometimes getting too many extraneous pixels. Thus as a second method we used "local" thresholding which allows the threshold itself to vary across the image (the original method is applied to the blocks of the original images, so the threshold level applied varies). This means that for each original galaxy image we will compute two binary (black and white) images and from these images we will compute components of the feature vectors, which will be used for the classification.

Four examples of original images and pairs of their corresponding thresholded images are in Fig.4.3.1-4.3.4. The galaxies in the images in Fig.4.3.1 and Fig.4.3.2 are elliptical while the galaxies in Fig.4.3.3 and Fig.4.3.4 are spiral. The **NGC** catalog number of these galaxies are: 3379, 4486, 4258, and 3893, respectively.

In all figures (Fig.4.3.1-4.3.4) the image in the first row, on the left, is the original image. The images labeled by (b) are the thresholded image obtained from the original images by using Otsu's method (global thresholding applied), while images labeled by (c) are thresholded images obtained by using local thresholding. In the second rows (in Fig.4.3.1-4.3.4) are the graphs of the ellipticity measure $\mathcal{E}_\rho(S)$, of the corresponding thresholded images S. The parameter ρ ranges from $\rho = 1/300$ to $\rho = 1$ (due to the role of the parameter ρ this is equivalent to the situation where ρ varies through $(1, 300)$).

4.4 Ellipticity Measures Used

As mentioned, two thresholded images, obtained from the original galaxy images, were used for the classification. From both of these images, three ellipticity measures were computed and used for the classification:

- Ellipticity measure $\quad \mathcal{E}_{\rho=0.7}(S) \;=\; \dfrac{1}{2 \cdot \pi} \cdot \dfrac{1}{\min\limits_{\omega \in [0,2\pi]} \iint_{S(\omega)} \left(\frac{x^2}{0.7} + 0.7 \cdot y^2 \right) \; dx \; dy}$

  (**m1**)

  from the new family;

- Ellipticity measure $\quad \mathcal{E}_{\rho=0.9}(S) \;=\; \dfrac{1}{2 \cdot \pi} \cdot \dfrac{1}{\min\limits_{\omega \in [0,2\pi]} \iint_{S(\omega)} \left(\frac{x^2}{0.9} + 0.9 \cdot y^2 \right) \; dx \; dy}$

  (**m2**)

  from the new family;

- Ellipticity measure $\quad \mathcal{E}(S) \;=\; \dfrac{1}{2} \cdot \dfrac{1}{\min\limits_{\omega \in [0,2\pi]} \iint_{S(\omega)} \left(\frac{x^2}{\xi} + \xi \cdot y^2 \right) \; dx \; dy},\qquad$ (**m3**)

  from section 3.2.2 (Eq.3.2.11).

  Note. The parameter ξ is the ratio between the major (3.2.3) and minor axis (3.2.4) as defined in the formula of $\mathcal{E}(S)$, obviously ξ varies and depends on the considered shape S.

Ellipticity measures $\mathcal{E}_{\rho=0.7}(S)$ and $\mathcal{E}_{\rho=0.9}(S)$ were used. Parameters $\rho = 0.7$ and $\rho = 0.9$ were selected by using Forward feature selection (Whitney, 1971). Why the selected parameters $\rho = 0.7$ and $\rho = 0.9$ are performed well, can also be explained by the graphs displayed in Fig.4.4.1. 32 shape were selected randomly and then thresholded by both global and local method. The graphs of $\mathcal{E}_\rho(S)$ for shapes obtained by global thresholding method are in Fig.4.4.1(a), while the graphs $\mathcal{E}_\rho(S)$ for shapes obtained by the local thresholding are in Fig.4.4.1(b). Since for both $\rho = 0.7$ and $\rho = 0.9$ the values of $\mathcal{E}_\rho(S)$ are "scattered" reasonably well, it would enable an efficient discrimination among the galaxy shapes by using the functions/measures $\mathcal{E}_{\rho=0.7}(S)$ and $\mathcal{E}_{\rho=0.9}(S)$. Also, the selected parameters are preferred to be reasonably different.
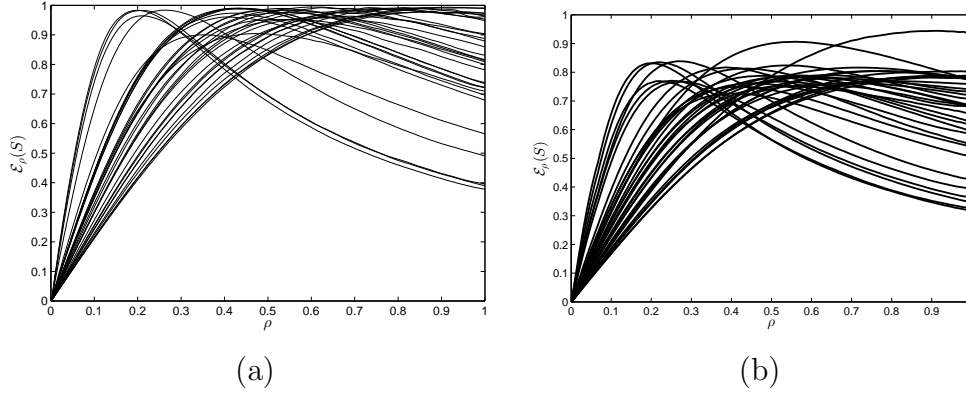
Figure 4.4.1: $\mathcal{E}_\rho(S)$, $\rho \in (1/300, 0)$, *graphs for shapes* S *obtained by thresholding of* 32 *randomly selected galaxy images: (a) global thresholding applied; (b) local thresholding applied.*

For the classification we have used k-Nearest Neighbor Classifier (k-NN), with $k = 5$. Each galaxy was represented by 6 numbers, i.e. the feature vector $FV(\mathbf{g})$ corresponding to a given galaxy $\mathbf{g}$ was

$$FV(\mathbf{g}) \;=\; \big(\mathcal{E}_{\rho=0.7}(S'_{\mathbf{g}}),\; \mathcal{E}_{\rho=0.9}(S'_{\mathbf{g}}),\; \mathcal{E}(S'_{\mathbf{g}}),\; \mathcal{E}_{\rho=0.7}(S''_{\mathbf{g}}),\; \mathcal{E}_{\rho=0.9}(S''_{\mathbf{g}}),\; \mathcal{E}(S''_{\mathbf{g}})\big) \quad (4.4.1)$$

where $S'_{\mathbf{g}}$ and $S''_{\mathbf{g}}$ are binary images obtained from the original image of the galaxy $\mathbf{g}$ thresholded by two selected methods (global and local one).

k-NN, with $k = 5$, is used as the classifier. For the training set we have used 4 elliptical galaxies, and 28 spiral ones (e.g. approximately 30% of galaxies have been used for the training). The classification was performed on the complete data set (galaxies selected for the training were also included).

4.5 Classification Results

The best possible classification accuracy of 100% is achieved, for several choices of training data. So, the existing accuracies are outperformed. In order to get a more robust impression about the efficiency of the classification "mechanism" applied we have performed 100 mutually independent experiments – i.e. galaxies for the training set (4 elliptical and 28 spiral galaxies) have been selected randomly. The average classification rate was 95.6% (still better than both best rates obtained by k-NN and neural network classifiers in Lekshmi et al. (2003)). Among these 100 experiments, the classification rate of 100% was acheived 3 times. The minimal classification rate of 90.2% was obtained 4 times. The classification results are displayed in

Fig.4.5.1. Since the 100% classification accurancy was acheived and since the average classification rate (95.6%) obtained is better than 95.1%, the highest classification rate reported in Lekshmi et al. (2003), we evaluate the established classification mechanism as very efficient.

A detailed classification accuracy tables have been added under the related figures. The tables include the results for the original data and the results for Z-score and Min-Max normalized data. The numbers, which is inside the parenthesis, beside the classification accuracies shows that how many times this classification accuracy achieved. In experiments which are illustrated in Table 4.5.1, 4.5.2, 4.5.3 and 4.5.7 the Z-score slightly imroved the average classification accuracy, but it does not show the same behaviour for the experiments illustrated in Table 4.5.4, 4.5.5 and 4.5.6. The same comments hold for the results of the Min-Max normalization. It improved the average classification accuracy for the experiments which are illustrated in Table 4.5.2, 4.5.3 and 4.5.6, but it decreased the average classification accuracy for the experiments illustrated in Table 4.5.1, 4.5.4, 4.5.5 and 4.5.7.
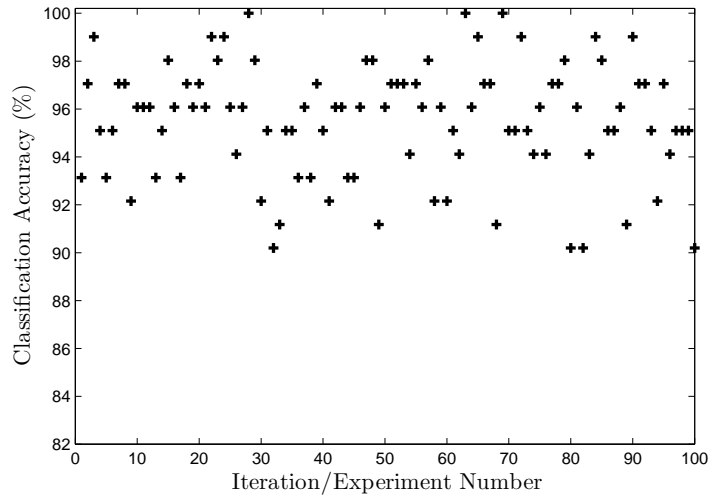
Figure 4.5.1: *Classification rates obtained for* 100 *galaxy classification experiments.*

	minimum	maximum	average
original data	90.2%(4)	100%(3)	95.6%
Z-score normalized data	85.2(2)%	100%(5)	95.7%
Min-Max normalized data	87.2%(4)	98.0%(2)	94.0%

Table 4.5.1: A detailed classification accuracy table for the experiment which is illustrated in Fig.4.5.1. The table includes the minimum, maximum and average classification accuracy results for the original data, Z-score normalized data and Min-Max normalized data.

Even though the method uses two thresholding methods and, actually two shapes assigned to every galaxy image, it can be understood as a very simple one. The new ellipticity measures introduced in this paper, as well as the ellipticity measure from section 3.2.2, are straightforward to compute (from the formulas in (**m1**), (**m2**), and (**m3**)).

As expected, a use of only one of two thresholded images has led to a decrease in the classification accuracy. The classification results obtained were as follows:

- If only black-white images/shapes obtained by the global thresholding method are used, the feature vector $FV(\mathbf{g})$ had to be replaced with a 3-dimensional feature vector $FV_{gt}(\mathbf{g})$ defined as

$$FV_{gt}(\mathbf{g}) \;=\; \left(\mathcal{E}_{\rho=0.7}(S'_{\mathbf{g}}),\; \mathcal{E}_{\rho=0.9}(S'_{\mathbf{g}}),\; \mathcal{E}(S'_{\mathbf{g}}) \right). \tag{4.5.1}$$

  The average classification rate was 87.5%, and the maximum accuracy achieved was 92.1% while the minimal classification rate was 82.4%.

- If only black-white images/shapes obtained by the local thresholding method are used, a 3-dimensional feature vector $FV_{lt}(\mathbf{g})$

$$FV_{lt}(\mathbf{g}) \;=\; \left(\mathcal{E}_{\rho=0.7}(S''_{\mathbf{g}}),\; \mathcal{E}_{\rho=0.9}(S''_{\mathbf{g}}),\; \mathcal{E}(S''_{\mathbf{g}}) \right). \tag{4.5.2}$$

  was assigned to each galaxy $\mathbf{g}$. The average classification accuracy was 92.2%. The maximum accuracy achieved was 96.0% while the minimal classification rate was 84.3%. Because of the 96.0% classification rate achieved (reached in 5 out of 100 experiments), such a simplified version of our method has the efficiency comparable to the methods from Lekshmi et al. (2003).
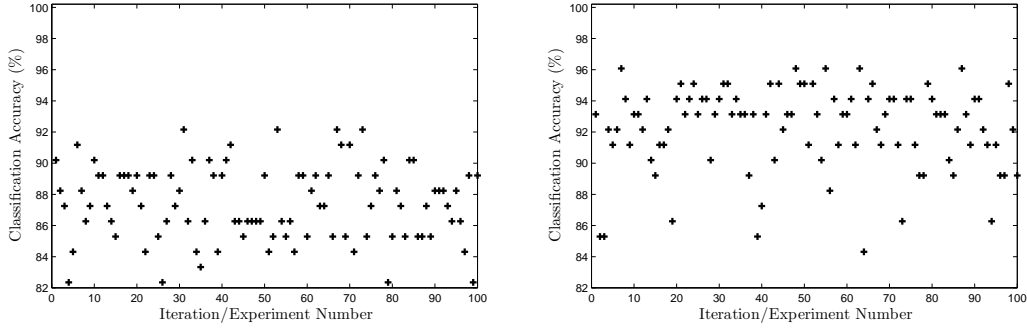
Figure 4.5.2: *Classification rates obtained for* 100 *simplified classification experiments. On the left: the shapes/images obtained by the global thresholding method and the feature vector (4.5.1) used. On the right the shapes/images obtained by the local thresholding method and the feature vector (4.5.2) used.*

	minimum	maximum	average
original data	82.4%	92.1%	87.5%
Z-score normalized data	87.8%	92.1%	89.2%
Min-Max normalized data	87.2%	92.1%	88.6%

Table 4.5.2: A detailed classification accuracy table for the experiment which is illustrated in Fig.4.5.2 (left).

	minimum	maximum	average
original data	84.3%	96.0%	92.2%
Z-score normalized data	85.3%	96.0%	92.5%
Min-Max normalized data	84.3%	96.0%	92.6%

Table 4.5.3: A detailed classification accuracy table for the experiment which is illustrated in Fig.4.5.2 (right).

Several more classification experiment has been done to show that the performance of the mechanism is not limited with the previously selected options (30% traning 100% percent test with $k = 5$). In the second experiment task, approximately 30% of galaxies have been used for the training and 70% have been used for the testing to perform classification. k-NN classifier witk $k = 5$ has been used. The average classification rate was 96.0%. Among these 100 experiments, the classification rate of 100% was acheived 15 times. The minimal classification rate of 88.5% was obtained 4 times. The classification results are displayed in Fig.4.5.3. The classification results which are displayed in Fig.4.5.3 is better than Fig.4.5.1.
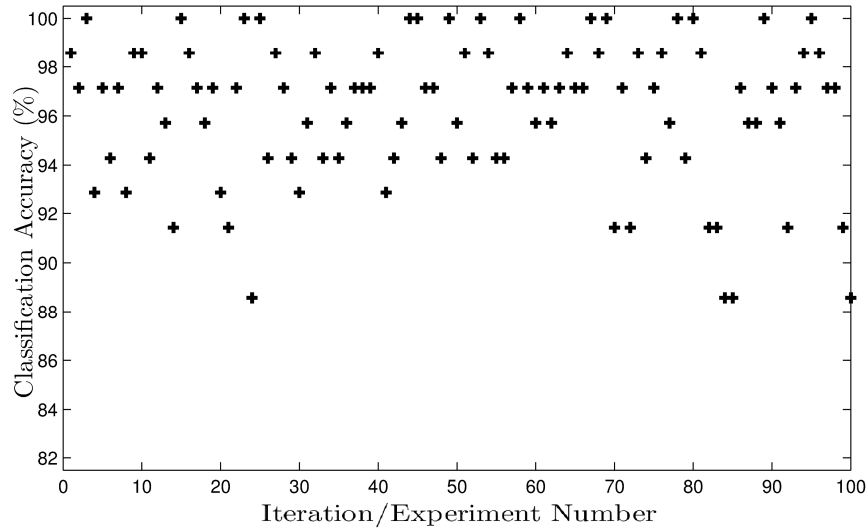
Figure 4.5.3: The experiment has been done by using 30% of the data as training and 70% of the data as testing: Obtained results when $k = 5$: Maximum result that we obtanied is 100% (15 times), Minumum results obtained is 88.5% (4 times) and the average calssification accuracy is 96.0%

	minimum	maximum	average
original data	88.5%(4)	100.0%(15)	96.0%
Z-score normalized data	85.0%(2)	100.0%(14)	95.0%
Min-Max normalized data	81.5%(2)	100.0%(16)	95.3%

Table 4.5.4: A detailed classification accuracy table for the experiment which is illustrated in Fig.4.5.3. The table includes the minimum, maximum and average classification accuracy results for the original data, Z-score normalized data and Min-Max normalized data.

In the next two experiments we repeated classification task by using 70% of the galaxies as training and 30% of the galaxies as testing. The classification results are displayed in Fig.4.5.4 and Fig.4.5.5. k-NN classifier witk $k = 5$ (Fig.4.5.4) and $k = 6$ (Fig.4.5.5) has been used. The average classification rate was 96.6% when $k = 5$ is used. The classification rate of 100% was acheived 29 times. The minimal classification rate of 90.3% was obtained 6 times. The classification performance improved when $k = 6$ is used. The average classification rate was 97.1%, the classification rate of 100% was acheived 39 times and the minimal classification rate of 90.3% was obtained 2 times.
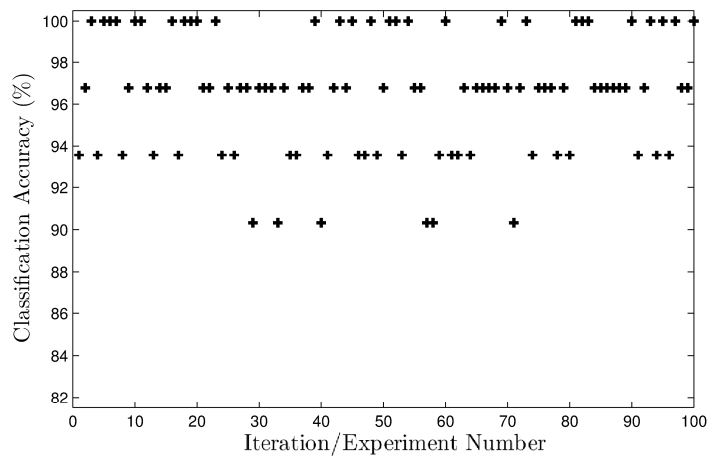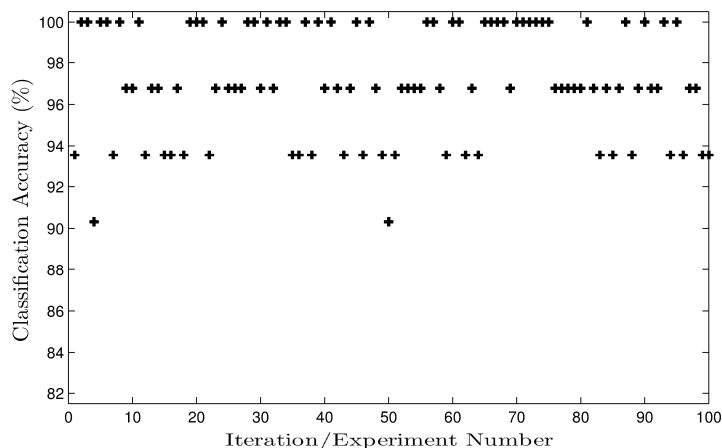
Figure 4.5.4: The experiment has been done by using 70% of the data as training and 30% of
the data as testing: Obtained results when $k = 5$: Maximum result that we obtained is 100% (29
times), Minumum results obtained is 90.3% (6 times) and the average classification accuracy is
96.6%.

	minimum	maximum	average
original data	90.3%(6)	100.0%(29)	96.6%
Z-score normalized data	84.3%(2)	100.0%(29)	96.1%
Min-Max normalized data	87.1%(3)	100.0%(31)	96.3%

Table 4.5.5: A detailed classification accuracy table for the experiment which is illustrated in
Fig.4.5.4. The table includes the minimum, maximum and average classification accuracy results
for the original data, Z-score normalized data and Min-Max normalized data.

Figure 4.5.5: The experiment has been done by using 70% of the data as training and 30% of
the data as testing: Obtained results when $k = 6$: Maximum result that we obtained is 100% (39
times), Minumum results obtained is 90.3% (2 times) and the average classification accuracy is
97.1%.

	minimum	maximum	average
original data	90.3%(2)	100.0%(39)	97.1%
Z-score normalized data	83.9%(4)	100.0%(40)	96.8%
Min-Max normalized data	87.8%(1)	100.0%(45)	97.3%

Table 4.5.6: A detailed classification accuracy table for the experiment which is illustrated in Fig.4.5.5. The table includes the minimum, maximum and average classification accuracy results for the original data, Z-score normalized data and Min-Max normalized data.

Lastly, we performed another classification task to show that the result of the classiffcation results vary depending on the choice of the values of the parameter ρ. In Fig.4.5.6, we give the classification accuracy for $\rho = 0.4$ and $\rho = 0.5$ selected. Both highest and average accuracies were lower.
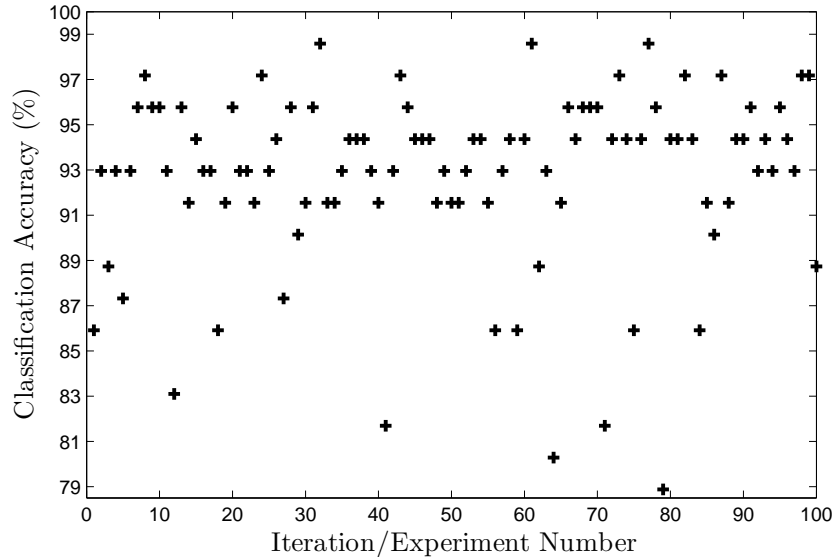
Figure 4.5.6: The experiment has been done by using 30% of the data as training and 100% of the data as testing with $\rho = 0.4$ and $\rho = 0.5$: Obtained results when $k = 5$: Maximum result that we obtained is 98.6% (3 times), Minimum classification obtained is 78.8% (1 times) and the average classification accuracy is 92.7%

	minimum	maximum	average
original data	78.8%(1)	98.6%(3)	92.7%
Z-score normalized data	79.7%(3)	98.6%(5)	93.8%
Min-Max normalized data	82.3%(2)	96.3%(2)	92.4%

Table 4.5.7: A detailed classification accuracy table for the experiment which is illustrated in Fig.4.5.6. The table includes the minimum, maximum and average classification accuracy results for the original data, Z-score normalized data and Min-Max normalized data.

4.6 Experiments on a common dataset

The two experiments, a matching experiment and a classification experiment were performed to compare the method with the other ellipticity measures which are considered in the thesis and to show the behaviour of the method on a common dataset. For the matching experiment "MPEG7 CE Shape-1 Part-B" database has been used. The data set was built by choosing 120 images from 5 classes (chicken, fly, bone, apple, horseshoe, tree) and "chicken-12" has been selected as a query image (the enclosed shape in Fig.4.6.1). In each task a single ellipticity measure has been chosed form the set $\{\mathcal{E}(S), \mathcal{E}_f(S), \mathcal{E}_{fm}(S), \mathcal{E}_I(S)\}$ and the results of the best 9 matches were illsutrated in the corresponding rows.

In the first and the second row the best 9 matches are displayed if $\mathcal{E}_f(S)$ and $\mathcal{E}_{fm}(S)$ are used respectively for the matching (5 of them were chickens). For the third task $\mathcal{E}_I(S)$ measure was used and the matching experiment was repeated. $\mathcal{E}_I(S)$ ellipticity measure performed better than either the $\mathcal{E}_f(S)$ measure or $\mathcal{E}_{fm}(S)$ measure and selected 6 of the best matches as chicken.

Moreover, in row four, the same matching experiment was performed by using the ellipticity measure $\mathcal{E}(S)$ which is defined in section 3.2.2. The results show that both ellipticity measures $\mathcal{E}(S)$ and $\mathcal{E}_I$ performed conformable. Furthermore, $\mathcal{E}(S)$ selected first two shapes from the same class and $\mathcal{E}_I(S)$ selected only the first image from the same class. Thus, we can say that $\mathcal{E}(S)$ measure performed slightly better than $\mathcal{E}_I(S)$. For the fifth task $\mathcal{E}_{\alpha=2}(S)$ measure which is defined in section 3.2.2 was used and for this situation, it performs worst than $\mathcal{E}_I(S)$ and $\mathcal{E}(S)$ measure (5 of them were chickens). For the next two tasks, the measure $\mathcal{E}_\rho(S)$ was used with different ρ. In row six the measure $\mathcal{E}_\rho(S)$ with $\rho = 8$ was used for the matching and 7 of them were chicken. For the last task two measures from the $\mathcal{E}_\rho(S)$ family were used. When the measures $\mathcal{E}_{\rho=7}(S)$ and $\mathcal{E}_{\rho=9}(S)$ were used together, there was only one shape which is selected from the different class. Thus, the best result has been achieved once the measures $\mathcal{E}_{\rho=7}(S)$ and $\mathcal{E}_{\rho=9}(S)$ have been used. In this case 8 out of 9 best matches were chicken.

(a) Result of matching task when $\mathcal{E}_f(S)$ is used.

(b) Result of matching task when $\mathcal{E}_{fm}(S)$ is used.

(c) Result of matching task when $\mathcal{E}_I(S)$ is used.

(d) Result of matching task when $\mathcal{E}(S)$ is used.

(e) Result of matching task when $\mathcal{E}_{\alpha=2}(S)$ is used.

(f) Result of matching task when $\mathcal{E}_{\rho=8}(S)$ is used.

(g) Result of matching task when $\mathcal{E}_{\rho=7}(S)$ and $\mathcal{E}_{\rho=9}(S)$ are used together.
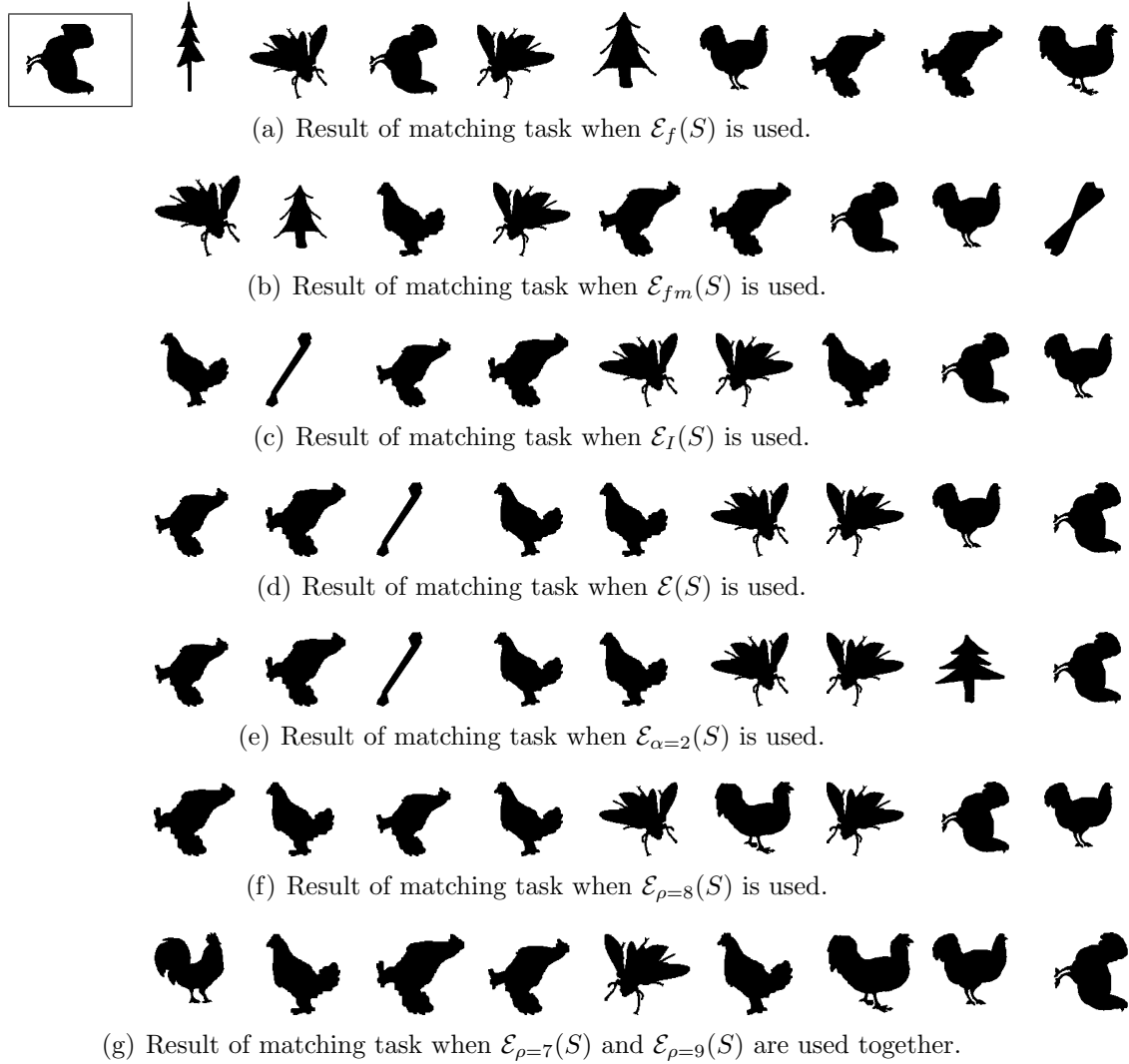
Figure 4.6.1: The enclosed query shape is in the first row. The best nine matches, for a different choice of shape descriptors used, are displayed in the corresponding rows.

For the classification experiment we created a data set consisting of 150 shapes belonging to 5 classes: starbust, ancient weapon, bug, butterfly, fish (taken from the Kimia database). The shapes selected randomly. Fig.4.6.2 shows one sample image from each of these classes. We used k-nearest neighbour classifier (kNN), with the value of k arbitrarily set to $k = 5$. The classification results obtained are in table shown in Fig.4.6.2.

The classification rates obtained are displayed in the table in Fig.4.6.2. It can be seen that the achieved classification rate by using the basic ellipticity measure defined in section 3.2.2. $\mathcal{E}(S)$ (60.00%) is better than the measures $\mathcal{E}_f(S)$ (56.00%), $\mathcal{E}_{fm}(S)$ (44.00%), and $\mathcal{E}_I(S)$ (57.33%). When the classification performed by using $\mathcal{E}_{\alpha=3}(S)$ measure, the classifcation accuracy was 63.00% and combining two

measures($\mathcal{E}_{\alpha=3}(S)$, $\mathcal{E}_{\alpha=7}(S)$) from the same family did not improve the result.

The most satisfactory classification accuracy was achieved when $\mathcal{E}_{\rho=0.9}(S)$ measure has been used to perform the classification, the classification accuracy increased to 73.33% which is better than all other results when a single descriptor is used. But the highest classification accuracy was achieved when two measures ($\mathcal{E}_{\rho=0.7}(S)$, $\mathcal{E}_{\rho=0.9}(S)$) from the family have been used together, the obtained classifcation accuracy was 96.00%.

To summarize: the results show that the family of ellipticity measure $\mathcal{E}_\rho(S)$ performed better for both of the experiments. The performance of the method depends on the ρ and when the optimum ρ selected, high results can be achieved.

	Descriptor set	Classification ratio
1.)	$\mathcal{E}_f$	56.00%
2.)	$\mathcal{E}_{fm}$	44.00%
3.)	$\mathcal{E}_I$	57.33%
4.)	$\mathcal{E}(S)$	60.00%
5.)	$\mathcal{E}_{\alpha=3}(S)$	63.00%
5.)	$\mathcal{E}_{\alpha=3}(S), \mathcal{E}_{\alpha=7}(S)$	63.00%
6.)	$\mathcal{E}_{\rho=0.9}(S)$	73.33%
7.)	$\mathcal{E}_{\rho=0.7}(S), \mathcal{E}_{\rho=0.9}(S)$	96.00%

Figure 4.6.2: Sample shapes from each class used in the classification experiment.

4.7 Conclusion

In this section we have considered a galaxy classification problem. We have used a well known galaxy images from the Nearby Galaxy Catalog (Frei et al., 1996) (14 elliptical and 90 are spiral ones). Several approaches are already applied to solve the problems and different classification rate were obtained. A classification rates of 92.3% and 95.1% were reported in Lekshmi et al. (2003) (a fractal signature and nearest neighbor and neural network classifiers were used). Here, we have used shape based approach. Shape characteristics are very often used for shape characterization

particularly because they allow many numerical characterization. Here we decided to use shape ellipticity descriptors, for such numerical characterizations. Such a choice seems to be natural since the galaxy shapes can be understood as nearly elliptical. Also, because ellipticity measures are global descriptors – i.e. just a single number is assigned to any object (i.e. its corresponding shape) we knew that a single descriptor would not be enough to overcome the existing classification accuracies (mentioned above). Because of that, we develop a family of the new ellipticity measures. Knowing that these measure need to distinguish among shapes which are very often nearly elliptical, we assume that a combination of the existing ellipticity measures, which do not distinguish among differently elongated ellipses, very likely would not lead to a high classification accuracy. The ellipticity measures from the new family, contrary to the existing ellipticity measures, distinguish among differently elongated ellipses (e.g. among ellipses whose axis length ratio differs).

Another issue is that we had to select a thresholding method which has to be used to get the galaxy shape (represented by a black and white image) from the original galaxy images. Obviously, any threshold method selected would bring some limitations incorporated into the cumulative efficiency shown at the end of the classification process. To reduce such a limit, we decided to use two thresholded images for each galaxy. These two images are obtained by using both, "global" and "local" version of the Otsu thresholding method (Otsu, 1979; Sezgin and Sankur, 2004).

Finally, we have selected k-NN classifier. We have assigned a 6 dimensional feature vector to each galaxy. Precisely, components of the feature vectors were computed by using only two ellipticity measures $\mathcal{E}_{\rho=0.7}(S)$ and $\mathcal{E}_{\rho=0.9}(S)$ from the new family, and an ellipticity measure which is defined in section 3.2.2. These three ellipticity measures were used to obtain 3 numbers for each of two corresponding threshold images (i.e. 6 numbers in total).

Even that we have used a relatively simple classification procedure we have reached the maximum possible 100% classification rate. Approximately 30% of galaxies were used as a training set and classification has been performed on the whole data set, including galaxies from the training set. The selection of the train-

ing set has been done randomly. Since there is always a bias of the training data used, to the classification efficiency obtained, we have repeated the classification task 100 times. This is in order to get a better evaluation of the efficiency of the classification process selected. The average classification rate was very high – 95.6% (3 out of 100 experiments had the 100% accurancy) and still beter than the results from Lekshmi et al. (2003).

Chapter 5

Conclusion

The aim of the research presented in this thesis was to create new shape descriptors and showing their suitability for image processing applications. All the shape descriptors are not applicable for all kind of applications and it is important to select optimum descriptors for specific application. The shape descriptors which is defined in this thesis is also not universal, but can be used as an additional tool which can be implemented to meet the specific applications needs.

The experiments in this thesis were designed to illustrate the use of these descriptors. More reasonable visual applications would be more complicated and needs to combinations of several shape descriptors to achieve specific task such as galaxy classification which was performed in last section.

Since each chapter has its own conclusion, we conclude this thesis with a summary, and with possibilities for future work.

5.1   Thesis summary and future work

The following section outlines the basic structure of this thesis, highlighting the main points of interest in each of the previous chapters. Some suggestions for further work are also given.

Chapter 1 gives a general introduction to shape descriptors and applications. Some well-known descriptors from the literature are presented in this chapter. Figure 1.2 gives the basic structure of image processing applications; this basic structure is

considered on the experiments in the rest of the chapters.

The Centeredness measure was introduced in Chapter 2. The new measure considers the distance between the shape centroid computed from the shape interior points and the shape centroid computed from the shape boundary points. In the experiments section the measure has performed well and resulted in improved accuracy in shape matching and shape classification tasks once the new descriptor is added to a set of other shape descriptors.

A line of future research is to follow the same approach, creating a shape signature and consider the Fourier Descriptors. In the literature the triangular area between two boundary points and the area based centroid has been studied. It can be possible to define a new shape signature which this time considers the area between two centroids (area based and contour based) and a boundary point. Moreover, it is also possible to use the angle between the two lines (first line is from boundary point to area based centroid and the second line is from the same boundary point to the contour based centroid.) It is also possible to try further extensions.

In Chapter 3 two ellipticity methods are defined and compared with existing ellipticity measures. The first presented ellipticity measure provides a reasonable alternative to the existing methods found in the literature. The second ellipticity measure which is described in the same chapter is the modified of the initially defined ellipticity measure. The second measure is dependent on a single parameter and by varying this parameter the sensitivity/robustness properties of the related ellipticity measures, vary as well. In some situations methods which sensitive to the presence of noise or to small object deformations, are more preferred. (e.g. in high precision inspection tasks.). These measures overcome some of the shortcomings of the existing methods. $\mathcal{E}$ and $\mathcal{E}_\lambda(S)$ can be applied to the shapes which are N-fold rotationally symmetric or which have big holes, without any restriction.

Finally Chapter 4 introduces a family of ellipticity measure. Ellipticity measures defined in this chapter distinguish between ellipses whose ratio between the length of the major and minor axis differs. All the existing methods assign a highest possible ellipticity to all the ellipses, including circles. This can be a disadvantage.

For example, some leaf shapes or mirrors are nearly elliptic, and to be able to distinguish among such elliptic shapes it is suitable to have ellipticity measures which treat differently ellipses which have a different major and minor axis ratio. It was illustrated in Fig.4.2.1.

In the experiment section a ranking task and galaxy classification task performed. The ranking experiments showed that all the ellipticity measures from the family are independent and can be used alone. And galaxy classification experiment showed that the defined family of ellipticity measures perform well.

Another possible line of research is to divide a given shape based on their gray levels and apply the specific shape descriptors to these individual components (Multi Component Analaysis). A gray levels in the image will be in the range $0 - -255$, with zero being black and 255 being white. These shapes can be segmented based on different ranges of gray level then each segment can be analayzed and computed seperately and a single measure is going to be assigned from the considered shape descriptor. (See Fig.5.1 for the illustration of the segmentation based on different levels)

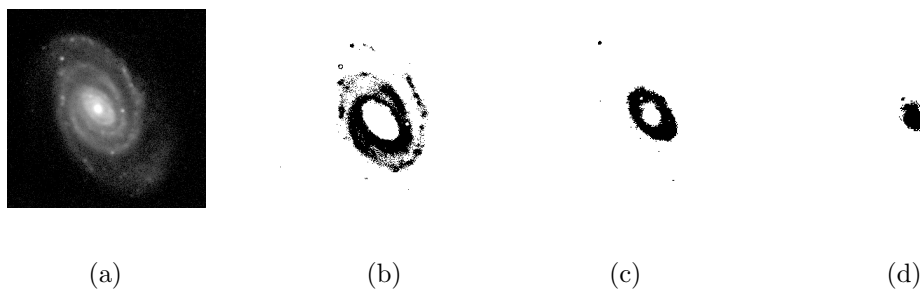|			
(a)	(b)	(c)	(d)

Figure 5.1.1: Illustration of segmentation based on different range of gray levels. Fig.(a)– Original image, Fig.(b) – Segmented from level 0 to 85, Fig.(c) – Segmented from level 85 to 170, Fig.(d) – Segmented from level 170 to 255.

Bibliography

Belongie, S., G. Mori, and J. Malik (2000). Matching with shape contexts. In *IEEE Workshop on Content-based access of Image and Video-Libraries*, pp. 20. 30

Bowman, E. T. (2001). Particle shape characterisation using fourier descriptor analysis. *Geotechnique 51*(6), 545–554. 40, 61

Chen, C.-C. (1993). Improved moment invariants for shape discrimination. *Pattern Recognition 26*(5), 683–686. 41

Chen, C. H. (2005). *Handbook Of Pattern Recognition And Computer Vision.* River Edge, NJ, USA: World Scientific Publishing Co., Inc. 39

Chuang, G. C.-H. and C. C. Kuo (1996, January). Wavelet descriptor of planar curves: theory and applications. *Trans. Img. Proc. 5*(1), 56–70. 40

Dalal, N. and B. Triggs (2005). Histograms of oriented gradients for human detection. In *Proceedings of the 2005 IEEE Computer Society Conference on Computer Vision and Pattern Recognition (CVPR'05) - Volume 1 - Volume 01*, CVPR '05, Washington, DC, USA, pp. 886–893. IEEE Computer Society. 30

Dampos, T. E. d., R. S. Feris, and R. M. C. Junior (2000). Improved face/spl times/non-face discrimination using fourier descriptors through feature selection. In *Proceedings of the 13th Brazilian Symposium on Computer Graphics and Image Processing*, SIBGRAPI '00, Washington, DC, USA, pp. 28–35. IEEE Computer Society. 35

Dang, J., Y. Wang, and S. Zhao (2006). Face recognition based on radial basis function neural networks using subtractive clustering algorithm. In *Intelligent*

Control and Automation, 2006. WCICA 2006. The Sixth World Congress on, Volume 2, pp. 10294 –10297. 29

Deniz, O., G. Bueno, J. Salido, and F. de la Torre (2011). Face recognition using histograms of oriented gradients. *Pattern Recognition Letters 32*(12), 1598–1603. 35

El-ghazal, A., O. Basir, and S. Belkasim (2009). Farthest point distance: A new shape signature for fourier descriptors. *Signal Processing: Image Communication 24*(7), 572 – 586. 27, 28, 41

El Rube, I., N. Alajlan, M. S. Kamel, M. Ahmed, and G. H. Freeman (2006). Mtar: A robust 2d shape representation. *International Journal of Image and Graphics 06*(03), 421–443. 41

Fitzgibbon, A., M. Pilu, and R. B. Fisher (1999, May). Direct least square fitting of ellipses. *IEEE Trans. Pattern Anal. Mach. Intell. 21*(5), 476–480. 62

Flusser, J. and T. Suk (1993). Pattern recognition by affine moment invariants. *Pattern Recognition 26*(1), 167–174. 63

Frei, Z., P. Guhathakurta, J. E. Gunn, and J. A. Tyson (1996). A Catalog of Digital Images of 113 Nearby Galaxies. *Astronomical Journal 111*, 174–181. 87, 95, 109

Gangopadhyay, A. (2001). An image-based system for electronic retailing. *Decision Support Systems 32*(2), 107 – 116. 34

Goderya, S. and S. Lolling (2002). Morphological classification of galaxies using computer vision and artificial neural networks: A computational scheme. *Astrophysics and Space Science 279*, 377–387. 86

Grauman, K. and T. Darrell (2005). The pyramid match kernel: Discriminative classification with sets of image features. In *Proceedings of the Tenth IEEE International Conference on Computer Vision - Volume 2*, ICCV '05, Washington, DC, USA, pp. 1458–1465. IEEE Computer Society. 33

BIBLIOGRAPHY

Guo, Q., F. Guo, and J. Shao (2010, oct.). Irregular shape symmetry analysis: Theory and application to quantitative galaxy classification. *Pattern Analysis and Machine Intelligence, IEEE Transactions on 32*(10), 1730 –1743. 86

Hu, M. K. (1962, February). Visual Pattern Recognition by Moment Invariants. *IRE Transactions on Information Theory IT-8*, 179–187. 19, 40, 41, 48, 52, 61

Huang, S.-S., H.-M. Tsai, P.-Y. Hsiao, M.-Q. Tu, and E.-L. Jian (2011). Combining histograms of oriented gradients with global feature for human detection. In K.-T. Lee, W.-H. Tsai, H.-Y. Liao, T. Chen, J.-W. Hsieh, and C.-C. Tseng (Eds.), *Advances in Multimedia Modeling*, Volume 6524 of *Lecture Notes in Computer Science*, pp. 208–218. Springer Berlin Heidelberg. 30

Jain, R. C., R. Kasturi, and B. G. Schunck (1995). *Machine vision*. McGraw-Hill. 15, 22

Jenkin, M. and L. Harris (1997). *Computational and Psychophysical Mechanisms of Visual Coding*. Cambridge University Press. 22

Jianchao, Y., Y. Kai, G. Yihong, and S. H. Thomas (2009). Linear spatial pyramid matching using sparse coding for image classification. In *Computer Vision and Pattern Recognition, 2009. CVPR 2009. IEEE Conference on*, pp. 1794–1801. 32

Kazhdan, M., P. Simari, T. Mcnutt, B. Wu, R. Jacques, M. Chuang, and R. Taylor (2009). A shape relationship descriptor for radiation therapy planning. In *Proceedings of the 12th International Conference on Medical Image Computing and Computer-Assisted Intervention: Part II*, MICCAI '09, Berlin, Heidelberg, pp. 100–108. Springer-Verlag. 34

Khotanzad, A. and Y. H. Hong (1990, May). Invariant image recognition by zernike moments. *IEEE Trans. Pattern Anal. Mach. Intell. 12*(5), 489–497. 40

Kobayashi, T., A. Hidaka, and T. Kurita (2008). Selection of histograms of oriented gradients features for pedestrian detection. In M. Ishikawa, K. Doya, H. Miyamoto, and T. Yamakawa (Eds.), *Neural Information Processing*, Volume

4985 of *Lecture Notes in Computer Science*, pp. 598–607. Springer Berlin Heidelberg. 30

Kue-Bum Lee, K.-S. H. (2012). Advanced leaf recognition based on leaf contour and centroid for plant classification. In *Information science and technology (IST), 2012 International Conference on*, pp. 133 –135. Science & Engineering Research Support soCiety. 41

Ladaga, J. and R. Bonetto (1998). Centroid, centroid from edge vectors, and shape descriptor using only boundary information. *Journal of Computer-Assisted Microscopy 10*, 1–9. 10.1023/A:1023302928848. 47, 48, 49

Lahav, O., A. Naim, L. Sodré, Jr., and M. C. Storrie-Lombardi (1996, nov). Neural computation as a tool for galaxy classification: methods and examples. *Monthly Notices of the Royal Astronomical Society 283*, 207. 86

Lambert, G. and H. Gao (1995). Line moments and invariants for real time processing of vectorized contour data. In *Proceedings of the 8th International Conference on Image Analysis and Processing*, ICIAP '95, London, UK, UK, pp. 347–352. Springer-Verlag. 25

Latecki, L. J. and R. Lakmper (1999). Convexity rule for shape decomposition based on discrete contour evolution. *Computer Vision and Image Understanding 73*, 441–454. 26

Lazebnik, S., C. Schmid, and J. Ponce (2006). Beyond bags of features: Spatial pyramid matching for recognizing natural scene categories. In *Proceedings of the 2006 IEEE Computer Society Conference on Computer Vision and Pattern Recognition - Volume 2*, CVPR '06, Washington, DC, USA, pp. 2169–2178. IEEE Computer Society. 33

Lee, D. R. and G. T. Sallee (1970). A method of measuring shape. *Geographical Review 60*(4), 555–563. 24

Lee, S. H., S. Sharma, L. Sang, J.-I. Park, and Y. G. Park (2011). An intelligent video security system using object tracking and shape recognition. In *Proceedings*

of the 13th international conference on Advanced concepts for intelligent vision systems, ACIVS'11, Berlin, Heidelberg, pp. 471–482. Springer-Verlag. 34

Lekshmi, S., K. Revathy, and S. R. P. Nayar (2003). Galaxy classification using fractal signature. *Astronomy & Astrophysics 405*, 1163–1167. 75, 82, 86, 100, 101, 102, 109, 111

Li, H., Z. Guo, S. Ma, and N. Luo (2011, nov.). A new touchless palmprint location method based on contour centroid. In *Hand-Based Biometrics (ICHB), 2011 International Conference on*, pp. 1 –5. 41

Ling, H. and D. W. Jacobs (2007). Shape classification using the inner-distance. *IEEE Transactions on Pattern Analysis and Machine Intelligence 29*, 286–299. 34

Mattias, P. H., J. Mark, B. Manav, N. M. Tahreema, G. Fergus, B. J. Michael, and A. S. Julia (2011). Non-local shape descriptor: A new similarity metric for deformable multi-modal registration. In *MICCAI (2)*, pp. 541–548. 34

Mhnen, P. and T. Frantti (2000). Fuzzy classifier for star-galaxy separation. *The Astrophysical Journal 541*(1), 261. 86

Mokhtarian, F. and M. Bober (2003). *Curvature Scale Space Representation: Theory, Applications, and MPEG-7 Standardization*. Norwell, MA, USA: Kluwer Academic Publishers. 26

Mokhtarian, F. and A. K. Mackworth (1992, August). A theory of multiscale, curvature-based shape representation for planar curves. *IEEE Trans. Pattern Anal. Mach. Intell. 14*(8), 789–805. 40

Newell, A. J. and L. D. Griffin (2011). Multiscale histogram of oriented gradient descriptors for robust character recognition. *0*, 1085–1089. 30

Odewahn, S., E. Stockwell, R. Pennington, R. Humphreys, and W. Zumach (1992). Automated star/galaxy discrimination with neural networks. *Astronomical Journal 103*(1), 318–331. 86

Otsu, N. (1979). A Threshold Selection Method from Gray-level Histograms. *IEEE Transactions on Systems, Man and Cybernetics 9*(1), 62–66. 82, 83, 98, 110

Padraig Corcoran, P. M. and A. Winstanley (2011). A convexity measure for open and closed contours. In *Proceedings of the British Machine Vision Conference*, pp. 81.1–81.11. BMVA Press. http://dx.doi.org/10.5244/C.25.81. 26

Pao, H., D. Geiger, and N. Rubin (1999). Measuring convexity for figure/ground separation. In *Proceedings of the International Conference on Computer Vision-Volume 2 - Volume 2*, ICCV '99, Washington, DC, USA, pp. 948–. IEEE Computer Society. 26

Peura, M. and J. Iivarinen (1997). Efficiency of simple shape descriptors. In C. Arcelli, L. P. Cordella, and G. S. di Baja (Eds.), *Advances in Visual Form Analysis*, Singapore, pp. 443–451. World Scientific. 62

Proffitt, D. (1982). The measurement of circularity and ellipticity on a digital grid. *Pattern Recognition 15*(5), 383 – 387. 62

Rahtu, E., M. Salo, and J. Heikkila (2006, September). A new convexity measure based on a probabilistic interpretation of images. *IEEE Trans. Pattern Anal. Mach. Intell. 28*(9), 1501–1512. 26

Rosin, P. L. (1999). Measuring rectangularity. *Machine Vision and Applications 11*, 191–196. 10.1007/s001380050101. 24

Rosin, P. L. (2000). Shape partitioning by convexity. *IEEE Transactions on Systems, Man, and Cybernetics. Part A: Systems and Humans 30*, 202–210. 26

Rosin, P. L. (2003a). Measuring shape: ellipticity, rectangularity, and triangularity. *Machine Vision and Applications 14*, 172–184. 34, 62

Rosin, P. L. (2003b). Measuring sigmoidality. In N. Petkov and M. A. Westenberg (Eds.), *Computer Analysis of Images and Patterns, 10th International Conference, CAIP 2003, Groningen, The Netherlands, August 25-27, 2003, Proceedings,*

Volume 2756 of *Lecture Notes in Computer Science*, pp. 410–417. Springer. 29, 61

Rosin, P. L. and J. Žunić (2011, January). Measuring squareness and orientation of shapes. *J. Math. Imaging Vis. 39*(1), 13–27. 86

Schleicher, D. and B. Zagar (2008, oct.). Image processing to estimate the ellipticity of steel coils using a concentric ellipse fitting algorithm. In *Signal Processing, 2008. ICSP 2008. 9th International Conference on*, pp. 884 –890. 62

Sezgin, M. and B. Sankur (2004, January). Survey over image thresholding techniques and quantitative performance evaluation. *Journal of Electronic Imaging 13*(1), 146–168. 98, 110

Sobel, I. E. (1970). *Camera models and machine perception*. Ph. D. thesis, Stanford, CA, USA. AAI7102831. 31

Sonka, M., V. Hlavac, and R. Boyle (2007). *Image Processing, Analysis, and Machine Vision*. Thomson-Engineering. 23, 26, 40, 48, 62, 64

Stojmenovic, M. and A. Nayak (2007). Direct ellipse fitting and measuring based on shape boundaries. In *PSIVT*, pp. 221–235. 62

Stojmenović, M., A. Nayak, and J. Zunic (2008, August). Measuring linearity of planar point sets. *Pattern Recogn. 41*(8), 2503–2511. 61

Stojmenović, M. and J. Žunić (2008, January). Measuring elongation from shape boundary. *J. Math. Imaging Vis. 30*(1), 73–85. 29

Sun, Q., C. Lam, and J. Wu (1998). A practical automatic face recognition system. In H. Wechsler, P. Phillips, V. Bruce, F. Souli, and T. Huang (Eds.), *Face Recognition*, Volume 163 of *NATO ASI Series*, pp. 537–546. Springer Berlin Heidelberg. 35

Swain, M. J. and D. H. Ballard (1991, November). Color indexing. *Int. J. Comput. Vision 7*(1), 11–32. 33

Tang, Y. (2000). *Wavelet Theory and Its Application to Pattern Recognition*. Series in Machine Perception and Artificial Intelligence. World Scientific. 29

Voss, K., H. Suesse, and R. Neubauer (1995). Moment-based invariant fiting of elliptical segments. In *Proceedings of the 6th International Conference on Computer Analysis of Images and Patterns*, CAIP '95, London, UK, UK, pp. 562–567. Springer-Verlag. 40

Žunić, J., K. Hirota, and P. L. Rosin (2010, January). A hu moment invariant as a shape circularity measure. *Pattern Recognition 43*(1), 47–57. 23, 35, 48

Žunić, J., L. Kopanja, and J. E. Fieldsend (2006, May). Notes on shape orientation where the standard method does not work. *Pattern Recogn. 39*(5), 856–865. 64, 72, 79

Žunić, J. and P. L. Rosin (2003, September). Rectilinearity measurements for polygons. *IEEE Trans. Pattern Anal. Mach. Intell. 25*(9), 1193–1200. 61

Watanabe, T., S. Ito, and K. Yokoi (2009). Co-occurrence histograms of oriented gradients for pedestrian detection. In T. Wada, F. Huang, and S. Lin (Eds.), *Advances in Image and Video Technology*, Volume 5414 of *Lecture Notes in Computer Science*, pp. 37–47. Springer Berlin Heidelberg. 30

Whitney, A. W. (1971, September). A direct method of nonparametric measurement selection. *IEEE Trans. Comput. 20*(9), 1100–1103. 82, 99

Xu, D. and H. Li (2008, January). Geometric moment invariants. *Pattern Recogn. 41*(1), 240–249. 48

Zabrodsky, H., S. Peleg, and D. Avnir (1995, December). Symmetry as a continuous feature. *IEEE Trans. Pattern Anal. Mach. Intell. 17*(12), 1154–1166. 61

Zahn, C. T. and R. Z. Roskies (1972, March). Fourier descriptors for plane closed curves. *Transactions on Computers, IEEE c-21*(3), 269–281. 40

Zaker, N., M. H. Mahoor, W. I. Mattson, D. S. Messinger, and J. F. Cohn (2012). Intensity measurement of spontaneous facial actions: Evaluation of different image representations. In *ICDL-EPIROB*, pp. 1–2. IEEE. 35

Zeng, W., R. Shi, Y. Wang, S.-T. Yau, and X. Gu (2012). Teichmller shape descriptor and its application to alzheimers disease study. *International Journal of Computer Vision*, 1–16. 34

Zhang, D. and G. Lu (2002). A comparative study of fourier descriptors for shape representation and retrieval. In *Proc. of 5th Asian Conference on Computer Vision (ACCV*, pp. 646–651. Springer. 27

Zhang, D. and G. Lu (2005). Study and evaluation of different Fourier methods for image retrieval. *Image and Vision Computing 23*, 33–49. 27